Seasonal pumped thermal energy storage with 89% round-trip efficiency.

Summary

Storing energy produced by wind and solar energy is one of the biggest challenges of the green transition. Here we present a solution to that problem. Electricity is stored as heat in a truncated cone-shaped open pit filled with crushed stone. The storage consists of two gas-tight halves that are insulated from each other. The mass of the upper low-pressure storage pressurizes the lower high-pressure storage, where the heat is stored. Between these chambers, a two-way closed Brayton cycle is implemented using optimized axial turbines and compressors[1]. The concept is in the scientific literature under various names, such as *Pumped Thermal Energy Storage* (PTES), *Pumped Heat Electricity Storage* (PHES) or Carnot Battery.

The energy is loaded into the storage with the reverse Brayton cycle, which works on the same principle as the heat pump. The main compressor heats the hot gas from the upper part of the low-pressure storage by pressurizing it to red-hot upper part of the high-pressure storage. At the same time, the opposite cryogenic turbine keeps the storage pressures constant by cooling the cold gas from the bottom of the high-pressure storage to the saturation point and saving the cryogenic cold to the lower part of the low-pressure storage.

The discharge of electricity takes place with the usual Brayton cycle, where the red-hot gas from the high-pressure storage is discharged through the main turbine to the upper part of the low-pressure storage. The pressure difference between the storages is again kept constant by compressing the cryogenic gas from the bottom of the low-pressure storage to the cold bottom of the high-pressure storage. The work done by the compressor is directly proportional to the absolute temperature of the compressed gas, so the efficiency of the discharge cycle is maximized by keeping the gas temperature as close to the saturation point as possible.

The gas discharged from the turbine and compressor flows through the crushed stone of the storages while either heating up or cooling down to the temperature of the opposite side. Thus, in this solution, the crushed stone functions as both a heat storage and a heat exchanger at the same time. Since the efficiency of the system cannot be 100%, excess heat is accumulated during charge and discharge, which can be partially recycled back into the process by using higher pressure difference during the discharge or utilized as district heating.

The excess heat accumulated on the cold side is removed by a separate high-efficiency heat pump during the charging. It cools the cold gas coming from the high-pressure storage so that the gas coming out of the cryogenic axial turbine is at the saturation point and at the same time slightly wet so that the pressure and total mass of the gas can be kept constant. The liquefied part of the gas is separated into a separate storage. The heat produced by the heat pump axial compressor is cooled as waste heat, fed directly into the district heating network or stored in some other way.

The excess heat accumulated on the hot side can be converted into electricity when the pressure of the low-pressure storage is reduced in the discharge mode so that the exit temperature of the gas from the main

---

[1]https://en.wikipedia.org/wiki/Brayton_cycle

turbine is the same as the inlet temperature of the main compressor. This solution simplifies the structure of the low-pressure storage, because the excess heat does not need to be cooled. In addition, the hot compressor and turbine can share the same low-pressure pipes and gas distribution channels. However, at the same time, the cooling of the cold side must be slightly increased, because in addition to the main turbine, the pressure ratio of its counterpart, the cryogenic compressor, and the waste heat it produces also increase.

The capacity of the storage is limited by the fact that the specific heat capacity of the working fluid is almost constant at different temperatures, while the specific heat capacity of solids decreases to zero as absolute zero is approached. Thus, the cold storage of a gas at the saturation point requires about 2.5 times more crushed stone than the high-pressure hot storage. The dependence of the specific heat capacities of solids on temperature is best described by the Debye model[2]. In the model, the specific heat capacity of a solid depends on the ratio of the measurement temperature and its Debye temperature. The lower is solid's Debye temperature, the better it stores cryogenic cold. The Debye temperatures of rock minerals are between 500–1200 K, so they store cryogenic cold quite poorly compared to, for example, water ice, which has a Debye temperature of 300 K, when the measurement temperature is 100 K. In this study we will use the charge-discharge simulation to show that, despite the limitations imposed by the Debye model, almost 60% of the theoretical maximum heat capacity of a high-pressure storage can be utilized when the cryogenic cold is stored mainly to crushed ice.

In this study the operating principle of the solution will be described in detail, the dimensioning of the energy storage will be cost optimized, problems related to its technical implementation will be analyzed and solutions proposed, the operation of the storage will be simulated programmatically, optimized designs of plant's axial turbomachines and heat exchangers are presented, their efficiencies of the designs are predicted by the best mean line loss models for axial compressors and turbines. The resulted on-design round-trip efficiency of the storage is 89%, which is better than in any pumped hydro storage and in the range of large lithium-ion batteries (85% - 95%).

The default energy storage design has a very wide charge/discharge power range. The round-trip efficiency decreases only 0.9% if the default 1009 power is quadrupled to 4036 MW. However, if the energy storage size is less than ten million tons crushed stone, various size-related problems and equipment costs increase rapidly. The technical upper limit for the charge and discharge power is set by the increasing flow resistance of the crushed stone and its heat exchange capability, which are opposite properties. The power of heat exchange is directly proportional to the surface area of the crushed stone, but on the other hand, the small average grain size and low porosity of the crushed stone increase the gas flow resistance.

Nitrogen has been found to be the best working fluid because it is inexpensive to produce on site, and its low vaporization temperature allows for a larger temperature difference between the cryogenic and hot cycles of the storage. In addition, nitrogen is an inert gas, meaning it reacts very weakly with other elements. This makes it a very problem-free working fluid compared to hydrogen, oxygen, methane or carbon dioxide. Finally, the unit costs of the stored energy and the charging and discharging power and the return on investment are evaluated. Argon is the secondary choice.

The search words "energy store Brayton cycle" return many new scientific articles about the thermal storage of electricity based on the Brayton cycle. A recently published study *Derived energy storage systems from Brayton*

---

[2]https://en.wikipedia.org/wiki/Debye_model

cycle[3] is an overview of the current state of research in the field. In it, researchers compare Brayton cycle-based CAES (compressed air energy system) and PTES (pumped thermal energy store) solutions at a theoretical level. For example, under the leadership of Josh McTigue, the feasibility of PTES projects has been mapped[4] [5]. The researchers considered that a 75% round-trip efficiency could be achieved with supercritical carbon dioxide when the heat is stored in table salt [6]. The techno-economic comparison of PTES solutions has also been studied in another study, which also ended up proposing different pressure ratios for charging and discharging. Concrete solutions to the further development needs [7]of PTES and techno-economic challenges mentioned in those studies will be presented in this article. In this solution, the crushed stone acts as a massive heat storage and heat exchanger at the same time. The inexpensive open-pit rock mining technology enables storage costs/kWh that are two orders of magnitude lower than in any battery storage. The default parameters of the energy storage design program produce an energy storage with a storage capacity of 1100 GWh and a discharge capacity of 1211 MW. The unit cost of the built storage capacity is 28 cents/kWh using the given unit costs when the cost of charge/discharge power is excluded. It is currently about 1/400 of the cost of a lithium-ion battery. When the efficiency of the plant's turbines and compressors is optimized to the upper limit set by current material technology in the manner presented above, then, based on the compressor loss model, at best 92% of the electricity charged from the grid would be recovered as electricity, when the upper temperature of the high-pressure storage is 900 °C, and the losses of the motor-generators and cooling heat pumps are also taken into account.

General operating principle and energy storage layout

The next figure shows a cross-section of the energy storage generated by the default parameters of the design and simulation program. Its size, approximately 28 million tons, corresponds to the annual mining volume of medium size open pit, such as Yara's Siilijärvi phosphate mine in Finland (mining approximately 20–30 million tons per year) [8]. There, the mining contractor's 200 employees are responsible for all mining, crushing, transporting the crushed rock to the processing and finally dumping the waste rock. Thus, the mining of the energy storage, crushing the crushed stone, screening and spreading it back could be a task of approximately 200 person-years, and its cost is estimated here at 12 euros/m3, which corresponds to the average mining cost for open pit mines of this size. The crushed ice storage, the liquid nitrogen storage and the motor generator are duplicated on both sides of the figure for clarity.

---

[3]https://www.sciencedirect.com/science/article/pii/S2589004224006813#:~:text=energy%20for%20storage.-,In%20discharge%20process%2C%20a%20Brayton%20cycle%20is%20formed%20by%20the,is%20converted%20back%20to%20electricity.

[4] https://core.ac.uk/download/pdf/42338379.pdf

[5]https://www.researchgate.net/publication/356766772_Techno-economic_analysis_of_recuperated_Joule-Brayton_pumped_thermal_energy_storage

[6] https://www.energy.gov/sites/default/files/2020/12/f81/SETO%20PTES%20Workshop%20McTigue_NREL.pdf

[7]https://www.mdpi.com/1996-1073/15/24/9595

[8]https://www.yara.fi/tietoa-yarasta/yara-suomi/toimipaikat/siilinjarvi/tuotantolaitos/
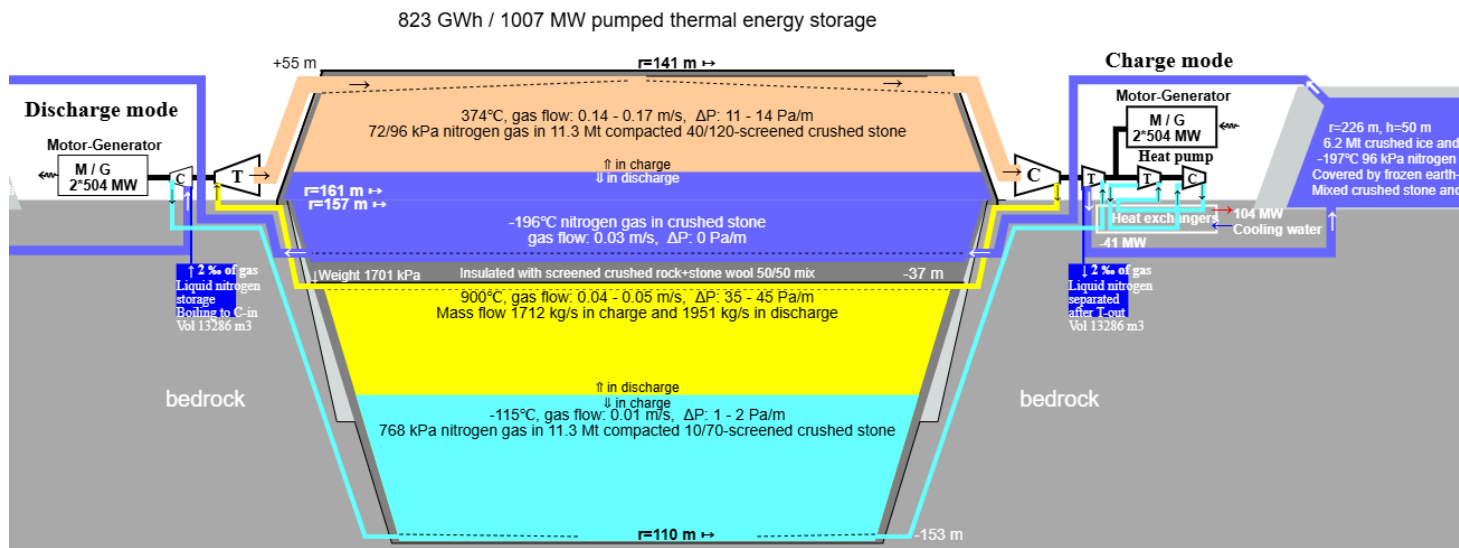
Figure 1. Cross -section and operating principle of the energy storage system where all quarried rock has been used for storage

In the figure, the slope of the fully reinforced wall of the open pit (including the gray filled double ramps) is 73 degrees, the high temperature is 900 °C. The high pressure of the storage is 768 kPa, the low pressure in the charging is 96 kPa, and in the discharging is 72 kPa. When using the efficiencies calculated with the compressor and turbine loss models, the electricity round-trip efficiency is 88.7%, when 10.1% cooling work of the heat pumps and 1.7% losses of the motor-generator are included. The high-pressure compressor and turbine blades do not need any cooling at that temperature, and the crushed mafic and ultramafic rocks still have good long-term durability. If the high-pressure storage were made of granite or gneiss, and its temperature should not exceed 573 °C, because the quartz crystal changes weather the granite at that temperature.

For clarity, the charging and discharging and the separate ice storage are placed on different sides in the figure, even though they share the same motor-generator. In the figure, the plant would consist of two identical units, so that they could be run flexibly according to the demand and supply of electricity, and so that they could be maintained one at a time. In addition, the discharging and charging power can be adjusted by changing the pressure ratio of the storages.

The design and analysis program can design the storage with different pressure ratios, but the turbomachines must be re-optimized for new pressure ratio and mass flow. The program increases the amount of excavation, so that with the given parameters, the gravitation of the crushed rock above is at least the same as the high pressure of the lower storage. An error tolerance of 100 kPa (i.e. about one atmosphere) is added by default. The pressure ratio 1:8 has the best round-trip efficiency, but its capacity unit cost estimation is 20% above the unit cost of pressure ratio 1:20.

The black lines in the figure are gas-tight boundaries, which can be welded steel or aluminum plates, injected rock, or even rock frozen by geothermal piping. Pumping caused by thermal expansion and contraction of the rock may gradually spread the upper part of the ground surface by several meters, so the steel plate must have vertical flexible folds. The steel plate above the high-pressure storage becomes a soft surface that stretches and shrinks with the surrounding crushed stone. The gas-tightness of the pressure storage can be ensured by a mixture of fine crushed stone above the steel plate surface and crushed stone that partially melts at the temperature of the high-pressure storage, which compresses into a solid elastic gas-impermeable layer under

heat and pressure. Even elastic ice and crushed stone mix could be used as a gas-tight layer between the storages when the pressure ratio is 1:12 or less.

The dark grey areas inside the black lines are thermal insulation layers, which contain equal volumes of stone wool or high-quality biochar and uniformly graded crushed stone having the compacted porosity above 0.40[9]. Heat conduction by convection can be minimized by adding thin horizontal layers of compacted clay to the vertical insulation layers. The u-value of this insulation has been estimated 0.1 W/m/K in this study. Biochar is excellent for high-temperature insulation in anoxic conditions. The melting point of biochar is 3000 Kelvin, the u-value is 0.03 W/m/K, its pore density is very high, and its size is small, at best only a few micrometers[10] [11], so it insulates thermal radiation at least one order of magnitude better than the commercial insulations, with cell sizes of 100–200 micrometers at best. The pyrolysis temperature should match with the temperature range of the insulation. At 900 °C biochar has transformed to a very small graphite sheets and its carbon content is over 90%.

In the figure, the thickness of the insulation layers has been calculated so that the heat leakage is approximately the same everywhere, 20 W/m^2, which means that the heat leakage of the high-pressure storage in the figure would be less than 4 MW when fully charged. The sloping walls of the upper part of the above-ground section have also been insulated from the inside with the insulation mix. Instead, the roof can be constructed using standard storage hall construction technology, and insulated from above with non-combustible stone wool, if this proves to be a more economical structure.

Instead of biochar, unbound blown stone wool could be used. Stone wool does not reduce iron oxide in the crushed stone and oxygen does not anneal it. The binders of ordinary stone wool insulation begin to evaporate at 250 °C, but the temperature range of the ordinary pure stone wool is 700–850 °C and ceramic fiber wools can withstand temperatures up to 1200 °C[12]. The use and application of blown stone wool may be technically simpler than biochar, and its price per unit volume may be cheaper than biochar, since its density is only 36 kg/m^3. The tax-free hardware store price of blown stone wool sold in plastic bags is about 1.6 euros/kg, but the factory price for thousands of tons of loose stone wool may be less than 500 euros/ton, which would make the cubic price of 50/50 loose stone wool insulation about 18 euros/m^3 or 36 euros/m^3 if the density of the stone wool is doubled to prevent convection. At that density, stone wool has a U-value of 0.033 W/mK, but it may not perform as well as a high-temperature insulator due to its larger pore size.

The gas coming from and to the pipes is distributed evenly along the branching channels running in the crushed stone so that its flow rate slows down enough so that stone dust is not carried into the equipment with the incoming gas. The gas duct in the hot upper part of the high-pressure storage are vaulted structures made of masonry or cast firebricks. The vault structures of the other three gas distribution ducts can be cast from reinforced concrete, where the steel mainly acts as concrete shrinkage reinforcement. The compressive strength of concrete increases as the temperature decreases, so it is therefore perfectly suited for vault structures in very cold lower parts having the highest compression. The branching distribution ducts are vaults

---

[9] https://wiki.sustainabletechnologies.ca/wiki/Aggregates
[10] https://link.springer.com/article/10.1007/s11157-020-09523-3#Tab2
[11]
https://pubmed.ncbi.nlm.nih.gov/30159845/#:~:text=The%20pore%20size%20distribution%20of,1.5%2D3%20%CE%BCm%2C%20respectively
[12] https://en.wikipedia.org/wiki/Mineral_wool#Use

open from the bottom, below which there is a gas distribution layer about 1–2 meters thick made of washed, sorted, coarser crushed stone, where the gas spreads and slows down to the very slow speed less than 0.2 m/s.

Between the hot and cold crushed stone layers is a heat exchange area. The convection slowly expands the area when the storage is used as will be shown later in the storage simulation.
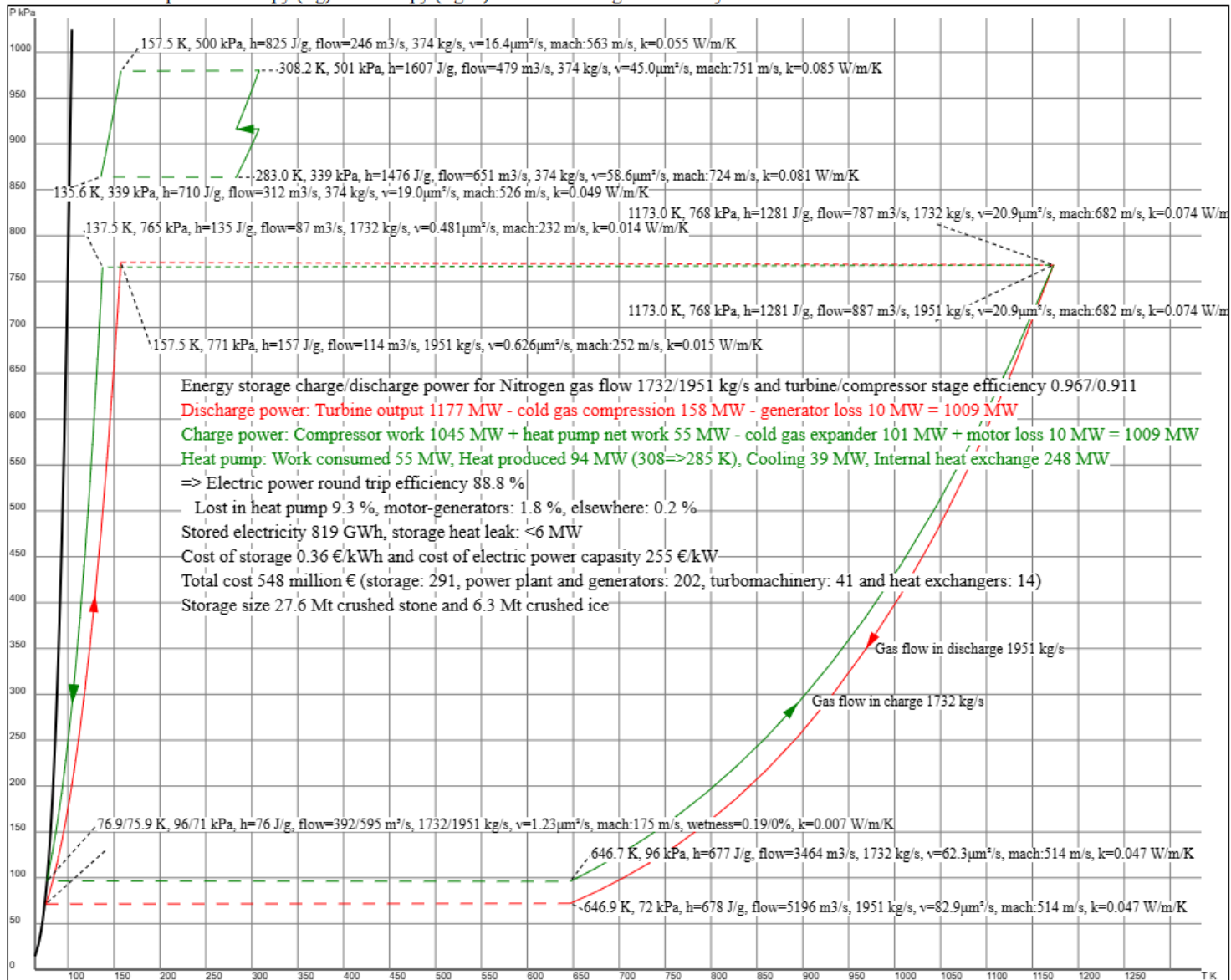

Figure 2. Energy storage operation as a TP diagram, with the horizontal axis showing temperature in kelvins and the vertical axis showing pressure in kilo Pascals.

Figure 2 shows a temperature/pressure diagram of the plant operation drawn by the design program. The storage charge cycle is drawn in green and the discharge cycle in red. The arrows indicating the gas flow direction are upwards for compressors and downwards for turbines. The dashed lines depict the gas flow through the crushed stone. They are slightly inclined to the gas flow direction due to the pressure drop caused by the crushed stone. The TP curves for turbines and compressors are curved because the pressure change has been calculated in very small parts according to the average stage efficiency calculated by the loss model.

Charge and discharge cycles share the same motor-generator, so their mass flows and equipment powers have been adjusted accordingly. In the middle of the figure are the powers and losses of the main components, the electricity round-trip efficiency and the price estimate calculated according to the unit prices given to the program. The default unit price values are based on published price estimates for the corresponding work stages and equipment.

Structural engineering of the energy storage

The design and structural engineering of the energy storage must address at least the following issues: thermal expansion and contraction of the crushed stone must not rupture the pressure insulation or the pipe connections coming from the rock wall. In addition, the repeated heating and cooling cycles must not fragmentate and compact too much the rock particles during the planned service life. The implementation of storage walls and the management of thermal expansion are considerably simplified if the storage can be built in a closed open pit, quarry or similar depression in such a way that all crushed stone of the storage is surrounded by rock walls. The next figure shows a 41 Mt 818 GWh storage without external ice storage. The portion of the low-pressure storage has been increased because the cryogenic rock has lowered specific heat capacity.
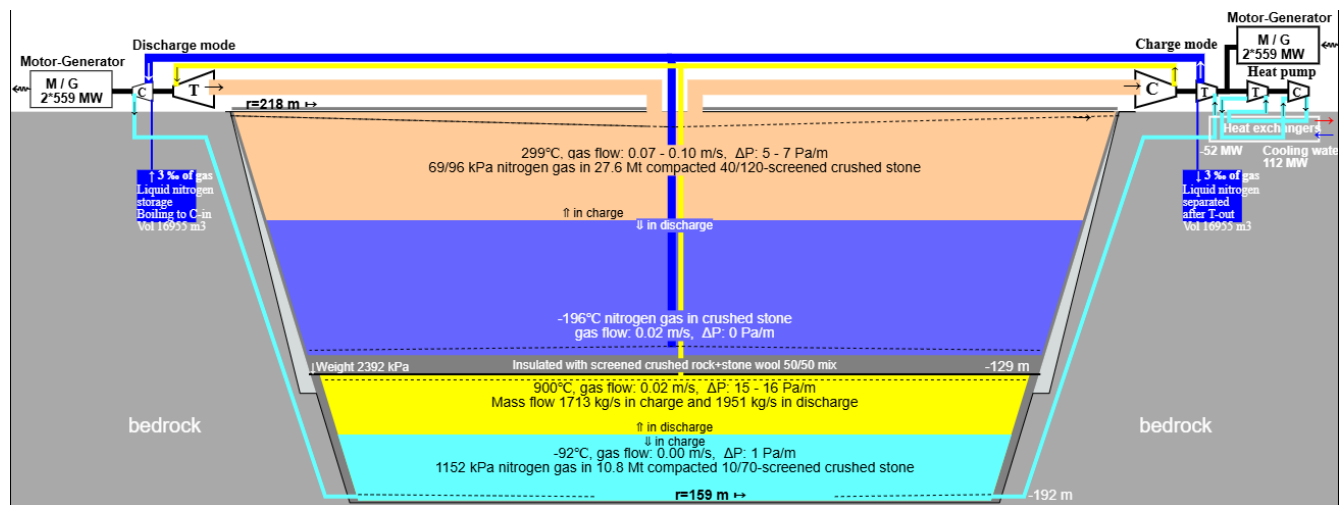

Figure 3. 41 Mt, 1118 MW and 863 GWh storage with 1:12 pressure ratio.

The durability of the crushed stone in high-pressure storage

The crushed stone of the high-pressure storage should withstand at least several dozen very slow heating and cooling cycles between the upper and lower temperatures of the high-pressure storage. It must maintain sufficient compressive strength so that the crushed stone does not start to compress into a pile. In addition, the crushed stone should not evaporate a harmful amount of gas, such as sulfur, which, by liquefying and crystallizing, would impair the operation of the main turbine. It should also have a high volumetric heat capacity. The most common mixed igneous rock types found on the surface of the earth, such as granite or gneiss, do not meet these requirements. For example, granite gradually begins to thermally crack after exceeding a temperature of 572 °C, because at this point the dominant α-crystal structure of quartz starts to

change to a β-crystal structure that has approximately 4% larger volume. This causes microcracks in the rock, [13]even if the rock is heated and cooled very slowly. This is probably because the other main mineral in granite, potassium feldspar, does not undergo a similar change in crystal structure, so internal stresses are created in the rock. In other words, rocks in which the proportion of quartz crystals is either sufficiently small or very large can better withstand high temperatures.

Study *High Temperature Versus Geomechanical Parameters of Selected Rocks— The Current State of Research*[14] It was found that the compressive strength of the tested sandstones and claystones initially increased significantly up to 400 °C and then began to slowly decrease. The initial compressive strength of 150 MPa was exceeded for a fine-grained and dense sandstone until 1000 °C, but for coarse-grained sandstone it was lost before 800 °C. For the other tested rock types (granite, marble and limestone), the compressive strength decreased continuously with increasing temperature, and at high temperatures it was significantly worse than the compressive strength of sandstones. This study also found a collapse in the compressive strength of granite before 600 °C. The researchers concluded that the temperature behavior of the rock's strength depends on its mineral composition, crystal size and porosity.

In the study *Effect of heat on the mechanical properties of selected rock types in a laboratory study* [15]compared the strength properties of diabase, granite and two quartzite schists after heating and cooling. The granite lost almost completely its compressive strength at temperature of 1100 °C. The reason is probably the melting of potassium feldspar, the other main mineral in granite. In that study, ultramafic diabase retained best its original compressive strength.

The same conclusion has also been reached in Finnish sauna stove stone tests [16]. Currently, the stove stones sold in Finland are mostly olivine gabbro. Olivine gabbro and other stove stones can withstand temperatures of at least 1100 °C without melting. Stove stones are mafic or ultramafic rocks, meaning they have solidified at the bottom of ancient volcanic vents and magma chambers. The sequence of the crystallization of common silicate minerals is described by **Bowen's reaction series**[17] in the next figure with the classification of igneous rock types[18].

---

[13] [Frontiers | Fractal Characteristics and Energy Dissipation of Granite After High-Temperature Treatment Based on SHPB Experiment (frontiersin.org)](#)
[14][https://www.sciencedirect.com/science/article/pii/S2300396015300689#:~:text=At%20temperatures%20from%20100%20to,less%20at%20the%20same%20level](https://www.sciencedirect.com/science/article/pii/S2300396015300689).
[15]
https://www.academia.edu/93970453/Effect_of_heat_on_the_mechanical_properties_of_selected_rock_types_a_laboratory_study
[16] https://saunologia.fi/kiuaskivet/

[17] https://en.wikipedia.org/wiki/Bowen%27s_reaction_series
[18]https://en.wikipedia.org/wiki/Igneous_rock
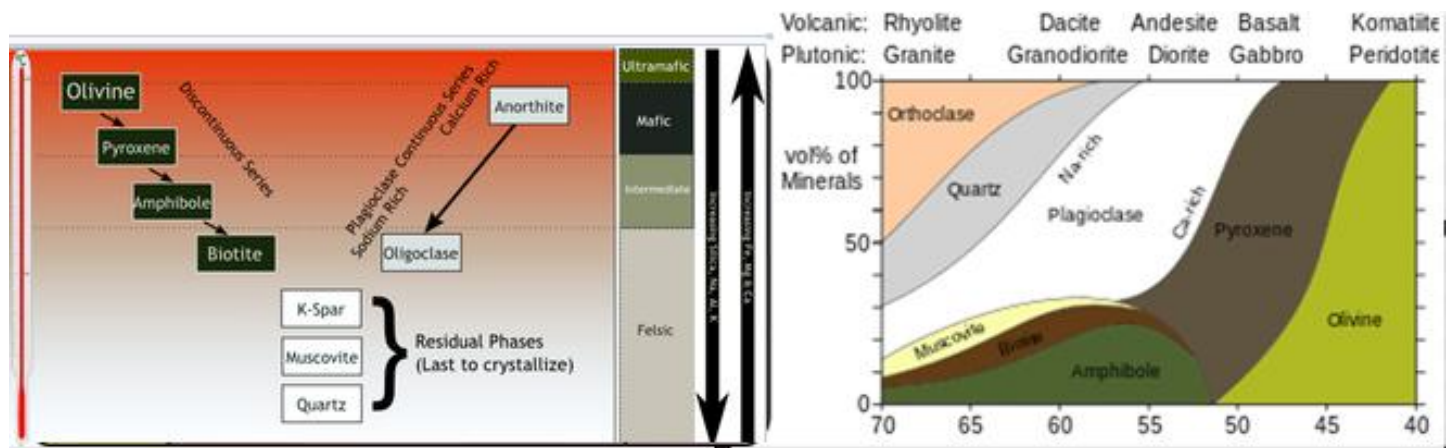
Figure 4. On the left, the Bowen's reaction series, on the right, the classification of rock types according to the content of silica and minerals

The properties of mafic and ultramafic rocks also vary. On the left, the Bowen's reaction series divides igneous rock types into main classes according to the crystallization temperature of magma eruptions. On the right, they are classified according to their silica content. The upper limit for the silica (SiO_2) content of mafic rocks is about 52% and that of ultramafic rocks 45%. In the figure, the proportions of the main minerals in each rock type are shown on the vertical line. The heat resistance of rocks generally increases as the proportion of silica decreases. In mafic rocks, it is about 1100 °C at 52%. The melting temperature of pure magnesian olivine or chromite used as foundry sand is about 1800 °C [19]. Mafic rock types are characterized by dark color, alkalinity, higher density than surface rock types, and thus also a higher specific heat capacity per volume.

In the more precise QFPA classification, [20]rock types are classified based on the sliding percentages of the four main minerals, and ultramafic rocks are classified separately [21]based on the three main minerals. Thus, the properties and melting points of so-called pure rock types also depend on the content of their main minerals and other impurities. The minerals of the rocks first soften and finally melt, each in its own temperature range. When the melting starts, the compressive strength of the rock decreases rapidly, even if it is externally intact.

Minerals: chromite and olivine, as well as mafic Plagioclase and pyroxene have high melting points. Plagioclase [22]consists of two and pyroxene [23]consists of five minerals, with mafic minerals with higher melting points at one end and felsic minerals with lower melting points at the other end. In summary, especially basic magnesium- and calcium-rich mineral subtypes have higher melting points, and correspondingly rocks containing potassium or sodium melt at lower temperatures. Replacing the magnesium portion with iron also lowers the melting temperature of the mineral.

[19] https://tupa.gtk.fi/raportti/arkisto/m19_3132_81_80.pdf
[20] https://en.wikipedia.org/wiki/QAPF_diagram
[21] https://en.wikipedia.org/wiki/Ultramafic_rock
[22]https://en.wikipedia.org/wiki/Plagioclase
[23]https://en.wikipedia.org/wiki/Pyroxene

The mafic rocks don't always be able to withstand high temperatures. The article *Damage and Changes in Mechanical Properties of a Gabbro Thermally Loaded up to 1,000°C*[24]. The summary states that the first microcracks caused by different thermal expansion coefficients of its mineral crystals appeared in the gabbro sample below 600 °C, and above that, compressive strength of the gabbro decreased dramatically mainly because of oxidation of free iron and magnesium. However, the oxidation is not possible in the nitrogen or argon gas of the storage.

The largest stove stone quarry in Finland is in Luvia [25], which belongs to the diabase vein area of southern Satakunta. Stove stones such as olivine diabase and peridotite serpentine have also been quarried from the Kemi intrusion in Keminmaa. Very dark diabase and gabbro, sold under the trade name black granite, are quarried at several natural stone quarries in Central and Eastern Finland. Mäntyharju is the only known deposit of pure [26]olivine in Finland, from which stove stone is also quarried. The melting temperature of the olivine quarried there has been measured at the Technical University of Helsinki to be 1350 °C[27]. The mafic calcium-containing subtype of hornblende (Amphibolite[28]) can also withstand high temperatures and is considered a good stove stone. Mafic hornblende has previously been quarried in Hyvinkää as stove stone.

The high proportion of waste rock is considered a challenge in the commercial exploitation of mafic rock deposits. For example, in Luvia, only about 25% of the rock extracted can be sold as stove stones. In the stone quarries, blocks of several cubic meters are cut from the rock, so the waste percentage of mafic rocks is even higher [29]. The waste rock content is high, because mafic deposits are layered and/or veined, partially or completely metamorphosed, and may be mixed with other mafic or intermediate layers such as diorite. A typical mafic so-called waste rock is peridotite, which, however, may have even better properties than pure diabase or gabbro. Thus, mixed mafic aggregates may be as usable as pure aggregates of a single rock type. Based on the storage simulation, only about 24% of the extracted crushed stone heats up to the maximum temperature of the high-pressure storage, so the above-mentioned typical concentrations of rock quarries are probably sufficient.

The mafic rock deposits are quite well studied and drilled, so based on the existing research data, it is possible to focus further research on the most promising areas. For example, the description of the Finland's bedrock[30] shows the largest mafic rock areas, but in the more detailed high-resolution description of the bedrock[31] you can see, that smaller mafic rock areas and lines with a diameter or length of a few kilometers can be found practically everywhere at least in Finland. The situation must be the same wherever there are old volcanoes. In

---

24

https://www.researchgate.net/publication/225969655_Damage_and_Changes_in_Mechanical_Properties_of_a_Gabbro_Thermally_Loaded_up_to_1000C

25 https://saunologia.fi/saunagranit-luvian-kiuaskivitehatalla/

26 https://tupa.gtk.fi/raportti/arkisto/m19_3132_81_80.pdf
27 https://suomenkiuaskivi.fi/oliviini-kiuaskivet/
28 https://en.wikipedia.org/wiki/Amphibolite
29 https://www.suomalainenkivi.fi/vanha/wp-content/uploads/2016/03/luonnonkiviväkteiden_suunnentilohje_osa2.pdf

30 https://tupa.gtk.fi/raportti/arkisto/50_2017.pdf
31 https://tupa.gtk.fi/kartta/erikoiskartta/ek_098_300dpi.pdf

Europe, they can also be found outside the actual active volcanic zones, for example in England, Central Germany, and Central France.
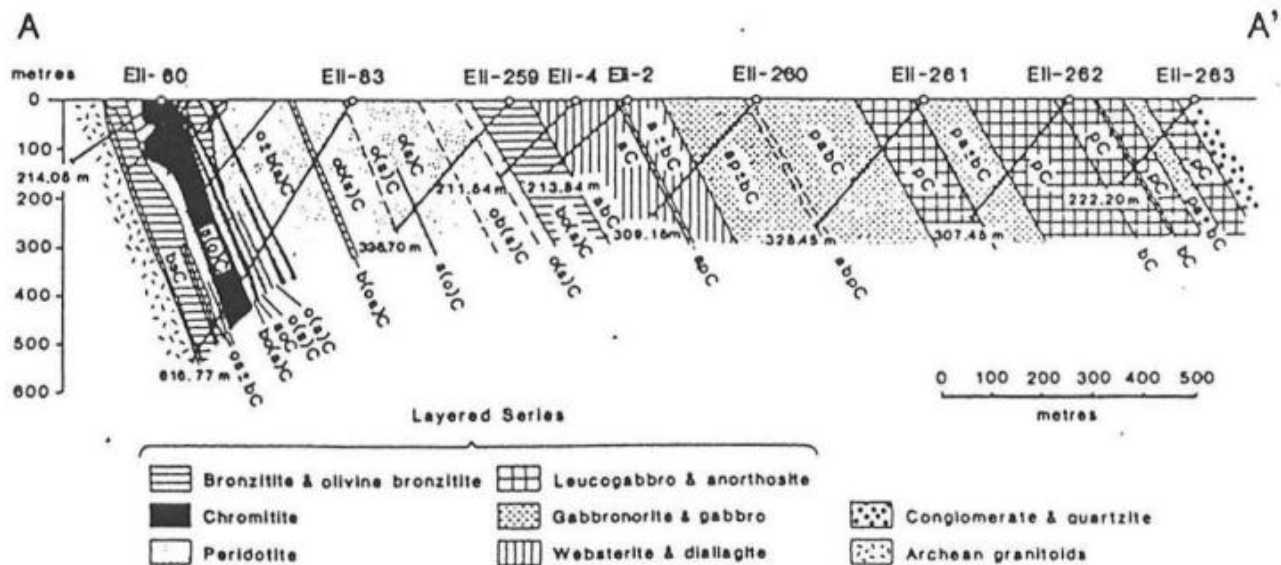
Kuva 4. Läpileikkaus A-A´ Kemin intruusiosta perustuen kairausprofiileihin. (Alapieti et al 1989)

Figure 5. Cross section of mafic Kemi intrusion based on drilling profiles

The Kemi intrusion in Finland is a good example of the geology of an ultramafic deposit. There is a good description of it in Alan Forsman's Master's thesis [32], from which the above image is copied. The image shows a cross-section of the intrusion viewed from the northeast. As a result of later folding, the intrusion has tilted at an angle of 70 degrees to the northwest, and the igneous rock types layered at the bottom of the magma chamber are in order from left to right. At first there is a less than kilometer-wide strip of ultramafic minerals such as peridotite, olivine, chromite and pyroxene. The proportion of pyroxene increases as you go to the right. After that comes a kilometer wide strip of mafic gabbro-like rock types, which are replaced on the top of the intrusion by leucogabbro and anorthosite. At the top and bottom of the intrusion, silicates have undergone metamorphosis and changed to serpentine, chlorite, amphibole, talc, and carbonates. Thus, the best aggregate is found in the partially metamorphosed ultramafic zone. The stove stone quarry has been located there. The unaltered gabbro zone in the middle could also be a promising location for energy storage. The Kemi intrusion at the mouth of the Kemijoki River and Luvia are located close to the nodes of the Finnish electricity grid, so electricity could be charged and discharged from several directions.

Some transformed mafic and ultramafic rock deposits may contain asbestos fibers. However, the minor asbestos content has not been found to be a significant safety problem in the utilization of those deposits[33].

[32] https://saunologia.b-cdn.net/wp-content/uploads/2018/02/1997-Forsman-kiuaskivet_silikaattimineraalit-SaunologiaS.pdf
[33] https://tupa.gtk.fi/julkaisu/tutkimusraportti/tr_127.pdf

Strength requirements of the crushed stone

The compacted crushed stone begins to compress when its maximum point load is exceeded. The maximum point load is generally considered to be about 5% of the intact rock compressive strength [34]. According to the sources mentioned above, after repeated heating and cooling cycles, the compressive strength of mafic rocks may decrease by about half. The crushed stone is compressed by its own weigh above and the compression between the side walls caused by the thermal expansion.

Only the upper half of the high-pressure storage will be heated to the top temperature. So, the less heat resistant felsic and intermediate aggregates can used elsewhere. The maximum compression of the crushed stone at the bottom of low-pressure storage is about 1.5 MPa, but only about 750 kPa in the top of the hot high-pressure store, because the pressure can be subtracted from the compression of the mass above it. The compression grows to about 1.5 MPa in the middle of high-pressure storage and 2.5 MPa at the bottom of it. At the operating temperatures of the low-pressure storage or in the bottom of high-pressure storage, the crushed stone does not lose its original compressive strength. A temporary exceeding of the maximum point load is not a problem for the operation of the energy storage if the compressed crushed stone reaches a new equilibrium state before its gas permeability decreases significantly.

Pressurization of thermal storages and control of thermal expansion of the crushed stone

The possible above-ground part of the storage could be pressure-insulated with welded stainless-steel sheets. The top of the high-pressure storage can be pressure-insulated with a soft steel. However, both steel insulations must be designed to withstand the thermal expansion of the crushed stone and the eventual vertical compaction of several meters during the plant's usage time.

The thermal expansion coefficient of basalt, gabbro and diabase is reported to be 5.4±1 10^{-6} m/K [35]. According to the simulation of the overhead storage, the average temperature difference between the empty and full storage would be approximately 570 °C, so the average volumetric change of the crushed stone would be at most 0.8%. Since the rock surrounding the storage is inelastic, the thermal expansion of the crushed stone can only direct upwards, so that the top of the storage could rise by 1 meter when the storage is fully charged. However, some of the thermal expansion only compacts the crushed stone. An example of this is fire bricks, which, due to their porous structure, have a thermal expansion coefficient of approximately 30% lower than that of ordinary solid bricks. The air space of the compacted crushed stone is significantly larger than the porosity of the fire bricks, so it can be assumed that its thermal expansion coefficient of compressed crushed stone may be less than 50% compared to solid rock. The difference probably depends on the porosity, as well as on the compression, the elasticity of the aggregate, the size of the particles and the settings of stone crusher, so the actual thermal expansion coefficient of the crushed stone must be measured on a case-by-case basis in the expected compression.

If the pipes coming from the turbomachines are fixed in the rock, there must be free space between them and the gas distribution channels in the crushed stone. In addition, the crushed stone of the high-pressure storage may compact by several percent over time, in which case the other side of the connection may sink several meters downward. Therefore, an accordion pipe should be used in the connection point. The hot high-pressure

---

[34] https://www.doria.fi/bitstream/handle/10024/121669/lts_2015-68_978-952-317-181-7.pdf?sequence=1&isAllowed=y

[35] https://www.britannica.com/science/rock-geology/Thermal-properties

and the cryogenic low-pressure pipe could be in the middle the low-pressure storage inside an insulated concrete pipe. In that case, thermal movement and compaction would not be a problem.

The friction of the crushed stone in the wall insulation must be about the same as the friction of the crushed stone in the storage. Otherwise, the thermal expansion and contraction may gradually pump up the insulation. When pressed, round-edged sieved sand slides between the fingers much more easily than angular rock ash that has passed through the same sieve. The friction therefore presumably depends on both the size of the fraction and the average angularity and aspect ratio of the particles.

Thermal expansion also raises and lowers the low-pressure storage, but significantly less, because the volume change of the high-pressure storage is more widely distributed there, and its thermal movement is also smaller and opposite to that of the high-pressure storage. The difference between the upper and lower temperatures of the low-pressure storage is about 570°C, and if the low-pressure storage is partially above ground, two-thirds of the expansion occurs laterally in its upper part. As a result of the opposite thermal movement of the storages, most of the thermal expansion of the low-pressure storage occurs downwards, but nevertheless, the external wall must be designed not be broken by the thermal expansion.

The radius of the above-ground storage is on average 140 meters, and the coefficient of thermal expansion of the granite is on average 7 10 $^{-6}$ m/K, so a temperature change of 570°C could push the sidewall outwards by up to 25 centimeters if about 50% of the rock heat capacity can be utilized. When this is repeated, for example, 50 times, the above-ground part of the storage could gradually spread by almost 12 meters and at the same time the above-ground part would lower by several meters. However, the expansion would require that the crushed stone particles would have continuous horizontal contact between heating and cooling cycles. I consider that quite unlikely. The above-ground part of the low-pressure storage would probably widen outwards perhaps 10–20 centimeters per year. That can be handled by the structural design of the storage walls and roof.

The thermal expansion won't be any structural problem, if the extra above ground crushed stone is sold out or the If the storage is made inside an existing pit and the whole storage can be enclosed inside rock walls. That is the default design because of its structural simplicity. There are plenty of closed quarries and mines that could be reused as underground thermal energy storage.

The gas barrier above the hot upper high-pressure storage can be made of soft, very low-carbon mild steel, which becomes elastic at the operating temperature of the upper high-pressure storage and thus adapts to its vertical thermal movement. The central part of the upper high-pressure storage may rise above its edge, but the crushed stone of the storage can expand upward perhaps half meter in relation to the surrounding rock (with 50 % utilization). In the cooler insulation layer at the edge, the steel can be replaced first with an aluminum alloy as the temperature drops, then with a mixture of pure aluminum and load-bearing crushed stone, and right near the rock, when the temperature drops below 200 °C, with an airtight mixture of crushed stone and technical rubber (or bitumen) melted together. At best, the long-term maximum operating temperature of heat-resistant technical rubbers is slightly above 200 °C. At that temperature, pure aluminum is probably still sufficiently malleable, so by changing the material, so the gas-tight pressure insulation can be extended to the rock walls. The softness of steel and aluminum depends on their additives such as carbon or silicon and heat treatment. The toughness of soft insulation layers can be improved by mixing, for example, carbon fiber strands into them, and their compressive strength can be improved by mixing them with a uniform size of good quality crushed stone, which prevents the soft pressure insulation from moving laterally. Above and below the insulation layer, the crushed stone fraction must be sufficiently fine so that the pressure does not push soft metal or rubber uncontrollably into the crushed stone.

The gas barrier of the steel surface above the upper high-pressure storage can be ensured by a layer of highly compacted load-bearing crushed stone and crushed biotite, which partially melts and becomes plastic at operating temperature. The melting of biotite minerals begins about at 800 °C [36]. The permeability of a one-meter-thick backup layer may at best be even lower than that of a few millimeters of steel plate [37]. Under compression and heat, the mixture will probably become completely gas-impermeable if at least 20% of its minerals either melt or become plastic, completely filling the air space of the compacted crushed stone.

The cracks and surfaces of the rock walls of the storage can be sprayed and injected with concrete to make them gas tight and waterproof. At the same time, it enables very steep slopes and improves safety of the workers. In very broken areas, a continuous steel plate anchored to the rock can be left inside the sprayed concrete. The rock can also be strengthened and made gas-tight by freezing it below the groundwater level. This may also have to be done if the storage is penetrated by an active rock movement joint that cannot be concreted with certainty to make it gas tight. Freezing is used to strengthen the rock in rock construction. The insulation thickness above is defined so that the continuous heat leakage of a full storage is 7 MW. Of this, perhaps about 4 MW leaks into the rock. When the cooling capacity of the rock piping is dimensioned sufficiently large, rock freezing could be done almost free of charge in northern winter. Continuous freezing with a heat pump would require less than 1 MW of power, because the average temperature difference would probably be less than 20 °C.

Structure and implementation of a separate cold pressure storage made of crushed ice

The simulation of the operating storage shows that its capacity almost doubles when a separate cold storage made of crushed ice is added to store cryogenic cold. The ice storage would have about the same volumetric size, but half the weight of the actual low-pressure storage made of crushed stone. The volumetric heat capacity of crushed ice is approximately 1.5 times that of crushed stone at the nitrogen vaporization temperature of the low-pressure storage (78 K). However, the specific heat capacities of different rock types vary somewhat, so the ratio depends on the composition of the crushed stone in the low-pressure storage and its porosity.

In the simulation example, the ice crushed stone temperature at the bottom is always below 80 K. The ice at the top of the storage reaches its maximum temperature only when the energy storage is completely empty, which is a very rare situation in normal use. When the storage is simulated with the default parameters, the maximum temperature at the top of the crushed ice storage is 218 K immediately after the storage reset, but it gradually increases during long-term use. The yield strength of compacted crushed stone is about 5% of compressive strength of the rock. However, ice is significantly more plastic compared to crushed stone, so the yield strength of solid ice it must be used instead of the compressive strength when calculating the yield strength of crushed ice. Based on measurements, the yield strength of an ice crystal increases almost linearly

[36]
https://www.researchgate.net/publication/259049396_Experimental_melting_of_biotite_plagioclase_quartz_muscovite_assemblages_and_implications_for_crustal_melting
[37] Ranges of common intrinsic permeabilities https://en.wikipedia.org/wiki/Permeability_(materials_science)

with decreasing temperature [38]. According to the source, the yield strength of ice is 40 MPa at 77 K and 10 MPa at 200

The highest temperature of the crushed ice at the top of the storage was 241 K and at the bottom 79 K after a simulation of 20 months continuous operation. In the middle, the maximum temperature increase accelerates as the top of the storage is approached. The most critical place in terms of load-bearing capacity is probably the bottom of the crushed ice storage. There the compression is approximately 0.4 MPa, which is below its yield strength 2 MPa by a large safety margin (40 MPa · 5 %).

A crushed ice storage is most economical to build from natural ice collected from nearby sources. Cooling 6.5 million tons ice from water would require almost 0.6 terawatt-hours of cooling energy. In addition, the capital cost of the massive cooling equipment required would probably be in the hundreds of millions. Instead, cooling the natural ice to 77 K can be done using the storage's own equipment while the storage is being charged to its initial state before the first charge. The enthalpy change of ice from 273 K to 78 K (275 kJ/kg) is less than the melting heat of ice, 333 kJ/kg.

The ice storage can be built partly with the same machines as the actual thermal storage made of crushed stone: large trucks, loaders and crushers used in open pit mines. In addition, long-range diggers, possibly fixed or mounted on rails, are needed to lift the ice pushed by tugboats to the shore. The ice storage can be pressure-insulated with a wet mixture of the soil in the area and the remaining fine crushed stone, which is frozen into a gas-impermeable layer after spreading. The outside of the insulation layer must be a flexible metal plate or any other elastic membrane that is impermeable to water vapor. The XPS insulation could be used in its temperature range. Biochar, stone wool or wood fiber insulation could be used elsewhere. In the bottom they could be mixed with uniform-sized crushed stone. The ice must naturally be processed in mid-winter, when natural ice is available. If the average thickness of the natural ice is 0.5 meters, then the required collection area would be at least 13 km^2. In inland waters, natural ice must be broken into blocks with light machinery, but at sea it can be done with an icebreaker. The current of the river, the wind or a boom pulled or pushed by tugs could push the broken ice onto the shore, within reach of the excavator, which dumps them on the shore to dry before crushing and transportation.

The filling of the circular ice storage proceeds from the walls to the center, so that the side walls are first raised and frozen in sync with the ice. The installation of the upper channel elements and roof insulation begins from the walls towards the center as soon as the ice reaches its final height. The crushed and screened ice is driven to the site by large mining trucks and spread on a safe slope by loaders or bulldozers. During the filling, the ice could be cooled to a load-bearing capacity by heating the outside air with the main compressor, which is first cooled in heat exchanger to about 300 Kelvin and then in a cooling turbine to about 130 Kelvin. The hot air from the heat exchanger preheats the crushed stone in the low-pressure storage to the target temperature of the empty low-pressure storage. Cold air from the cooling turbine is directed to the bottom of the circular crushed ice storage, from where it flows through the crushed ice up and into the center. The cold air flowing over the end walls of the storage accelerates the freezing of the soil on the outer edge.

Energy storage simulation and design program

---

[38]https://agupubs.onlinelibrary.wiley.com/doi/full/10.1029/2019JE006217

The energy storage simulation and design program is a research and design tool built on top of the JavaScript adaptation of the public Coolprop (http://coolprop.org/) thermodynamics library. All essential variables affecting the construction, size, power and costs of an energy storage are editable input parameters. The software has been expanded in several stages, when it has been a need to test new ideas, design the turbomachines of the plant, predict their efficiencies and map possible technical problems. The most important algorithms used in the storage design are briefly described here. The HTML page of the program and the JavaScript source code it contains, which may be somewhat difficult to understand, can be read directly from the server. The code contains some references to scientific articles from which the algorithms used have been extracted. The gases supported by the Coolprop library, their sources and allowed pressures and temperatures are listed in the List of Fluids section at http://www.coolprop.org/fluid_properties/PurePseudoPure.html . For example, the maximum allowed temperature for methane is 625 K, so the program sets the upper temperature of the storage to 623 Kelvin if methane is selected as the working fluid.

The program is published at https://anttisaarenheimo.github.io/ .

Simulation of compressor and turbine operation

The ideal gas equation cannot be used with real gases if the pressure is very high, if the gas is wet, or if its temperature close to the saturation temperature. Therefore, thermodynamic libraries are used to simulate the operation of compressors and turbines. They provide very accurate results under all conditions. In its simplest form, the simulation is performed by calculating four properties of the gas in a loop, when the turbomachine's average stage efficiency η is known: pressure P (Pa), temperature T (K), mass enthalpy h (J/kg), and mass entropy s (J/kg/K). The system can be assumed to be closed, because the mass flow and enthalpy change are very large compared to the heat losses in the turbomachinery and pipes.

The program uses the easy-to-use high-level PropsSI interface of the Coolprop library, where two gas properties are used to query a third property. When the efficiency of a single stage of a compressor or turbine is η, the positive or negative enthalpy change Δh, the initial state of the gas before the compressor or turbine stage (T1, P1, h1, s1) and the final state after the stage (T2, P2, h2, s2). For a compressor, the efficiency is the part of the enthalpy that changes the pressure while the entropy remains constant. The rest of the enthalpy change is converted directly into heat, which in turn increases the temperature and entropy of the gas in the final state. Thus, the change in one stage is for nitrogen gas:

P2 = PropsSI ('P', 'H', h1+ Δh · η, 'S', s1, 'Nitrogen')

h2 = h1 + Δh

T2 = PropsSI ('T', 'H', h2, 'P', P2, 'Nitrogen')

s2 = PropsSI ('S', 'H', h2, 'P', P2, 'Nitrogen')

In the case of a compressor stage, Δh is the work added into the system, which with the part determined by the efficiency increases the pressure. In the case of a turbine, Δh · η is the work produced by the pressure drop in turbine, while (1- η) · Δh is converted to heat.

There are several variations of that calculation because the change in enthalpy is not always known in advance. For example, the compressor must be simulated backwards with efficiency 1/η starting from its final pressure and temperature.

Calculating the dimensions of an energy storage

An underground energy storage is assumed to be shaped like a cut cone. That shape minimizes construction costs and heat loss. At the same time, it enables pressurizing the hot high-pressure storage with the mass of the low-pressure storage.

The main dimensioning parameters of the energy storage are the amount of crushed stone in tons, the low pressure and pressure ratio in charge, the temperature of the hot high-pressure storage, the efficiencies of turbines and compressors, density of the rocks used for the high- and low-pressure storages, specific heat capacity, steepness of the wall, the sieve spacings of the crushed stone of the upper and lower pressure storage, the maximum steepness of the above-ground heap and the permitted heat leakage per square meter. It is assumed than an underground storage (choice: no top fill) is made in a closed quarry or open pit mainly from its waste rock, and an above ground storage (choice: Top fill used as storage) is mined into the rock, and all aggregate would be used to build the energy storage.

At first the average volume specific heat capacity is calculated is for the temperature ranges of both storages. The specific heat capacity of the rock depends on the temperature. At low temperatures, this relationship is best described by the Debye model. According to the model,[39] the Debye temperature can be calculated from the maximum of the crystal vibration of solid elements and minerals. The ratio of this to the measurement temperature can be used to normalize the temperature dependence of the specific heat capacities of solids to the same curve (see the next figure). The most important thing from the point of view of energy storage is the reduction of the specific heat capacity to zero when the temperature is approaching absolute zero, and the fact that the ability of minerals to store very cold is inversely proportional to their Debye temperature. However, the Debye temperature is not constant but usually increases at the same time as the measurement temperature. For example, the Debye temperature of ice increases from 222 Kelvin to 300 Kelvin when the measurement temperature increases from 0 to 100 Kelvin. The Debye temperature of silicate minerals is typically between 500 and 1200 Kelvin measured at room temperature[40].

---

[39]https://en.wikipedia.org/wiki/Debye_model
[40] https://pubs.usgs.gov/of/1988/0663/report.pdf
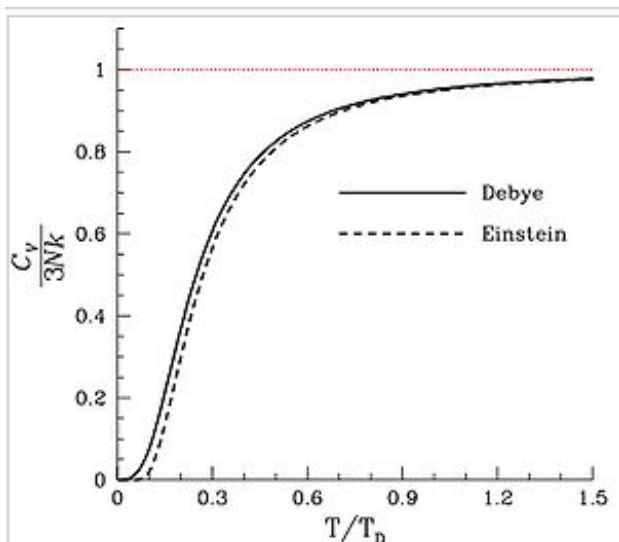
Debye vs. Einstein. Predicted heat capacity as a function of temperature.
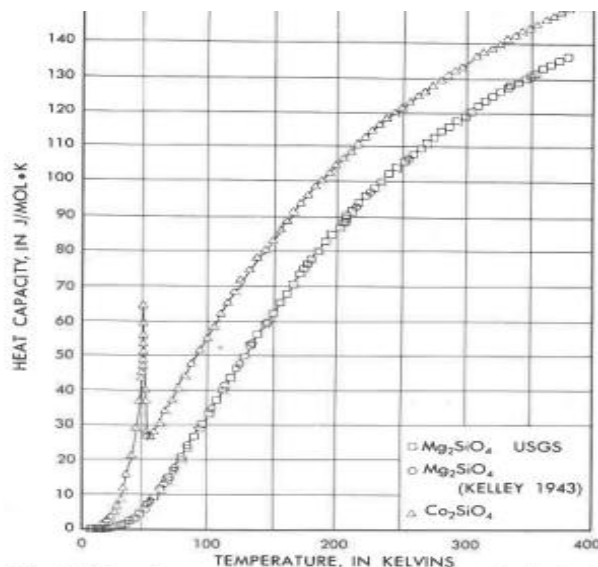
Fig. 1. Experimental molar heat capacity of synthetic single crystal Mg₂SiO₄ (forsterite), formula weight 140.694 g mol⁻¹ and synthetic single crystal Co₂SiO₄ formula weight 209.950 g mol⁻¹

Above are the measured specific heat capacities of two ultramafic minerals, forsterite (Mg_2SiO_4, T_D 758 K) and cobalt olivine (Co_2SiO_4, T_D 548 K). The Debye temperature cannot be defined for ordinary rocks[41], because they consist of several minerals, the mutual ratios of which can vary by tens of percent.

In the next figure on the left are the measured specific heat capacities of several rock samples at high temperatures, and on the right their normalized distribution from the study A Review and Evaluation of Specific Heat Capacities of Rocks, Minerals , and Subsurface Fluids . Part 1: Minerals and Nonporous Rocks [42].

[41] https://rruff.geo.arizona.edu/doclib/am/vol67/AM67_470.pdf

[42]

https://www.researchgate.net/publication/226113239_A_Review_and_Evaluation_of_Specific_Heat_Capacities_of_Rocks_Minerals_and_Subsurface_Fluids_Part_1_Minerals_and_Nonporous_Rocks
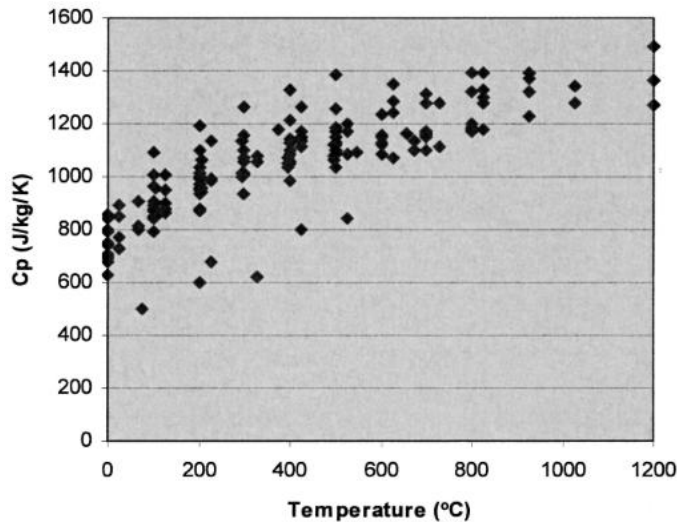
Figure 11. Measured specific heat capacities plotted as a function of temperature for all nonporous rock samples in Table 2, showing the general increase in heat capacity with increasing temperature. Data from Kappelmeyer and Haenel (1971), Tkach and Yurchak (1972), Roy, Beck, and Touloukian (1981), Čermák and Rybach (1982), and Robertson and Hemingway (1995).
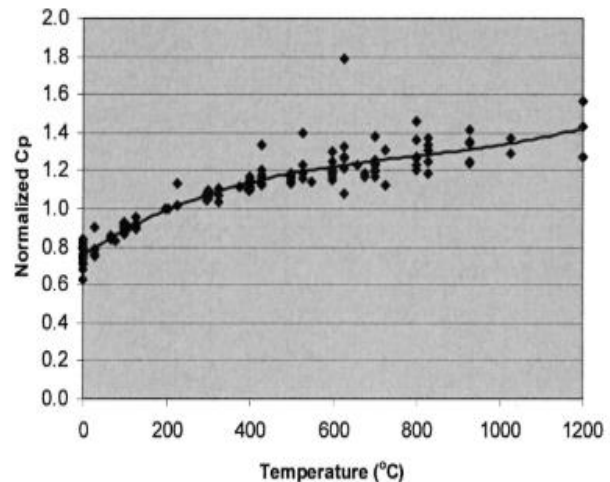
Figure 13. Normalized specific heat capacities plotted as a function of temperature for the same nonporous rocks shown in Figure 11. Normalization was carried out by dividing all reported specific heat capacities by the value for the same rock at 200°C. Line represents best-fit third-order polynomial. Correlation coefficient $r^2 = 0.93$.

The calculation of the specific heat capacity of the thermal storage has been simplified by following the Debye curve of 650 Kelvin linearly through three reference points below 20 °C (heat capasity at 77 K: 23%, at 200 K: 78%, at 293 K: 100%) and the normalized curve of the aggregates above through three reference points above (heat capacity at 473 K: 125%, at 773 K: 150%, at 1023 K: 163%). The thermal capacity of the storage is obtained by calculating the average specific heat capacity of the temperature range of the high-pressure storage, multiplying it by the temperature range and mass of the storage and finally multiplying it by the heat capacity utilization factor parameter. Its default value is 0.59, or 0.42 if the cryogenic cold is stored only to crushed stone. The efficiency factor determines how much of the maximum capacity of the high-pressure storage can be used before its round-trip efficiency begins to decrease significantly. These factors were selected by simulating the operation of the storage.

The calculation of the density of the crushed stone is based on the sieve spacings given as parameters, and on the assumption that the cubic weight of the compacted 0–100 mm aggregate would be 2.1/2.65 of the original stone cube weight, and the density of a completely uniform compacted crushed stone would be 1.5/2.65 of the stone density and the airiness 0.434. Based on this, the ratio of the density of an evenly distributed min/max compacted crushed stone fraction to the stone density is (1.5 + (2.1-1.5) · (1-min/max))/ 2.65, i.e. the smallest particle leaves an empty space in the crushed stone, which reduces the density and weight. 1.5 may be too large a number for the density of a uniformly compacted crushed stone, because elsewhere it is assumed that the airiness of a completely uniform insulating crushed stone is 0.5, which would mean a ratio of 2.65/2, i.e. 1.325. The densities of the crushed stone, of course, depend on the actual screen spacings used, the particle size, the average particle aspect ratio and distribution, the crusher settings and the splitting of the aggregate. The actual values can only be determined by measurement. Crushed stone with a rounder shape and a smaller particle aspect ratio has been found to pack more tightly, and the gas or liquid flow is faster[43]. Presumably, the

---

[43] https://www.ncbi.nlm.nih.gov/pmc/articles/PMC9458179/

point load carrying capacity of rounder particles is also better. Thus, with the right crusher and screen settings, the operation of the energy storage can be improved and probably also extend its service life.

Calculating the shape and dimensions of a storage is a typical multi-step heuristic algorithm, the optimal outcome of which is known in advance, but the many interacting variables make it impossible to solve as an equation. The energy storage must meet the following requirements:

1. The available thermal capacities of the high-pressure and low-pressure storages must be symmetrical, i.e. when the high-pressure storage is full of heat, the low-pressure storage is full of cold, and of course vice versa.
2. The above-ground part of the storage should preferably be completely above the upper pressure storage, i.e. it should not extend beyond the excavated rock.
3. The weight (in Newtons) per square meter of the upper low-pressure storage should be at least the maximum pressure of the high-pressure storage. The program assumes that the compacted crushed stone on the storage scale behaves like a liquid: only the mass directly above the high-pressure storage matters in the calculation. The actual gravitational compression force can be measured with the pressure sensors above the high-pressure storage.
4. The area of the storage's external surface should be as small as possible to minimize the costs and heat leak.

At first, an initial weight is calculated using an educated guess about the dimensions of the storage. The algorithm makes necessary corrections to the dimensions, and the calculation is made again. If the storage has a high pressure (such as 2000 kPa), this is repeated until the safety margin of the result is less than 5% above or below 100 kPa. If the pressure is low, then the surface area is minimized.

Along with the storage dimensions, the program calculates the proportion of gas to be liquefied during the charge, which is 0.2% of the mass flow with the default parameters for nitrogen and 0.033% for argon.

Simulation of energy storage operation

The operation of the designed energy storage can be simulated programmatically. The simulation algorithm divides the crushed stone and ice into horizontal thin slices (default 10 cm), which are assumed to have the same temperature. In the simulation, each slice is heated or cooled by the forced convection of gas for a given time (default 900 seconds) so that the end temperature of the gas and the solid in the block would be the same. In reality, of course, this is not the case, and if desired, the actual heat exchange coefficient between the crushed stone and the gas can be enabled before simulation as presented in the literature[44], and the temperature difference between the gas and crushed stone is derived from it. However, using the heat exchange coefficient of the gas and crushed stone does not significantly change the efficiency of the storage based on the simulation, or even its maximum capacity, because the temperature of the gas flowing out normally deviates from the temperature of the crushed stone or ice by fractions of a degree at most. Only when the storage is almost empty or full can the temperature difference of the hot gas coming out increase to 1–2 degrees.

---

[44] https://shop.tarjomeplus.com/UploadFileEn/TPLUS_EN_4259.pdf

The internal heat leak of the storage (W/m/K) is also included in the simulation, so that the known heat transfer coefficient of the crushed stone[45] in room temperature is split to the conductive heat transfer and heat transfer by radiation. In the simulation, the heat radiation is scaled to the actual temperature and median particle size of the crushed stone. Although heat radiation increases the heat transfer coefficient of the crushed stone in hot high-pressure storage by an order of magnitude higher than in the room temperature, it does not seem to have a significant effect on the storage capacity or even the energy storage time, because the internal heat leak is very small compared to the heat capacity of the storage, and on the other hand because the internal heat leak has an effect only if it changes the temperature of the gas leaving the storage, i.e. only when the storage is almost empty or full. Based on the simulation, even months of downtime do not significantly equalize the internal temperature differences.

The simulation aims to determine the actual maximum capacity of the storage and the maximum number of charging and discharge cycles before it is worth restoring the storage to its initial state. The restoration to its initial state occurs in such a way that the low-pressure storage is first cooled near to its lowest cryogenic temperature, and in the following discharge the same is done to the high-pressure storage, whereby the heat exchange areas gradually widened by convection almost completely disappear. Additional resistors placed in the crushed stone of the upper part of the low-pressure storage can be used to preheat the cooled gas to the level required by the compressor pressure difference. Additional heating of the gas can also be done by increasing the pressure ratio and deliberately worsening the compressor efficiency.
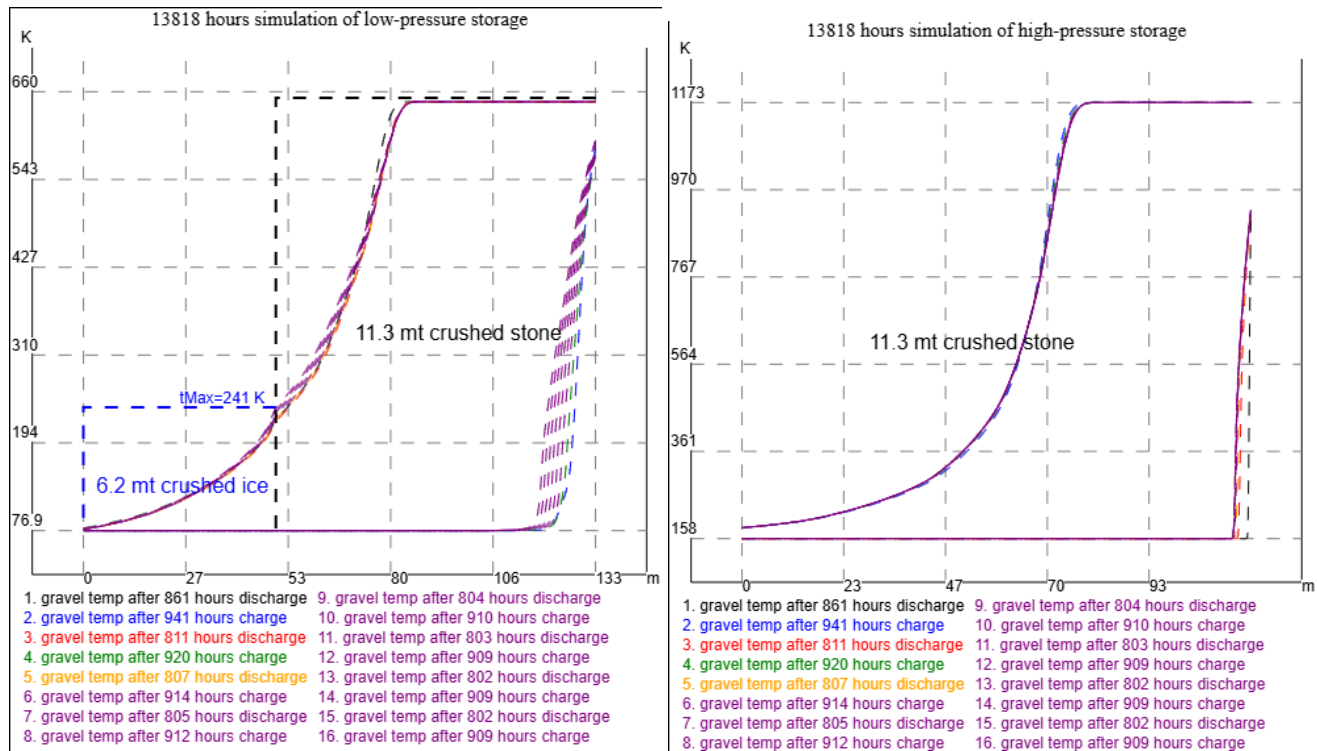
The diagrams above show the final temperatures of the crushed stone and ice by height in the end of eight consecutive full charging and discharge cycles. The discharging or charging has been continued in the simulation until the exit temperature of the high-pressure gas has exceeded by 20 K the on-design minimum

[45] https://trepo.tuni.fi/bitstream/handle/10024/135911/Convective_heat_transfer_in_crushed.pdf?sequence=1

temperature or fallen 250 K below the on-design high temperature 1173 K. The simulation duration is about 19 months, which could correspond to approximately two years of production use. However, in a real production, the charge does not fluctuate between the two extremes, so the contraction of the maximum capacity caused by the widening of the heat exchange area is probably faster than in this simulation. In the real production, the high- and low-pressure storages should probably be cooled once a year to their minimum temperatures to restore the maximum capacity of the energy storage.
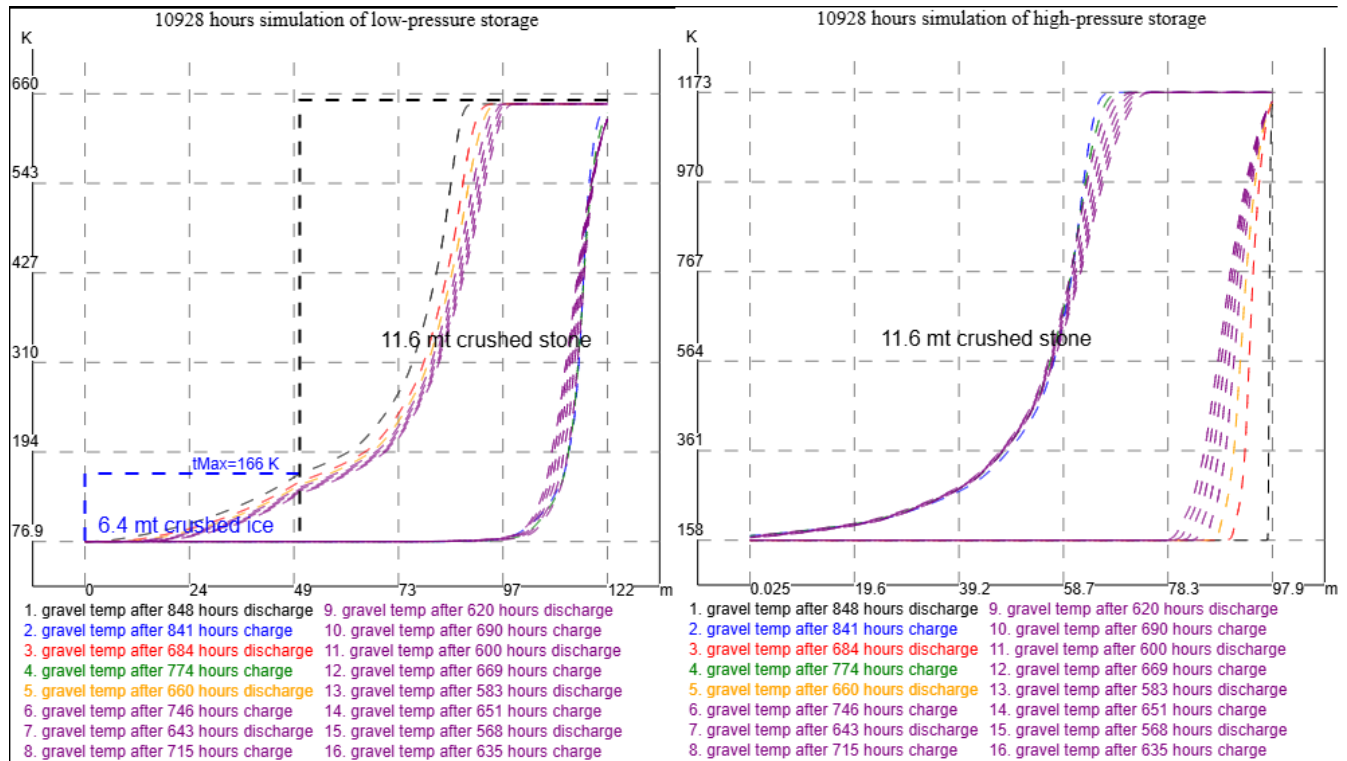
Figure 6. Storage simulation with a tight range of exit temperatures

The storage capacity is considerably less if the range of allowed exit temperatures is very small as can be seen in the previous figure. Turbomachine is operating off-design when only its inlet temperature (storage exit temperature in this case) is less than the design value. That can be compensated by increasing the pressure ratio until the stage enthalpy change is the on-design value. Unfortunately, that is possible only for the other side of Brayton cycle because it is impossible to have equal relative exit temperatures differences for high- and low-pressure storages. The problem can be resolved by using frequency controllers to adjust the rotational frequencies of the cryogenic turbomachines and adjusting the pressure ratio of the storages for the main synchronized turbomachines. That would mean, that the cryogenic turbomachines and the heat pump would share the same synchronized motor-generator, that could be optionally controlled by a set of frequency controllers. Such design with additional liquid storage capacity would make possible to adjust the produced and consumed power by the demand and supply or the grid. The additional liquid nitrogen or argon storage capacity would be used adjust the storage pressures for the sold or bought power. The increased fluid pressure and density increases the mass-flow and the power produced or consumed by a turbomachine, but does not change its on-design state, if the pressure ratio and inlet temperature are unchanged.

Dimensioning of pipelines

The allowable pressure drop in the pipes between the storages and the turbo machines is one of the design parameters of the system. Its default value is 1%. Based on the given allowable pressure drop, the diameters of the pipes and the gas velocity in the pipe are calculated. The actual pressure drop is calculated using the Darcy-Weisbach equation. The friction factor f used in the equation is calculated as presented by Tkachenko and Mileikovskyi in 2020. The value of epsilon (ε) is 0.025 (steel, structural or forged), which is probably an order of magnitude worse than the typical value of steel pipes. On the other hand, pipe bends, welds, dust filters and valves each increase the pressure drop, so it probably gives a good estimation of the actual value. The algorithm is again heuristic because the desired result is known, i.e. the allowed pressure-drop, but the equation is too complex to directly solve the only variable affecting it, i.e. the diameter of the pipe.

Calculation of gas flow resistance in crushed stone

Air flow in the crushed stone has apparently not been studied very much, because with the search words used, only a seminar presentation of a research project was found[46]. In that study, the radon ventilation of the subfloor was studied with two EU standard crushed stones 6/12 and 10/20. The conclusion of the study was that for the crushed stone, the Darcy-Forchheimer equation best corresponds to the measurement results. The superiority of the equation is self-evident, because the laminar and turbulent parts of the equation have their own measurement-based coefficients depending on the properties of the crushed stone.

The Darcy-Forchheimer equation is: $\Delta P/L = \mu /k \cdot v + c/k \cdot v^2$, where ΔP is the pressure change (Pa), L is the distance (m), μ is the fluid viscosity (Pa·s), k the measured permeability of the crushed stone (m^2), v velocity (m/s) and c the measured Forchheimer factor.

The study measured the permeability of the crushed stones, the Forchheimer factor and the pressure drop at air flow speeds of 0.015–0.5 m/s. The gas flow velocity range of the energy storage (0.02–0.15 m/s) is within those speeds, but the min and max particle size of the crushed stones and the porosity differ significantly from the EU standard crushed stones in the study. The crushed stones measured in the study were apparently uncompacted because their porosity was 0.40 and 0.51. Therefore, in the calculation of the pressure drop in the storages, the values measured for the 20/40 crushed stone of the study are used as a fixed point. The laminar (200) and turbulence coefficient (1630) are scaled for the selected crushed stone type and its porosity using Erguin equation[47]:

$\Delta P/L = v \cdot (150 \cdot \mu / D_p^2) \cdot (1-n)^2 /n^3 + v^2 \cdot (1.75 \cdot \rho / D_p) \cdot (1-n)/n^3$, where v is velocity (m/s), μ is viscosity (Pa·s), D_p is the average diameter of the particles in the crushed stone, n is the porosity of the crushed stone and ρ is the gas density.

The viscosity and density of the air of study are scaled to the selected working fluid at the pressure and temperature of the storage part.

46
https://www.researchgate.net/publication/322140487_Behaviour_study_of_airflow_through_gravels_based_on_laboratory_experimentation_and_contrast_with_FEM_models
[47] https://en.wikipedia.org/wiki/Ergun_equation

The program calculates the pressure drops separately for both storages and for their hot and cold sections. The calculation of the electricity round-trip efficiency assumes that the storage is half full, which is the worst case, because it is the maximum possible charging level (about 50%) based on the simulation and the pressure drop in the cold side is almost zero.

Strength calculation of compressor and turbine blades

The relative blade maximum thickness is a main factor in the profile loss of a compressor stage. So, the blade maximum thickness, width and length must be known to be able calculate the stage efficiency.

The greatest stress is placed on the rotor blades. The blade stress mainly consists of centrifugal force and bending caused by the pressure difference. The tensile stress of the centrifugal force depends solely on the mass of the blade and its distribution along its length. So, the algorithm calculates first the torques applied to the middle of the gas flow and the hub. The maximum thicknesses of the blade at the mean flow and rotor hub are obtained from their torques and the maximum permissible tensile stress of the selected material in the temperature of the blade. When the given minimum thickness of the blade at the tip (default 1 mm for compressors or 3 mm for turbines) is known, the ratio of the cross-sectional areas of the tip and hub can be obtained, from which the centrifugal force applied to the hub can be calculated. If the centrifugal force exceeds the permissible tensile stress, the thickness of the blade at the hub and center is increased.

The torque acting on the blade can be calculated from the power consumed (or produced) by the stage and from the blade angles at the measurement points. The compressor loss model (described later) is used to calculate the blade angles at the hub, in the middle of the gas flow and in the middle of the outer half of the gas flow. The torque of the bending is calculated by dividing the blade span to 10 parts each having 10% of the flow and force F accelerating the gas. The total force F is fluid mass flow · velocity change/ (1 - reaction). The velocity change is the constant axial velocity·(tan(α2)- tan(α1)), where α1 absolute angle in blade inlet and α2 in blade exit. The force bending the blade in the hub is obtained by dividing the transverse force F by the cosine of the blade angle at the measurement point, multiplying it by the cosine of the difference between the angle of the hub and the center of the flow, and finally multiplying it by the difference between the radii of each center of the flow and the hub. The torque acting on the median of the blade is calculated in a similar way.

The section modulus of the blade is integrated by dividing NACA 63A010 airfoil[48] to small rectangles. The section modulus of rectangle is $S = b \cdot t^2/6$ [49], where t is the thickness and b the width of the rectangle. The bending resistance therefore increases as the square power of the thickness. The maximum torque is $M_y = S \cdot \sigma_y$, where σ_y is the maximum allowable tensile stress. The width is calculated as $b = s \cdot c$, i.e. the solidity multiplied by the chord length of the blade. The solidity s is the chord length divided by the distance of between blades. The chord length is assumed to increase from the hub to the tip in the ratio 1/cosine of the stagger angle of the blade. The actual section modulus of the blade depends on its cross-sectional shape. It must be at least a few percents greater than the used bending resistance of the rectangle.

---

[48] http://airfoiltools.com/airfoil/details?airfoil=n63010a-il#polars
[49]https://en.wikipedia.org/wiki/Section_modulus

The centrifugal force acting on a rotating blade is calculated by the formula $\sigma_{ct} = 0.5 \cdot \rho_b \cdot U_t^{\,2} \cdot K \cdot (1\text{-}b^2)$ [50], where ρ_b is the density of the material, U_t is the speed of rotation in the rotor tip, b is the ratio of the radii of the rotor hub to the tip. The coefficient K is calculated by the formula K=1 − (1 − d) · (2 − b − b²) / (3 · (1-b)), where d is the above-mentioned ratio of the blade tip and hub cross-sections. If the centrifugal force exceeds the maximum permissible tensile stress, the blade thickness at the hub is increased until d is sufficiently small.

The heuristic algorithm calculates a preliminary estimate of the blade shape and relative maximum thickness at first. Then it uses the stage efficiency prediction (by loss model) and blade stagger angles to get the exact results. The implementation can be found in a function *getDeltaH.*

Comparing the working fluids

Air and other mixed gases are not suitable as a working fluid for this system because they do not have an exact saturation temperature. Each gas in the mixture saturates at its own changing partial pressure and temperature. Carbon dioxide is not suitable because its triple point pressure is over five atm, which would be far too high pressure for the low-pressure storage. Hot oxygen, on the other hand, would react with the crushed stones, turbomachines, pipes and with possible biochar insulation.

Argon, helium, methane, nitrogen or hydrogen are possible working fluids of the system. Of these, nitrogen has the best electricity round-trip efficiency of 88.8% with default input parameters and a very good storage capacity. In addition, the properties of nitrogen and air are very similar, so existing large industrial compressor and turbine designs can easily be adapted to nitrogen. The storage simulation with default parameters calculates the total weight of nitrogen gas to be 26500 tons. That is less than 0.1% of the worldwide production of industrial nitrogen gas and the on-site production cost could be about 3 million euros. The production cost depends mainly on the price of the electricity.

The calculated round-trip efficiencies for argon are about 0.8% less than for nitrogen and the estimated cost of its turbomachinery (based on number of blades) is about the same as of nitrogen, but its heat exchangers are 50% bigger and more expensive. It usually has better storage capacity than nitrogen. Argon has the advantage of lower high pressure due to the lower pressure ratio of the noble gas. The lowest operation temperature of cryogenic argon compressor drops almost to its freezing point when its pressure ratio exceeds 10. The storage simulation with the default parameters calculates the total weight of needed argon to be 21000 tons. That would be about 3% of the current worldwide production of industrial argon gas, but the availability and cost of argon should not be a problem because argon is a side product when oxygen is produced about 100 million tons in the cryogenic air distillation process[51]. Thus, its annual worldwide production could expand up to 4 million tons. The lowest published factory price of liquid argon is only US$ 100/ton (in China). The shipping to the site in a small LNG tanker would increase the cost perhaps 50%. So, the cost of argon gas may be about the same as on-site produced nitrogen, and the capital costs of energy storage designed for argon is probably lower.

The high temperature of methane is set 625 K because it is the maximum temperature of methane in Coolprop, Methane is stable up to 900 °C, but it is usually more expensive gas than argon or nitrogen and its autoignition

---

[50] Module_04_-_Axial_Flow_Comp.pdf (polymtl.ca)
[51] https://en.wikipedia.org/wiki/Air_separation

temperature with air is 537 °C. It is possible to design efficient methane turbomachines, but the higher dew point and lower max temperature decrease its round-trip efficiency few percents below nitrogen or argon.

Helium is not a practical choice because of the high cooling work at its low-pressure saturation point. In addition, as an expensive gas.

The physical properties of hydrogen make it a very challenging to design efficient commercial compressors or turbines for it. An example of this is the recently published counter-rotating hydrogen compressor concept by Siemens Energy [52]. It has a single-stage efficiency of 89% (i.e. polytropic efficiency), and the pressure ratio of its counter-rotating half is 1.09 (24 counter-rotating pairs create a pressure of 80 atmospheres, meaning the concept has a total of 48 stages and apparently the same number of motors). The concept is still in its design phase.

Motor-generators used in pumped hydro plants

The first pumped storage power plants were built at the beginning of the 20th century. Since then, their power and efficiency have been continuously improved by technological developments. Today, the largest pumped storage power plants usually consist of a reversible pump turbine and a synchronous motor-generator. Voith Hydro is the largest supplier of pumped storage power plants, and its technical solutions and references are described in the brochure Harnessing the power of water with engineered reliability [53].

The most interesting from an energy storage perspective are Voith's motor-generator solutions, with outputs of up to 530 MVA (Bath County, USA, rpm 257). Most Voith references have only one speed, i.e. their motor-generator is synchronous. Thus, their speed is always a fraction of the grid frequency, and the number of pole pairs in their motor-generator varies between 5 and 14. Voith has also supplied asynchronous motor-generators, such as the largest 433 MVA unit in Europe (Frades II, Portugal, rpm 350–381). Voith supplies both induction[54] and frequency converter based asynchronous motor-generators.

The advantage of asynchronous motor-generators is their power control and self-starting. Large synchronous motors and motor-generators always require either an external or integrated starting system, or most often a combination of both[55]. Synchronous generators in large thermal power plants have usually two poles (rpm 3000 or 3600). The turbine and, if applicable, the compressor unit are directly connected to the generator shaft, i.e. their speed is determined by the network frequency. The efficiency of large synchronous generators is at best 99%. Power control is achieved by changing the pressure ratio and mass flow of the turbine. However, this adjustment usually comes at the expense of efficiency. Only in smaller power plants use a gearbox used between the generator and the turbine, because otherwise the small turbine would have too low rotational speed.

---

[52]Advanced Hydrogen Compressor for Hydrogen Storage Integrated with a Powerplant
https://www.osti.gov/servlets/purl/1874341
[53]https://voith.com/corp-en/11_06_Broschuere-Pumped-storage_einzeln.pdf
[54] https://en.wikipedia.org/wiki/Induction_motor
[55] https://en.wikipedia.org/wiki/Synchronous_motor

The world's largest induction motor made by GE in 2018 has a power of 80 MW and an efficiency up to 98.1%[56]. Either this is not completely true, or the big asynchronous motor-generators supplied by Voith are controlled with static frequency converters. The typical power range of frequency converters extends up to 10 MW, so for example the asynchronous 433 MVA unit of Frades II would be too big or them. However, in 2018, ABB has delivered a 4·103 MW static frequency converter system to the German railways, which had 4 different frequencies [57].

Voith's brochure does not state the efficiency of its references, but their pump turbines have a maximum power of 90% of the motor-generator power. This may mean that pumping is carried out at almost full power with the discharge power approximately equal to the turbine power, i.e., at most 90%. Voith motor-generators can be cooled with air or water. Air cooling can be used in generators in hydroelectric power plants even at high power levels, if their speed is low enough. Large thermal power generators of more than 60 MW directly connected to the grid frequency must use hydrogen cooling or a combination of hydrogen and water cooling[58]. Therefore, motor-generators in hydroelectric pumped storage plants cannot be used as such in thermal gas pumped storage plants, but their technical solutions are directly applicable there.

Turbine and compressor technology of current gas turbine power plants

According to Wikipedia, the single-stage efficiency [59]of axial compressors would be 0.92 at best, and the typical pressure ratio of industrial compressors is 1.05–1.2. This was probably true 40 years ago, but nowadays supersonic compressors of new large gas turbines reach 24–25 atm pressure in just 13–15 stages and a mass flow of 700–1000 kg/s [60]. A Chinese research team was able to improve the efficiency of the compressor's first stage of an old gas turbine model to 95% using CFD modeling and achieve[61]a pressure ratio of 1.5. This was probably an old Mitsubishi F model, and its original stage efficiency was 94%.

The compressor power of new gas turbines is at best less than 45% of the gross turbine power, and the turbine unit power is typically about twice the net power of the plant. For example, a 448 MW Mitsubishi M701JAC gas turbine could have a compressor power of about 400 MW, and its turbine unit power of about 900 MW. The list price of the M701JAC power unit alone was estimated to be $76 million [62]. If the compressor and turbine power of the energy storage is assumed to be, for example, 60% of the total price of a simple gas turbine package, then the unit price of its compressors and turbines power would be $35/kW.

Thanks to the complex cooling technology, the temperature of the gas turbines has been raised to almost 1700 °C. Nevertheless, the production of the compressed air required for cooling and extra cooling loss reduce the overall efficiency of the gas turbine. The efficiency of the turbine is also reduced by the relatively small number of stages (maximum 4), which inevitably increases the load factors of the individual stages and the torques of

[56] https://www.gevernova.com/power-conversion/news/ge-successfully-completed-no-load-testing-one-worlds-largest-80-megawatt-induction

[57] https://new.abb.com/news/detail/10379/worlds-most-powerful-rail-frequency-converter

[58]https://en.wikipedia.org/wiki/Hydrogen-cooled_turbo_generator

[59]Mitsubishi J-Type Technology https://www.mhi.co.jp/technology/review/pdf/e503/e503001.pdf

[60] https://en.wikipedia.org/wiki/Axial_compressor

[61]Optimization Design of Aspect Ratio and Solidity of a Heavy-Duty Gas Turbine Transonic Compressor Rotor https://www.mdpi.com/2075-1702/11/1/82

[62] https://tealgroup.com/images/TGCTOC/sample-wpsbim.pdf

the blades. For these reasons, the efficiency of the turbine equipment of commercial gas turbines is likely to be significantly below the maximum value of 0.97. Manufacturers only state the overall efficiency of the gas turbine power plant, which does not allow conclusions to be drawn about the efficiency of the compressor or turbine units of the plant. The tensile strength of common nickel alloys used in turbine and compressor rotor blades generally begins to decrease rapidly above 650 °C, and it is completely lost in most alloys at 1000 °C[63]. The blades of the first high-pressure stages of gas turbines are usually made of a directionally solidified nickel-tungsten alloy [64]. Its tensile strength remains unchanged up to 800 °C. When the tensile stress at the operating temperature is exceeded, the rotor blades must be cooled. Simpler internal cooling of the blade can be used if the temperature difference is not more than 100 °C. Above this, external cooling must be used, in which a thin layer of colder gas is directed onto the blade surface.

Performance limits of axial turbomachines

The study Performance Limits of Axial Turbomachine According to Stages[65] predicted 95.5% as the maximum efficiency for the analyzed upstream compressor stage. Correspondingly, the maximum efficiency of an uncooled optimized turbine stage would be 97.2%, according to the study. Its compressor and turbine losses distributed is shown in the next figure. The work did not document properly the used loss models, and its compressor profile loss prediction is more optimistic than the mean line loss model (by Koch & Smith) used in this work.
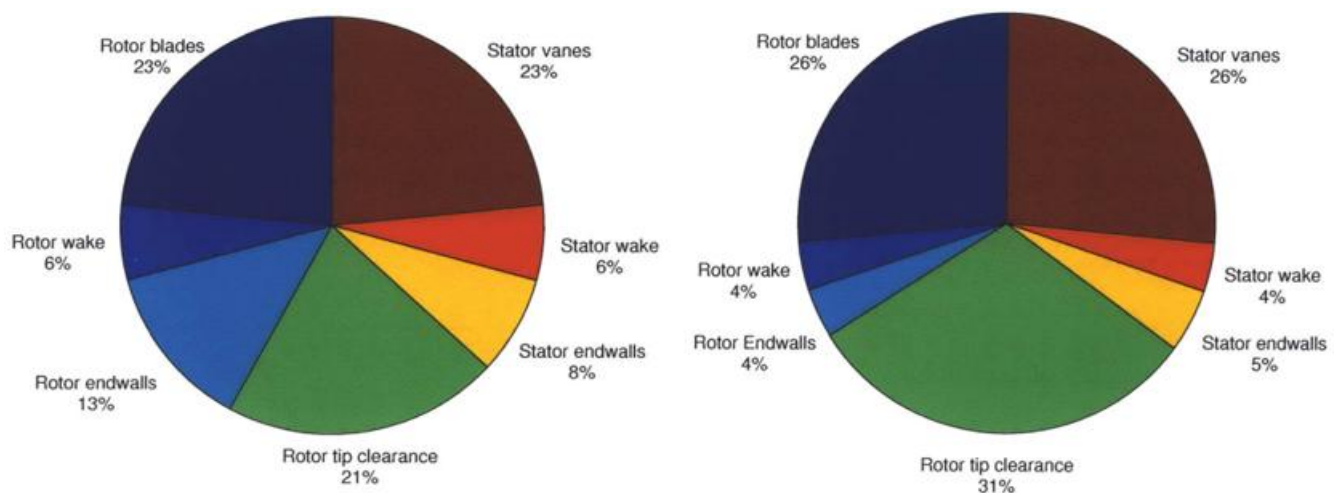
Figure 7. Losses of an optimized low-pressure compressor stage on the left and a turbine stage on the right according to the study "Performance Limits of Axial Turbomachine Stages"

Compressor's Reynold number was 500 000 and rotor tip clearance 1% of the blade length, typical for upstream stages. According to the used model, each 1% increase in the tip clearance decreased the efficiency of the stage by 1%. Other studies and measurements of physical devices have shown that the efficiency

---

[63] https://nickelinstitute.org/media/8d93486143182f5/nickel_incopub393_updated-june-2021.pdf

[64] https://upcommons.upc.edu/bitstream/handle/2117/350237/ANEXO%203-%20Materiales.pdf?sequence=2

[65] Performance Limits of Axial Turbomachine Stages https://core.ac.uk/download/pdf/4427598.pdf

decrease is as high as 2%. The large tip gap typical for downstream high-pressure stages is the main reason why their efficiency may be several percent lower than that of upstream stages.

Rotor blades, rotor wake, stator vanes and stator wake are included in the profile loss of the stage. The profile loss increases in proportion to the relative thickness of the blade. It is also inversely proportional to the Reynold's number when it is below 1000 00, because then the proportion of laminar flow surfaces and the losses resulting from them begin to increase rapidly. One of the goals of aerodynamic design is to keep the flow completely turbulent. The Reynold's number for compressors and turbines indicates the relative size of the blade. Re_c is calculated by multiplying the width of the blade by the flow velocity in the direction of the gas axis and dividing them by the dynamic viscosity (viscosity/density).

In addition to tip gap leakage, compressor end wall losses are caused by a slower flow region on the inner and outer end walls, which narrows the free flow region from both sides. End wall losses independent of tip gap leakage increase linearly with blade width, as shown in the next figure on the right.
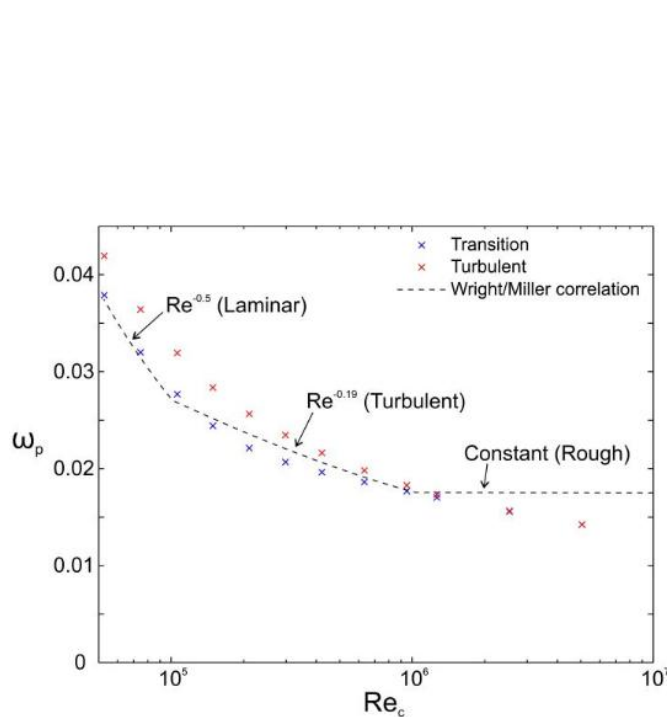
Fig. 18: Profile loss variation with Re_c (MISES)
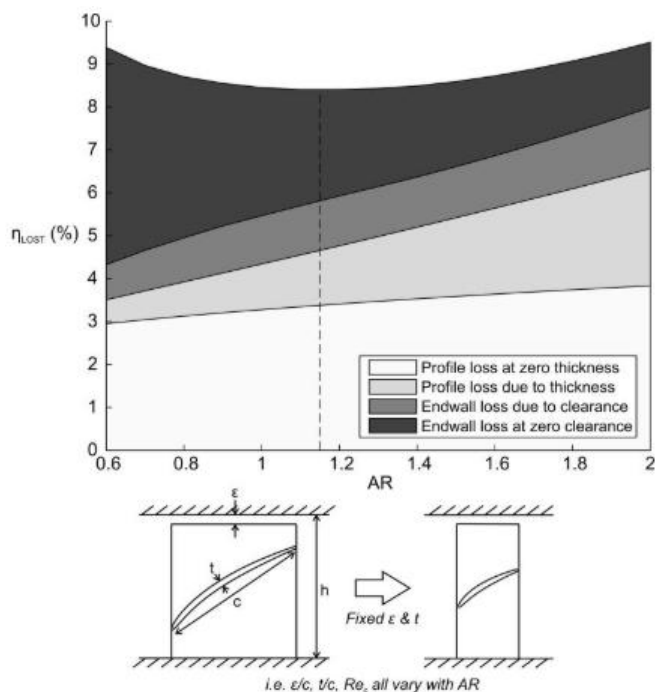
Fig. 21: Breakdown of lost efficiency using low order model $(t/h = 4.7\%, \varepsilon/h = 1.2\%, Re_h = 5.5 \times 10^5)$

The figure above shows the relationship between profile losses and Reynold's number according to the study THE EFFECT OF ASPECT RATIO ON COMPRESSOR PERFORMANCE [66]. On the right is another figure copied from the same study, shows the dependence of the blade aspect ratio (blade height/chord length c) on profile and end wall losses. The figure shows the contribution of 1.2% of the tip gap and 4.7% of the blade thickness to the total losses at different aspect ratios, when Re_h is constant $5.5 \cdot 10^5$. The Reynold's number Re_h in the figure has been calculated according to the rotor blade height, so that in the CFD simulation it would be constant as the

[66]https://api.repository.cam.ac.uk/server/api/core/bitstreams/fbfb70fe-58b3-47fb-a338-859384279d7c/content

aspect ratio and blade width change. In the figure, the profile losses increase, and the end wall losses decrease as you go to the right. At the same time, the Reynold's number of chord length Re_c decreases from $9.2 \cdot 10^5$ to $2.25 \cdot 10^5$. In the figure, the optimum blade aspect ratio AR 1.15 is found in the middle, where Re_c is $4.3 \cdot 10^5$, meaning that the laminar flow surfaces have started to increase profile losses.

Reynolds number also affects also endwall loss and blockage: *In compressor cascades, Reynolds number affects characteristics of loss, deviation angle and loading distributions by changing transition and separation behaviors of boundary layer along blade surfaces. In compressor stages, Reynolds number shows more complicated influences on performances besides airfoils, involving endwall effects, inter-stage matching and three-dimensional flow details. As a result, the Reynolds number effects varied among compressors stages, and were mainly discussed in the correction models of overall performances.*[67]

Reynold number correction factor of the profile loss depends also on the relative sand grain roughness Ks/c of the blade surface, where Ks is the sand grain roughness and c is the camber length. The next figure shows the dependence. The Ks value of a new smooth high-quality blade is below 2 μm, but a damaged blade may have 150 μm or more (see google search "what is sand grain roughness of compressor blade"). Thus, the blades in the high-pressure heat pump and cryogenic turbomachines, having chord lengths 26 – 50 mm and Re_c above $5 \cdot 10^6$, should have a Ks value about 0.5 μm.

---

[67] Correction models of Reynolds number effects for through-flow method in axial compressors
https://www.sciencedirect.com/science/article/pii/S1000936125003413#:~:text=Abstract,CFD%20calculations%20and%20Wassell's%20model.
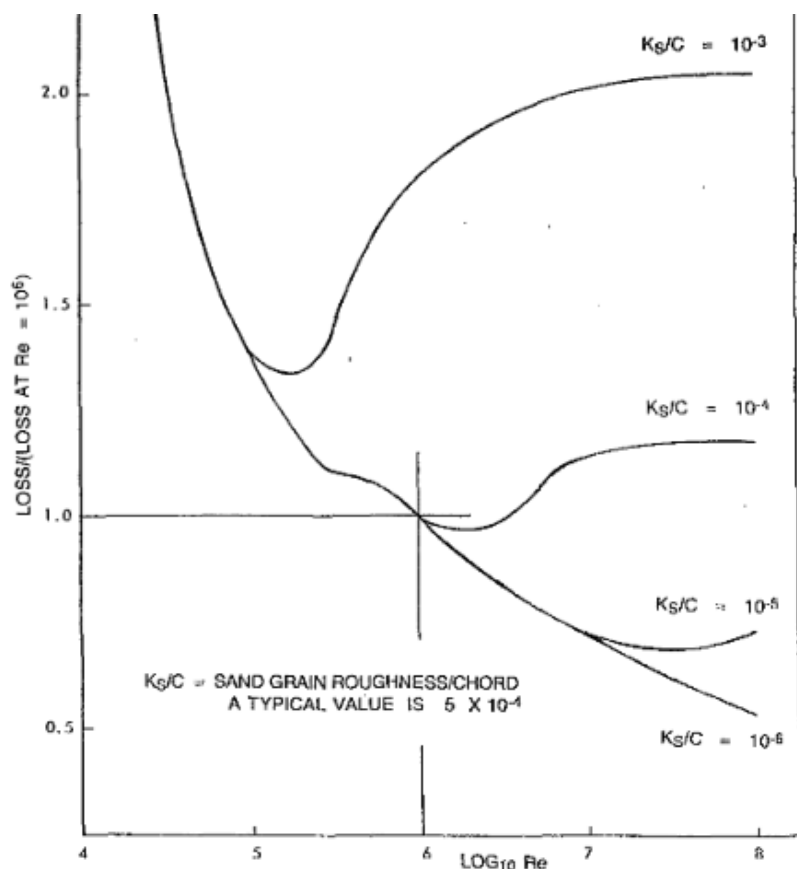
Fig. 23 Variation of profile loss with Reynolds number and surface roughness

Figure 8 The dependence of Re correction factor from blade surface roughness Ks (Loss Mechanisms in Turbomachines[68]). $K_S/C=10^{-5}$ is the expected roughness/chord of the high-pressure blades in this work.

The next diagram shows the Reynold's number corrections of compressor profile and endwall loss and turbine profile loss in this work. The third correction was used in Axial Flow Compressor Mean Line Design (by Niclas Falck), which was probably from the original work of Koch and Smith.

---

[68] https://www.unife.it/ing/lm.meccanica/insegnamenti/fluidodinamica-delle-macchine/materiale-didattico/JT_V115_621-656.pdf
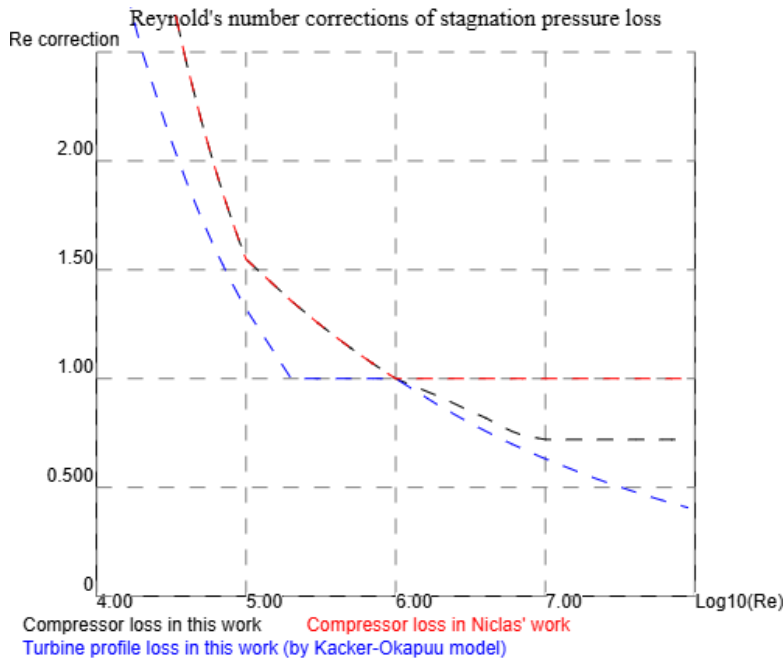
Figure 9 Reynold's number corrections of this work
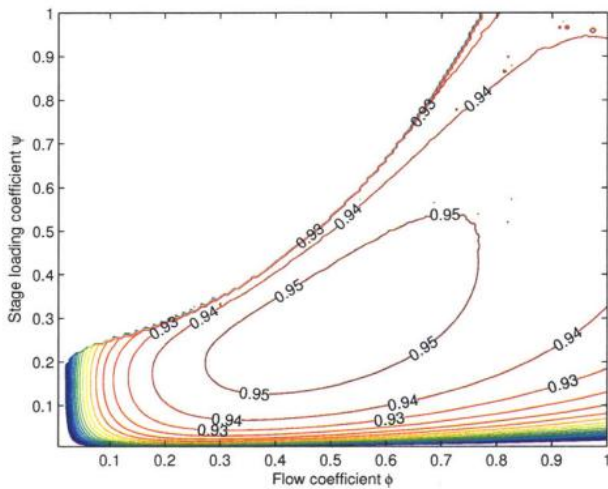
Figure 4-2: Smith chart, optimized baseline compressor stage   Figure 5-2: Smith chart, optimized baseline uncooled stage
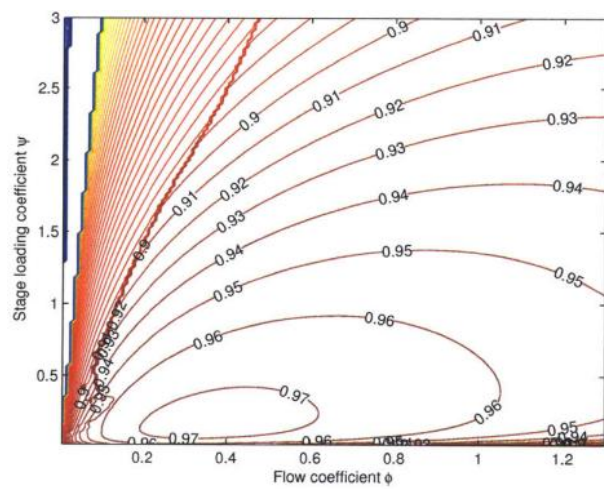
When the other loss factors in a compressor or turbine have been optimized to a minimum, the efficiency of a stage can be calculated from its stage loading and flow coefficents. Stage loading coefficient is calculated by the formula $\psi = \Delta h/U^2$, where Δh is the change in gas enthalpy J/kg and U is the rotation speed of the rotor tip m/s. The flow coefficient is $\phi = V_x/U$, where V_x is the axial velocity of the gas.

In the figure above, on the left is the Smith chart of an optimized upstream compressor stage and on the right is the chart of an optimized uncooled downstream turbine stage from the study Performance Limits of Axial Turbomachine. The Smith chart shows dependence of the stage efficiency on the flow coefficient and stage loading coefficient. The best efficiency is achieved by us a higher number of lowly loaded stages. The efficiencies in the figure have been calculated assuming that the tip gap is 1% of the blade length. Other parameters can be found in the mentioned study.

Compressor loss model used by the design and simulation program

The axial compressor loss models have been developed by several researchers since 1950s. It calculates the relative flow angles and velocities on the leading and tailing edge of the blade, and the maximum relative velocity of the fluid flow on the low-pressure side. From these, the diffusion factor DF and the equivalent diffusion ratio DR are calculated, from which the end wall and profile losses of the stage are calculated. The main source of the model is Axial Flow Compressor Mean Line Design (by Niclas Falck) available as an e-book and from Turbomachinery Lecture Series (RDDM) power point presentation[69]. Seymor Lieblein developed approximation for diffusion factor DF and equivalent diffusion ratio DR. Later Koch and Smith modified the Lieblein approach and developed a more advanced correlation for the losses which allows for the factors maximum thickness to chord (t/c) and the Axial Velocity Density Ratio, i.e. AVDR.[70]

Lieblein, Koch and Smith's loss model was calibrated by several cascade tests, and it matches quite well with the design points of subsonic compressors, but it may give less reliable results in the off-design conditions or for loaded intersonic compressors. The error margin with the subsonic cascade tests can probably be explained by the selected Reynolds number correction factor and blockage factor, that rarely match exactly with the actual values of a specific cascade.

The loss of an axial compressor is the function of load coefficient, flow coefficient, blade chord length c, blade spacing s, blade height h, max thickness t, tip clearance gap ε, axial velocity of the fluid Vx, the Mach number of the velocity, inlet and outlet density of the fluid (d1,d2), radius of inlet and outlet (r1, r2), Reynolds number Re_c, the blockage factor, the reaction of the stage and the type of the blade. The used loss algorithm ignores the possible shock loss (up to 30 %) caused when the flow velocity exceeds the speed of sound. The loss of the fluid accelerating to compressor inlet and deacceleration after outlet is an input parameter (the default loss is 3%).

---

[69] https://moodle.polymtl.ca/pluginfile.php/1035680/mod_resource/content/1/MEC8250-2020-Kidikian-Part-01-02.pdf
[70] Loss sources and magnitudes in axial-flow compressors CC Koch, LH Smith Jr - 1976
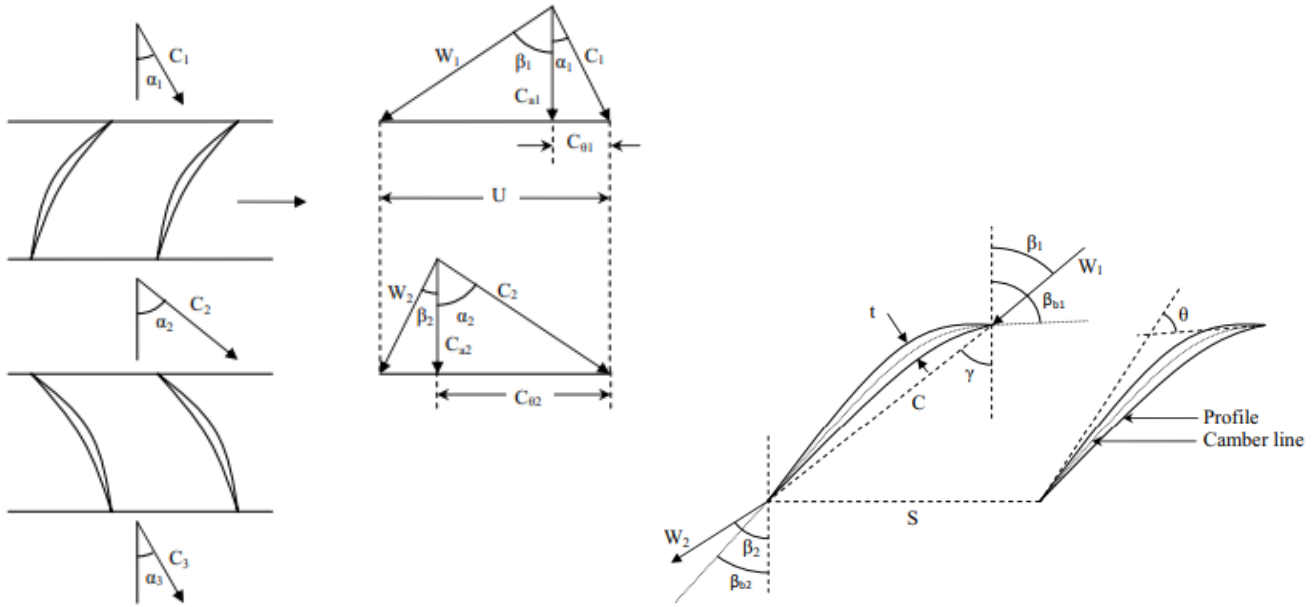
Figure 10. Symmetric velocity triangle of rotor and stator blades with reaction 0.5 on left, and incidence angle i (β_1 - β_{b1}), deviation angle δ (β_2- β_{b2}), and the camber angle Θ (β_{b1} - β_{b2}) on right. Source: Axial Flow Compressor Mean Line Design by Niclas Falck. The right-side figure is incorrect. Its relative velocity and incidence angles have very off-design values. A NACA65 reference incidence angle may be between -8° and 6° and its most typical value is near to 0°.

On the left C_1, C_2, C_3 are absolute fluid velocities, W_1 and W_2 are fluid velocities relative to the rotating rotor blade, U is the rotational speed. On the right are incidence angle *i* (β_1 - β_{b1}), the deviation angle δ (β_2- β_{b2}), and camber angle θ (β_{b1} - β_{b2}). Relative rotor inlet and outlet velocity angles β_1, β_2, and absolute velocity angles α_1, α_2, and α_3 are calculated from the median stage loading and flow coefficients. All values are in the mean flow with radius rMid = sqrt((rTip^2+rHub^2)/2) . The reaction is the pressure rise of the rotor divided by the pressure rise of the stage. 0.5 is usually very near to the optimal reaction for conventional axial compressors.

β_1 = atan([reaction + loadCoefficient/2]/flowCoefficient)   // inlet flow angle relative to rotor

β_2 = atan([reaction - loadCoefficient/2]/flowCoefficient)   // outlet flow angle relative to rotor

α_2 = atan([(1-reaction) + loadCoefficient/2]/flowCoefficient)   // absolute/relative flow angle at stator inlet

α_3 = atan([(1-reaction) - loadCoefficient/2]/flowCoefficient)   // absolute/relative flow angle at stator outlet

If we assume, that the axial velocity V_x is constant ($c_a == c_{a1} == c_{a2}$) for all stages and reaction is 0.5, then α_1 == α_3, and the velocities are V_x/cos(angle of velocity). Parameters ($\alpha1$, $\alpha2$) equal to (β_1, β_2) for rotor and (α_2, α_3) for stator. The profile and endwall lossed are calculated for both and then added: stage loss = reaction · rotorLoss + (1 – reaction) · statorLoss.

The flows of rotor and stator cascades are matched together by having the same loading and flow coefficient in the both sides of the gaps between cascades. This means, that blade inlet and exit have different loading and flow coefficients and their values change in the same way between inlet and exit as from hub to tip. The mean line stage loading and flow coefficients are the same only if the stage power and mean line radius are constants for all cascades.

The source code of axial compressor mean line stagnation pressure loss model by Lieblein, Koch and Smith is presented below. All angles are in degrees[71]. Because our program uses isentropic effciency, the resulted stagnation pressure loss coefficient is transformed to static enthalpy loss.

Ksh is the blade correction factor, it is 1 for NACA65 series and 0.7 for DCA blades. This algorithm is in the function getCamberAngle.

```
// for rotor and stator
Kit = -0.0214 + 19.17·(t/c) - 122.3· (t/c)² + 312.5· (t/c)³
i010 = 0.0325-0.0674·c/s + (-0.002364+0.0913·c/s) · α1 + (1.64/100000-2.38/10000·c/s) · α1²
// There seems to be different formulas for coefficient n, because the exact value of reference incidence angle is a design choice
// Nicla's version produces too low iRef values  ~ -4°
// n = -0.063+0.02274·c/s + (-0.0035+0.0029·c/s) · α1 - (3.79/100000+1.11/100000·c/s) · α1²
// This version was copied from an old Polytechnique Montréal material. It produces a too high iRef ~ +4°
//n = 0.063-0.02274 · c/s + (-0.0035+0.0029 · c/s) · α1 + (3.79/100000 + 1.11/100000 · c/s) · α1²
// My modified version produces expected iRef values ~0°
// and the results match with figures of https://ntrs.nasa.gov/api/citations/19710024786/downloads/19710024786.pdf
n = 0.063-0.02274 · c/s + (-0.0035+0.0029 · c/s) · α1 - (3.79/100000 + 1.11/100000 · c/s) · α1²
Kδ = 0.0142 + 6.172·(t/c) + 36.61· (t/c)²
δ010 = -0.0443+0.1057·c/s + (0.0209-0.0186·c/s) · α1 + (-0.0004+0.00076·c/s) ·α1²
b = 0.9655+2.538/1000·α1+4.221/100000·α1²-1.3/1000000·α1³
m = 0.17 - 3.33/10000·(1.0-0.1·α1) ·α1 · (s/c) ᵇ            // For NACA 65 series:
m = 0.249 + 7.4/10000·α1 - 1.32/100000·α1² + 3.16/10000000·α1³ · (s/c) ᵇ   // For DCA:
iRef = δRef = 0
10 loops {
        camberAngle = α1-iRef - (α2-δRef)              // θ = β1´ - β2´
        iRef = Ksh·Kit·i010 + n·camberAngle            // incidence angle iRef = β1 - β1´
        δRef = Ksh·Kδ·δ010 + m·camberAngle             // deviation angle δRef = β2 - β2´
}
α1θ = α1 – iRef            // suction side flow angle on leading edge
α2θ = α2 – δRef            // suction side flow angle on tailing edge
staggerAngle = α1 - camberAngle/2    // approximation copied from Niclas' Master thesis
Vx1 = Vx2 = Vx                       // axial velocity is kept constant
vssLE = Vx1/cos(α1θ)                 // suction side velocity on leading edge
vssTE = Vx2/cos(α2θ)                 // suction side velocity on tailing edge
vFlowIn = Vx1/cos(α1)                // relative velocity at blade inlet
vFlowOut = Vx2/cos(α2)               // relative velocity at blade exit
vSSmax ~= vFlowIn + (vssLE - vssTE)/(2·c/s)        // approximation maximum suction side velocity
//oldDF = (vSSmax - vFlowOut)/ vFlowIn             // Seymor Lieblein's approximation of diffusion factor (not used)

C_theta_in = Vx1·Math.tan(α1)               // angular velocity of blade inlet
C_theta_out = Vx2·Math.tan(α2)       // angular velocity of blade outlet
gamma = (r1· C_theta_in - r2· C_theta_out) / (vFlowIn· c/s ·(r1+r2)/2)
deHallerNum = vFlowOut/ vFlowIn
DF_lbl = 1 – deHallerNum + |gamma/2|         // used because produces 0.04-0.09 higher DF values and loss


// Equivalent diffusion ratio by Koch and Smith:
Γ = (r1· C_theta_in - r2· C_theta_out) / (vFlowIn·c/s ·(r1+r2)/2)
AVDR = d2·Vx2/(d1·Vx1)
ApStar = (1 - 0.4458 · c/s · t/c / cos(α1+α2)/2) · (2 + 1/AVDR)/3
densityRatio = 1 (Vx1/vMach)² / (1 - Vx1/vMach)² · (1 - ApStar - 0.244 · c/s · Γ · sin(α1))

eqDR = (vFlowIn/vFlowOut·(1 + 0.7688 · t/c) + 0.6024 · Γ) ·
```

[71] Loss sources and magnitudes in axial-flow compressors CC Koch, LH Smith Jr - 1976

$$\text{sqrt}([\sin(\alpha1) - 0.2445 \cdot c/s \cdot \Gamma]^2 + \cos(\alpha1) / [\text{ApStar} \cdot \text{densityRatio}])$$

profileLossParam = func(eqDR, vFlowIn/vMach)   // see the next figure

endWallLossParam = func(DF_lbl, tipGap/c)   // see the next figure

// Niclas forgot to multiply profileLossParam with solidity! Solidity increases the wetted perimeter of the blade row and loss.

$\text{profileLoss}_x = \text{scaleToRe(Re)} \cdot 2 \cdot \text{solidity} \cdot \text{profileLossParam} \cdot \text{deHallerNum}^2 / \cos(\alpha2) / \text{blockageFactor}_n$

$\text{endWallLoss}_x = \text{end'WallLossParam} \cdot \text{deHallerNum}^2 \cdot c / h / \text{blockageFactor}_n$

// The blockage factor used in this study is calculated from endWallEnthalpyLoss of the previous cascade

// $\omega_{ew} \cdot \text{AR}_{eff} \cdot k = \delta / c$ and $\text{AR}_{eff} = (h - \delta) / c$ => relative blockage $\delta/h = 1 / (1 / (k \cdot \omega_{ew}) + 1)$ =>

$k = f (\Delta p /(\rho_1 \cdot V_x^2))$ // blockage factor k is function of static pressure rise coefficient of axial velocity

$\text{blockageFactor}_{n+1} = 1 - 1 / (1 / (k \cdot \text{endWallLoss}_n) + 1)$ // blockage factor of the next stage

$Y = \text{profileLoss}_x + \text{endWallLoss}_x$ // stagnation pressure loss coefficient

// Transform stagnation pressure loss coefficient Y to enthalpy loss (i.e. work lost as heat)

// According to Denton, the stagnation entropy change:

// https://www.unife.it/ing/lm.meccanica/insegnamenti/fluidodinamica-delle-macchine/materiale-didattico/JT_V115_621-656.pdf

// Chapter: 2.3 Relation of Entropy Change to Machine Efficiency.

// Compressor stagnation pressure coefficient

// Y = (P01 -P02) / (P01 – P1), where $P0_x$ = PropsSI('P', 'S', S_x , 'H', H_x + 0.5*$V_{x\_rel}^2$, fluid)

// => P02 = P01 - Y · (P01 – P1) => s02-s01 = R · ln(P02/P01) = R · ln(1 – Y · (P01 – P1)/P01)

P02 = P01 – Y*(P01 – P1)

s2 = PropsSI('S', 'P', P02, 'H', h2 + 0.5*V_{2rel}, fluid)

P2 =PropsSI('P', 'S', s2, 'H', h2, fluid)

h2_100 = PropsSI('H', 'S', s1, 'P', P2, fluid)

η_x = 1 – (h2 – h2_100)/(h2 – h1)

stageEfficiency = $\eta_r \cdot r + \eta_s \cdot (1 - r)$ // add rotor and stator efficiencies
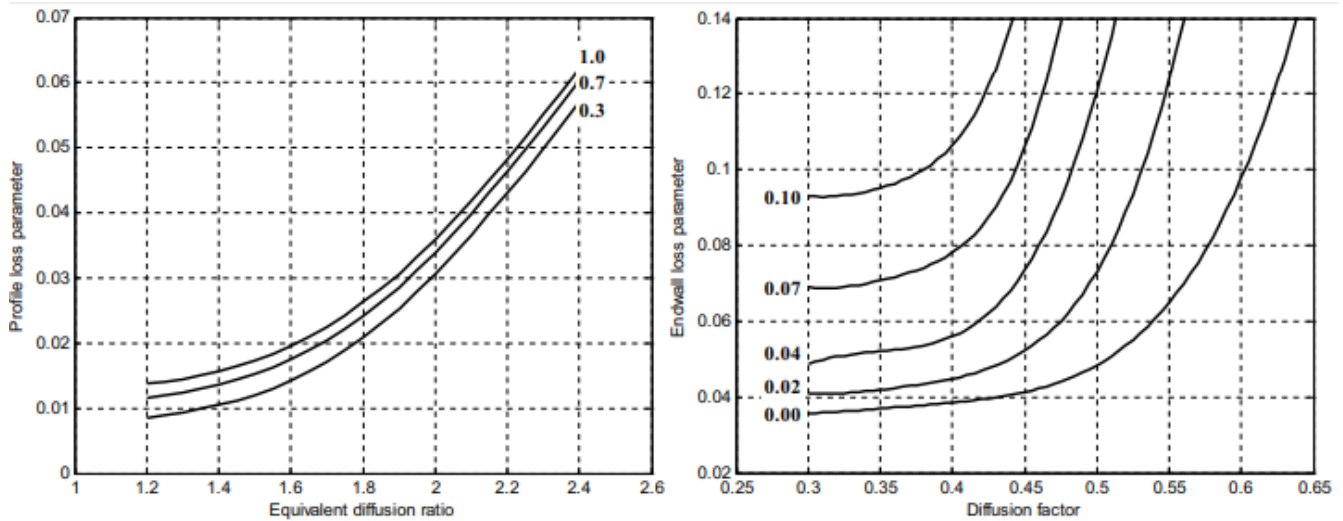
Figure 11. Profile loss parameter with variation of Mach number and eq. DR, and end-wall loss parameter with variation tip gap/c and DF
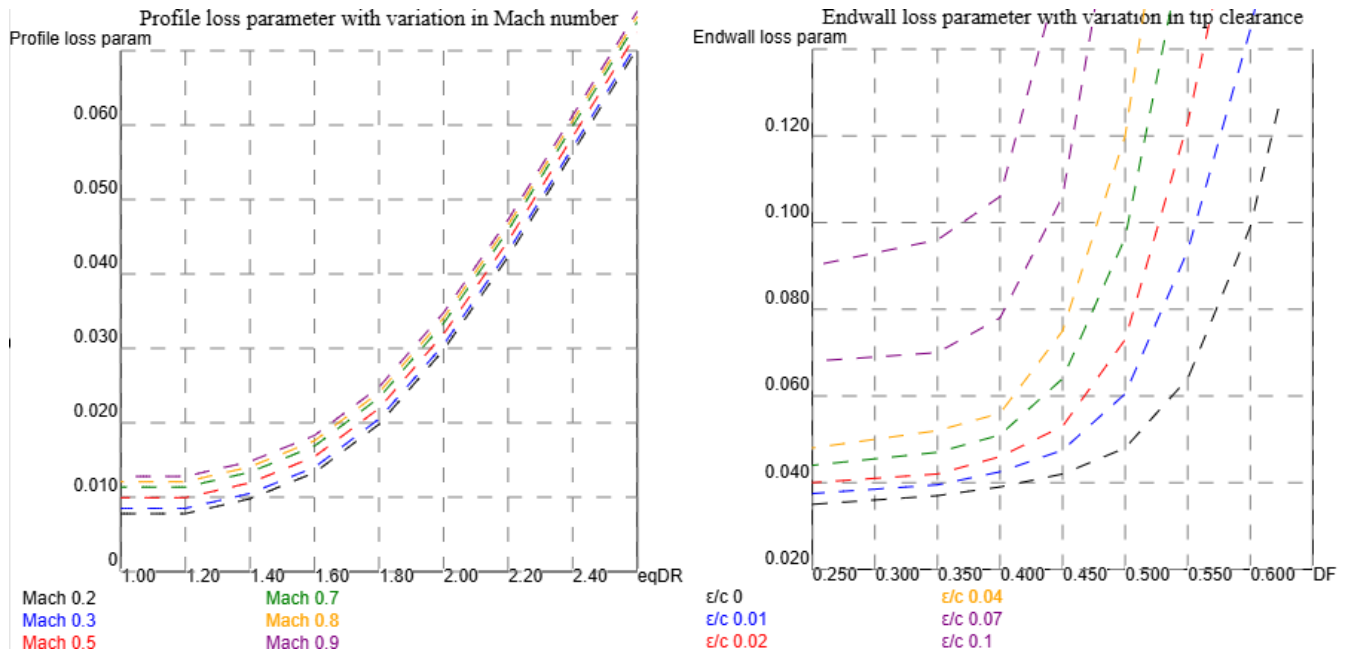
Figure 12. Linear extrapolation of profile and endwall loss parameter functions in this work. Design eqDR =~1.8 and DF=0.45

The algorithm implementing this loss model can also be found in the source code of the program's HTML page with names getLossParameters and *getEfficiencyWithDF_DR*. The algorithm uses the formula of NACA 65 series blades, when the relative gas velocity at the blade tip is below 0.7 Mach, and above it uses the formula of DCA (Double Circular Arcs) blades. The blade solidity, stage loading coefficient, flow coefficient, blade angles and relative thickness have been calculated at the mean radius of the blade, i.e. there are equal section areas both sides of the mean line. The average losses of the stage are assumed to be the same as the losses of the mean line. The compressor loss model did not include Reynold number correction or did not mention the reference value of the model. We chose $Re_c=10^6$ as the reference value, because then the model matches best with the other loss model, and it is also a logical choice as the reference value of Reynold's number, because then the flow becomes fully turbulent.

The compressor mean-line loss model returns the stagnation pressure loss coefficient for a stationary blade row:

Y = (P01 - P02) / (P01 – P1) => P02 = P01 – Y*(P01 – P1)

P1 is the static pressure in blade row inlet and P01 and P02 are relative stagnation pressures in inlet and exit. The relative stagnation pressure is calculated with the thermodynamic library from entropy, relative velocities and static values of enthalpy and pressure: P01 = PropsSI('P', 'S', s1, 'H', h1 + 0.5*V_{1rel}, fluid), where s1 is the entropy (J/kg/K), h1 is the static enthalpy (J/kg) and V_{1rel} is the relative velocity in blade inlet.

When also Y, h2 and V_{2rel} are known, the machine efficiency and exit values of a compressor blade row are:

P02 = P01 – Y*(P01 – P1)
s2 = PropsSI('S', 'P', P02, 'H', h2 + 0.5*V_{2rel}, fluid)
P2 =PropsSI('P', 'S', s2, 'H', h2, fluid)
h2_100 = PropsSI('H', 'S', s1, 'P', P2, fluid)
η = 1 – (h2 – h2_100)/(h2 – h1)

A stationary blade row must have the same axial velocity, stage loading coefficient and flow coefficient in its inlet and exit. If this is not the case, then the machine loss can be calculated either with the inlet or exit values and use the resulted loss to get the actual P2, s2 and h2 values. Otherwise, the calculated loss would be totally wrong, and it could be negative.

Denton suggested the following approximation for the compressor machine efficiency for a blade row:
$\Delta s = -R*\ln(P02/P01) = -R*\ln(1 - Y*(P01 - P1)/ P01)$
$\eta = 1 - T2*\Delta s/(h2 - h1)$

The error of this approximation seems to be 0 – 4 %. The approximation is used to calculate the compressor loss values on Smith's chart.

Simple compressor blockage model based on endwall loss and pressure rise coefficient of axial velocity

The loss caused by compressor endwall blockage is included in this compressor mean line loss model implementation. In the literature end wall blockage is usually defined by work done factor, the proportion of the cross-sectional area doing actual work i.e. compressing the gas, that decreases by decreasing steps down to a constant value in the rear high-pressure stages. The cross-sectional area of each stage and its calculated stagnation pressure loss coefficient must be divided by the blockage factor of the stage. The maximum blockage factor is usually an input parameter, e.g. 0.86, but in this study, we calculate it from the endwall loss ω_{ew} and the stage static pressure rise coefficient of axial velocity V_x.
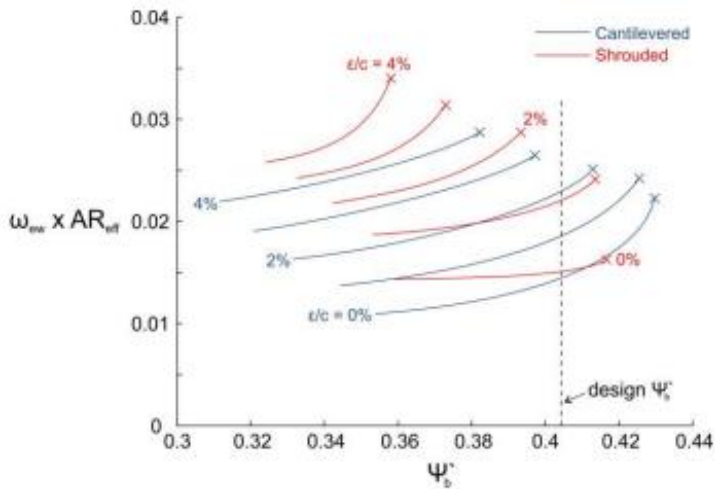
Fig. 15: Comparison of endwall loss coefficient for cantilevered & shrouded endwalls
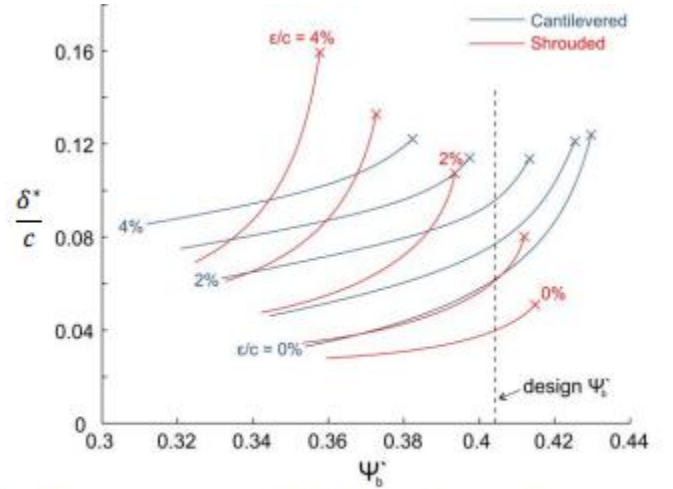
Fig. 16: Comparison of blockage for cantilevered & shrouded endwalls

The relation of blockage δ to the endwall loss coefficient ω_{ew} and static pressure rise coefficient $\Psi^{\cdot}_{bU}$ = $2 \cdot \Delta p/\rho U^2$ is shown in the previous figures copied from THE EFFECT OF ASPECT RATIO ON COMPRESSOR

PERFORMANCE. We can define the dependency of two graphs as $\omega_{ew} \cdot AR_{eff} \cdot k = \delta / c$. In the figure factor k is a function of the static pressure rise coefficient $\Psi^{\cdot}_{bU}$ only because the used flow coefficient V_x/U is constant 0.6.

It has been found in CFD-simulations of multistage compressor, that the blockage is insensitive to the radial blade velocity U[72], but it is a function of stage static pressure rise coefficient of axial velocity: $\Psi^{\cdot}_{bVx}= \Delta p/\rho V_x^2$. It means, that the blockage decreases from left to right on Smith's chart when radial velocity U and the stage loading coefficient $\Delta h/U^2$ are constant, but increased loading Δh or decreased radial velocity U does not increase the blockage, if the axial velocity is unchanged.

J.H. Horlock's theoretical blockage model[73] for a fully turbulent flow agrees with that finding: $\Delta\delta =$ $K\cdot H\cdot\Psi^{\cdot}_{bU}\cdot\tau/(2\cdot\Phi^2)$ [74], where H is the shape factor of boundary layer, K the coefficient of Horlock's blockage model, τ dimensionless tip clearance, Φ stage flow coefficient V_x/U and V_x axial velocity. Radial velocity U can be sieved away from the Horlock's formula: $K\cdot H\cdot\Psi^{\cdot}_{bU}\cdot\tau/(2\cdot\Phi^2) == K\cdot H\cdot\tau \cdot\Delta p /(\rho\cdot V_x^2)$. In the next picture $\Psi^{\cdot}_{bU}$ at design point is only half of its value 0.81 mentioned in the study, because it has been calculated for a blade row. The $\Psi^{\cdot}_{bU}$ values can be divided by $(\Phi = 0.6)^2$. When the effective aspect ratio AR_{eff} is $(h - \delta^*)$ /c and AR_{eff} ω_{ew} equals $k \cdot \delta^*/c$, we get blockage to blade height $\delta^*/h = 1 / (1 / (k \cdot \omega_{ew}) + 1)$, where factor k is a function of axial static pressure rise $\Psi^{\cdot}_{bVx} = \Delta p /(\rho\cdot V_x^2)$. In the picture factor k is about 2.8, 4.3 and 5.0 for $\Psi^{\cdot}_{bU}$ values 0.355, 0.405 and 0.43, when the stage loading and flow coefficients are constant (0.44 and 0.60).   Respective $\Psi^{\cdot}_{bVx}$ values are 0.986, 1.125 and 1.194, which are used as reference points in the extrapolation of k.

The previously referred study *The effect of end wall boundary layer on matching and corresponding flow control technique for multistage axial compressor* by Li Zhihui, Zheng Xinqian, and Ji Baohua suggests the re-cambering of the rear stators in the hub region can decrease the blockage. This probably means, that the blockage could be compensated by increased flow coefficient and reaction in the displacement area near the hub. Increased reaction near the hub also decreases the profile loss and the centrifugal stress.

The blockage depends also on Reynold's number, but we don't make an extra correction because the compressor endwall loss has already been Reynold's number corrected.

Compressor blockage increases both the cross area of the stage and the loss, and the increased endwall loss increases again the blockage until the blockage stabilizes before 10th stage. For simplicity we ignore this gradual increase, but we set the blockage of the next stage immediately to the level it would reach after repeating several identical stages. On the other hand, the blockage is also decreased immediately, if the endwall blockage and factor k produce a smaller blockage.

---

[72] https://journals.sagepub.com/doi/10.1177/0954410015621928

[73] The determination of end-wall blockage in axial compressors: A comparison between various approaches

[74] https://www.sciencedirect.com/science/article/pii/S1000936125003413
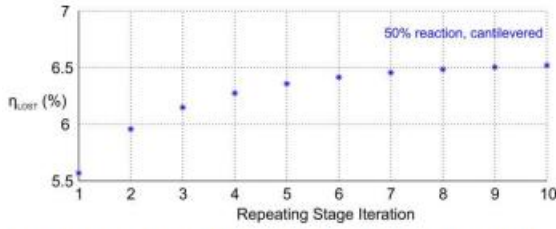
Fig. 2: Lost efficiency vs no. of repeating stage iterations ($AR = 1.7$, $\varepsilon/c = 1.0\%$, $t/c = 4.1\%$, $Re_c = 6.3 \times 10^5$)
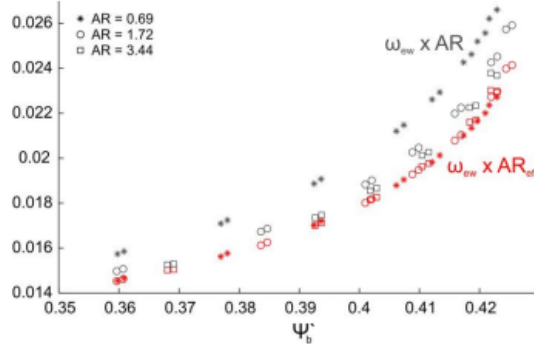
Fig. 10: Endwall loss varies inversely with effective AR and not AR ($\varepsilon/c = 1.0\%$)

Figure 2 shows the increase of the lost efficiency caused by blockade when the endwall loss is increased only by the blockage itself. The stage outlet blockage increases the loss of the next stage, and its endwall loss increases the blockage until the increase becomes too small to measure at stage 10. The loss of stage 10 is the loss of stage 1 divided by 0.85, which is almost the same as work done factor 0.86. The endwall loss is about 40 % of the total loss in the figure 2.

Compressor stall/surge prediction model

Reliable stall prediction model is very useful in the initial compressor design phase. The best compressor efficiency is usually near the stall/surge limit, but it also sets the maximum pressure ratio for the compressor. The stall occurs usually near the hub of the first low pressure compressor stage, but if the compressor has the constant inner radius, the stall may occur in any upper stage. So, the stall margin is calculated for all stages. We selected the algorithm suggested in a recent study: *An improved stall prediction model for axial compressor stage based on diffuser analogy, 2022*[75] by Li, Jian; Teng, Jinfang; Ferlauto, Michele; Zhu, Mingmin and Qiang, Xiaoqing.

The writers claim, that model predictions are within 15 % of the actual tested stall values, which means that the compressor designs with an estimated stall margin 85 % or less will very likely be able to produce the planned pressure ratio in the design point.

Below is the JavaScript implementation of their algorithm of this work. The algorithm is in getLossParameters function.

```
// stall/surge limit by Koch et al:
const s = c/solidity;                    // spacing between blades = chord/solidity
const U2 = U·r2/r1;                      // angular velocity in blade outlet
const V2 = axV2/Math.cos(α2);            // absolute velocity in stator inlet
const Re1 = dynamicVisc1 · c · vRel1;
const Re2 = dynamicVisc2 · c · V2;
// actual static pressure rise coefficient
const Cp = (ΔhStage - 0.5·(U2·U2 - U·U)) / ((vRel1·vRel1 + V2·V2)/2);
const Vmin = (β2+α2) <= Math.PI/2 && β2 >= 0 ? V2·Math.sin(β2+α2) :
                            (β2+α2) > Math.PI/2 ? V2 : U2;
const Fef = (V2·V2 + 2.5·Vmin·Vmin + 0.5·U2·U2) / (4·V2·V2);
const ReStage = (Re1·vRel1·vRel1 + Re2·V2·V2) / (vRel1·vRel1 + V2·V2);
```

[75] https://iris.polito.it/retrieve/580ec40f-1a42-42d8-8f74-841adc5600cd/postprint.pdf

```javascript
const camberAngleRad = ret.camberAngle · Math.PI / 180;
const Rc = c / 2 / Math.sin(camberAngleRad/2);
const Xc = Rc · Math.cos(ret.midβ1θ) + s / 2;
const Yc = Rc · Math.sin(ret.midβ1θ);
const k1 = -Math.tan(β1);
const k2 = -Math.tan(β2);
const Xa = (Xc + k1·Yc - Math.sqrt(Math.abs(Rc·Rc·(k1·k1+1) - Math.pow(k1·Xc-Yc,2))))/(k1·k1+1);
const funcβ2 = k2·(Rc·Math.cos(β2)-s/2)+Rc·Math.sin(β2);
const Xb = Xc - (k2·funcβ2 + Math.sqrt(Rc·Rc·(k2·k2+1) - Math.pow(funcβ2,2)))/(k2·k2+1);
const Ya = k1·Xa;
const Yb = k2·(Xb-Xc+s/2-Rc·Math.cos(β2))+Yc+Rc·Math.sin(β2);
const κA = Math.atan((Ya-Yc)/(Xc-Xa));
const κB = Math.atan((Yb-Yc)/(Xc-Xb));
const κ2 = ret.midβ2θ; // κA-κB < 0 !!! when the loading is very low
const modLg2 = solidity·Math.abs(κA-κB)/2/(Math.sin(camberAngleRad/2)·Math.cos(κ2));
const BL = Math.pow(ReStage, 1/6) / solidity;
const modCh = getStallingPressureRiseCoefficientModCh(modLg2, getBlockagePercent(BL));
const refCamberAngleRad = (0.0165 · Math.pow(ret.staggerAngle,2) - 2.029 · ret.staggerAngle + 72.97)
                                          · Math.PI / 180;      // to radians
const Fcam = Math.pow(
        (camberAngleRad · Math.sin(refCamberAngleRad/2)·Math.cos(κ2-refCamberAngleRad/2+camberAngleRad/2))
        / (refCamberAngleRad·Math.sin(camberAngleRad/2)·Math.cos(κ2)), 2);
const ΔZ = c·stageData.rotorStatorGap;// 0.2 is typical space between compressor blade rows
const Z = Math.round(2·Math.PI·r1/s);              // number of blades on row
const g = Math.PI·(r1+r2)/2·(Math.cos(ret.midβ1θ)+Math.cos(ret.midβ2θ))/Z;
const Fεg = fTipClearanceAveragePitchlineGap( h·tipGap / g );
const FΔZs = fNormalizedAxialSpacing( ΔZ / s );
ret.CpMax = modCh·Fcam·Fεg·FΔZs·Fef; // return maximum allowed static pressure rise
ret.Cp = Cp;          // return actual static pressure rise
ret.stallMargin = ret.Cp/ret.CpMax;      // return the stall margin
return ret;

function fTipClearanceAveragePitchlineGap( εg ) {
        const a = [[0,1.215],[0.01,1.14],[0.02,1.085],[0.04,1.035],[0.1,0.92],[0.12,0.89],[0.13,0.88],[0.14,0.865],[0.15,0.84]];
        return getLinearInterOrExtrapolation( a, εg );
}
function fNormalizedAxialSpacing( deltaZ_s ) {
        const a = [[0,1.19],[0.1,1.06+0.02·3/12],[0.2,1.0305],[0.3,1.01],[0.4,0.995],[0.5,0.89],[0.6,0.88],[0.7,0.865],[0.8,0.865]];
        return getLinearInterOrExtrapolation( a, deltaZ_s );
}
// An improved stall prediction model for axial compressor stage based on diffuser analogy, 2022
// Figure 9: Effects of blockage indicator on static-pressure-rise coefficient
// BL >= 9 => Rec >= 531441
function getBlockagePercent(BL) {
        if (BL >= 9) return 1;
        else if (BL >= 8) return  1 + 1·(9-BL);
        else if (BL >= 7) return  2 + 3·(8-BL);
        else if (BL >= 5.5) return  5 + 4·(7-BL);
        else return  13 + 8/3·(4.75-BL);
}
// An improved stall prediction model for axial compressor stage based on diffuser analogy, 2022
// Figure 8: Correlations of static-pressure-rise coefficient at different blockage
function getStallingPressureRiseCoefficientModCh(modLg2, blockagePercent)
{
```

```javascript
        const blockagePercent1 = [[0.5·3/12, 0.2],[0.5, 1.3/17],[1, 0.5+0.25/17],[1.5, 0.6+0.2/17]];
        const blockagePercent9 = [[0.5·7/12, 0.2],[0.5, 0.2+1.3/17],[1, 0.4],[1.5, 0.4+1.2/17],
                                                    [2.0 ,0.5+0.45/17],[2.5, 0.5+1.2/17]];
        const blockagePercent13= [[0.5,0.2], [1.0, 0.3+0.7/17], [1.5, 0.4+0.35/17],
                                                    [2.0, 0.4+1.2/17], [2.5, 0.5+0.2/17]];
        if (blockagePercent <= 1) {
                return getLinearInterOrExtrapolation( blockagePercent1, modLg2 );
        }
        else if (blockagePercent <= 9) {
                const modCh1 =  getLinearInterOrExtrapolation( blockagePercent1, modLg2 );
                const modCh2 =  getLinearInterOrExtrapolation( blockagePercent9, modLg2 );
                return modCh1·(9 - blockagePercent)/8 + modCh2·(blockagePercent-1)/8;
        }
        else {
                const modCh1 =  getLinearInterOrExtrapolation( blockagePercent9, modLg2 );
                const modCh2 =  getLinearInterOrExtrapolation( blockagePercent13, modLg2 );
                return modCh1·(13 - blockagePercent)/4 + modCh2·(blockagePercent-9)/4;
        }
}
// Linear inter- and extrapolation
function getLinearInterOrExtrapolation( xyVals, xVal )
{
        var i;
        for (i = 0; i < xyVals.length; i++) {
                if (xVal <= xyVals[i+1][0] || (i+2) == xyVals.length) {
                        return xyVals[i][1] + (xyVals[i+1][1] - xyVals[i][1])
                                · (1 - (xyVals[i+1][0]-xVal)/(xyVals[i+1][0]-xyVals[i][0]));
                }
        }
}
```

Turbine mean line loss model

The mean line loss model[76] presented by Kacker and Okapuu in 1982 was selected for turbines. The source code was adapted from the work of Roberto Agromayor and Lars O. Nord *Preliminary Design and Optimization of Axial Turbines Accounting for Diffuser Performance*[77] that contains an excellent description of the turbine loss model with MathLab source code, and there is no reason to present it here again in detail. Kacker and Okapuu turbine loss model matches very well with the empirical on-design tests of turbines, but it is not very useful in the prediction of off-design conditions. The source code of the model is in file Kacker-Okapuu_loss_model.js, that is almost direct JavaScript transformation of Roberto's original MathLab source code. The algorithm is called from the stage design loop originally made for only compressors but later extended to for both turbomachines.

---

[76]Kacker, S.C.; Okapuu, U. A Mean Line Prediction Method for Axial Flow Turbine Efficiency. J. Eng. Power 1982
[77] https://www.mdpi.com/2504-186X/4/3/32

For a normal stage, $c_1 = c_3$

$$R = (h_2 - h_3)/(h_{01} - h_{03})$$

Using eq. 4.4: $h_2 - h_3 + (w_2^2 - w_3^2)/2 = 0$ and Euler

$$R = \frac{w_3^2 - w_2^2}{2U(c_{y2} + c_{y3})}$$

$$R = \frac{(w_3 - w_2)(w_3 + w_2)}{2U(c_{y2} + c_{y3})} = \frac{w_3 - w_2}{2U}$$
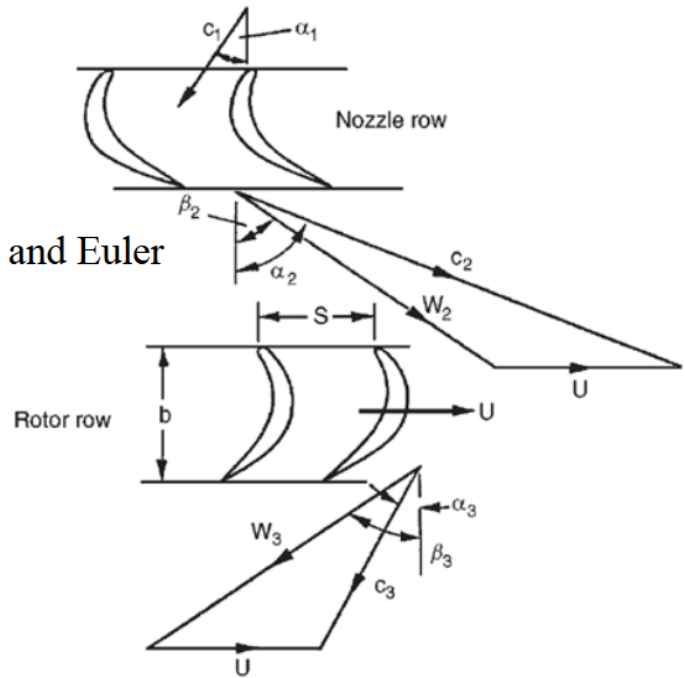
Figure 13. Turbine velocity triangle (source https://www.lth.se/fileadmin/tpe/Kurser/Chapter_4.pdf)

Turbine velocity triangle and its flow angles are different from compressor ones. These formulas were derived from Theory of turbo machinery presentation (LTH) [78].

α_1 = atan([loadCoefficient/2 - (1-reaction)]/flowCoefficient)   // absolute/relative flow angle at stator inlet

α_2 = atan([loadCoefficient/2 + (1-reaction)]/flowCoefficient)   // absolute/relative flow angle at stator outlet

β_2 = atan([loadCoefficient/2 - reaction]/flowCoefficient)   // inlet flow angle relative to rotor

β_3 = atan([loadCoefficient/2 + reaction]/flowCoefficient)   // outlet flow angle relative to rotor

Kacker-Okapuu loss model returns the turbine stagnation pressure rise loss coefficient Y = (P01 – P02) / (P02 – P2) for a stationary blade row, where P01 and P02 are stagnation pressures of blade inlet and exit. The stagnation pressure can be calculated with the thermodynamic library from the static values of entropy, enthalpy and relative velocity in blade inlet and exit:

P01 = Module.PropsSI('P', 'S', s_{in}, 'H', h_{in} + 0.5*V_{relIn} , fluidName)

P02 = Module.PropsSI('P', 'S', s_{out} , 'H', h_{out} + 0.5*V_{relOut} , fluidName).

The entropy at blade exit (s_{out}) can be calculated with only if we can guess the machine loss. It means, that there must be an iterative loop, that is repeated until the error (Y - (P01 – P02) / (P02 – P2))/Y is almost zero at least by three decimal digits. The calculations must be done assuming the blade row inlet and exit to have the same axial velocity, stage loading coefficient and flow coefficient and the resulted efficiency must used to calculate the actual P2, s2 and h2 values, when the blade row is not stationary.

[78] https://www.lth.se/fileadmin/tpe/Kurser/Chapter_4.pdf

Kacker-Okapuu loss model contains the Reynold's number correction, but no blockage correction was done for the turbine loss or stage cross area, because we found no references about turbine blockage in the literature.

Kacker-Okapuu loss model uses the blade thickness correlation of Ainley/Mathieson/Dunham/Came (AMDC) loss system: $Y_p = Y_p * (tMax / chord / 0.2)^a$ where exponent $a = \beta_1 / \alpha_2$ (metal flow angle in/relative flow angle out) which equals α_1/α_2 for circular blades with zero incidence angle used in the modern turbines. The result of this equation would be infinite with a negative α_1 / α_2 and zero thickness, and the profile loss of negative exponent would decrease when thickness increases. The source implementation used in this work resolved the problem with $a = max(0, \alpha_1/\alpha_2)$, which means, that the thickness correlation is always 1 for all thickness values when α_1 / α_2 is negative. In this work the exponent was changed to $a = \alpha_2 > 0$? $|\alpha_1/(\alpha_2 - min(0,\alpha_1))|$: $|\alpha_1/(\alpha_2 - max(0,\alpha_1))|$. The thickness correlation equations means, that the zero inlet angle has the same loss as the reference value of tMax/c regardless of the actual thickness, because the flow has the maximum thickness in the both side and the loss is caused only by the acceleration and diffusion. When inlet angle grows from zero to any direction, the opposite max thickness positions shift apart, the flow starts to turns around them and the loss correlates more and more with the relative maximum thickness. The divider is the actual turning angle of the blade when α_1/α_2 is negative.
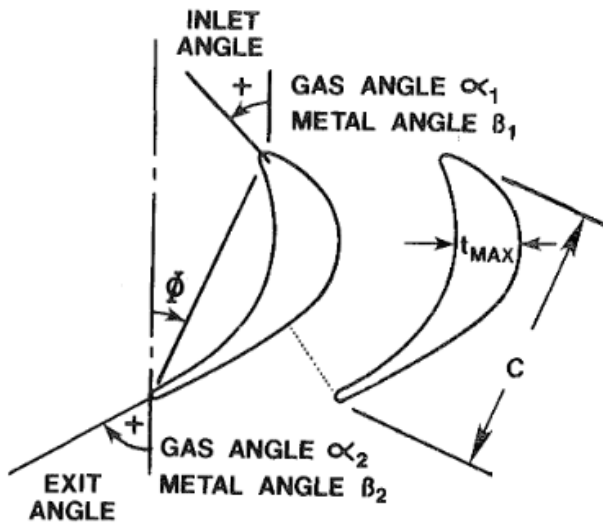
Fig. 3   Blade section terminology
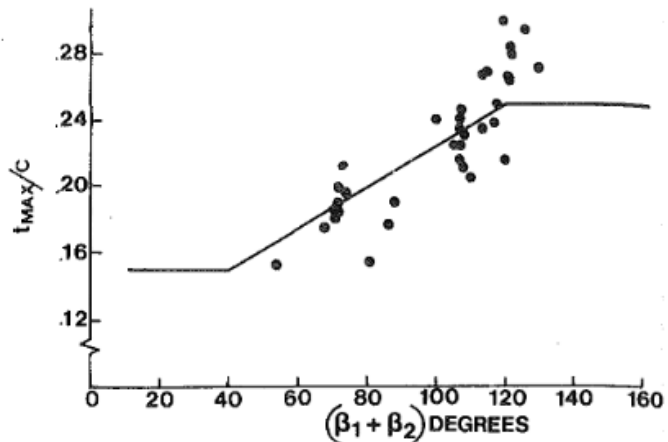
Fig. 4   Thickness/chord ratio for typical turbine blade sections

This work presents turbine designs with efficiency predictions 2-3 % above the reference measurements of the model in the next figure from Kacker's and Okapuu's work. Nevertheless, the model predicts quite well the efficiencies between 80 % and 94 % of the turbine designs from 70s, and it very likely still works also above that range. In this work the loss model predicts the best stage efficiencies are above 97% when stage loading coefficient $\Delta H/U^2$ is 0.7 and flow coefficient C_x/U is 0.45-0.50. The values match quite well with the extrapolation of the Smith's chart in the next figure. Most reference turbines had just one stage, but there is an interesting case of a turbine with 4 stages (30, 31, 32 and 33) where lower pressure ratios and high aspect ratios produce good efficiencies matching well with the predictions. In the same way the increased number of stages with very high aspect ratio, lower pressure ratio and loading explain the excellent turbine efficiency predictions of this work. The lower stage efficiencies of the 4 stages turbine (about 91%) are mainly explained by its quite high stage loading and flow coefficients (2.32-2.71 and 1.25-1.50 respectively).

NO.	SOURCE	# STAGES	STAGE	$\Delta H/U^2$	Cx/U	PRESS. RATIO	h/c NOZZLE	h/c ROTOR
1	P&WA	1	1	1.88	.54	2.67	.366	1.75
2	P&WA	1	1	1.51	.533	4.00	.612	1.98
3	P&WA	1	1	1.45	.565	3.89	.571	1.72
4	P&WA	1	1	1.55	.570	2.95	.437	2.188
5	OTHER	1	1	1.25	.613	2.98	.520	.671
6	OTHER	1	1	1.55	.675	2.90	.55	.825
7	OTHER	1	1	1.59	.642	2.90	.725	1.26
8	OTHER	1	1	1.11	.383	1.48	1.50	1.50
9	OTHER	1	1	1.656	.595	2.77	1.0	1.0
10	OTHER	2	1	.989	.309	1.11	1.44	1.456
			2	.987	.318	1.11	1.32	1.489
11	OTHER	1	1	1.672	.696	1.82	.71	1.01
12	P&WA	1	1	1.19	.397	2.00	.317	.739
13	P&WA	1	1	1.19	.531	2.00	.247	.777
14	P&WA	1	1	1.19	.497	2.00	.253	.670
15	P&WA	1	1	1.139	.322	3.40	.24	.486
16	OTHER	2	1	1.65	.690	1.71	1.47	1.87
			2	1.65	.813	1.87	1.54	2.16
17	OTHER	1	1	2.00	.721	1.99	.468	.847
18	P&WA	1	1	1.44	.566	2.76	.637	1.9
19	P&WA	2	1	1.50	.924	1.45	1.27	2.09
			2	1.77	.990	1.65	1.95	2.47
20	P&WA	2	1	.9	.622	1.44	1.102	2.23
			2	.83	.502	1.53	1.81	3.02
21	P&WA	2	2	1.28	.758	1.70	1.102	2.23
			1	1.02	.698	1.73	1.81	3.02
22	P&WA	1	1	1.94	.529	2.24	1.23	2.67
23	P&WA	1	1	2.388	.712	2.68	1.23	2.67
24	P&WA	1	1	1.45	.565	3.89	.571	1.08
25	P&WA	1	1	1.45	.561	3.89	.984	1.72
26	P&WA	1	1	1.516	.583	2.81	.421	1.95
27	P&WA	1	1	1.463	.492	3.23	.527	2.155
28	P&WA	1	1	1.38	.485	1.99	.710	.921
29	P&WA	1	1	1.58	.545	1.94	1.328	1.111
30	P&WA	4	1	2.44	1.50	1.33	2.61	3.94
31	"		2	2.32	1.28	1.35	4.07	4.98
32	"		3	2.38	1.25	1.45	5.01	5.76
33	"		4	2.71	1.50	1.68	5.68	5.80
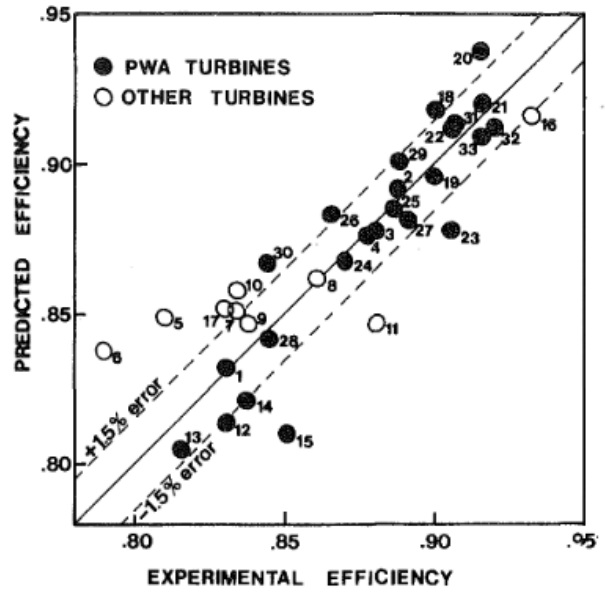
Fig. 19 Comparison of predicted efficiency with experimental efficiency of 33 turbines (new loss system)
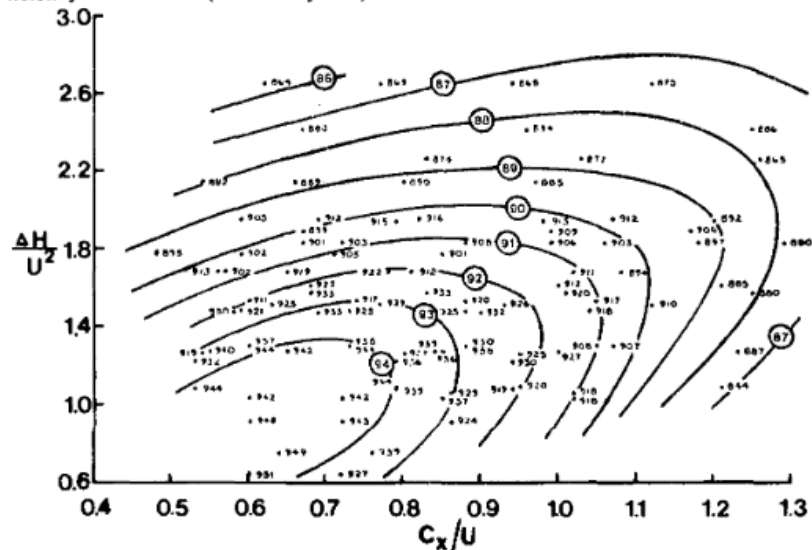
Fig. 16 Turbine stage efficiency at zero tip leakage calculated by the present method

Figure 14. The experimental efficiencies compared to the efficiencies predicted by Kacker-Okapuu.loss model.

Subsonic velocity and lower stage loading coefficient usually means increased number of stages. The next figure from work *Turbomachinery flowpath design and performance analysis for supercritical CO2*[79] shows the efficiency vs number of stages for a large supercritical CO_2 turbine with a constant pressure ratio 2.86 and variable rotational speeds. In our work the selected mass flow and fixed rotational frequency sets optimal number for the stages.

---

[79] https://www.softinway.com/wp-content/uploads/2024/09/GT2014-25385.pdf
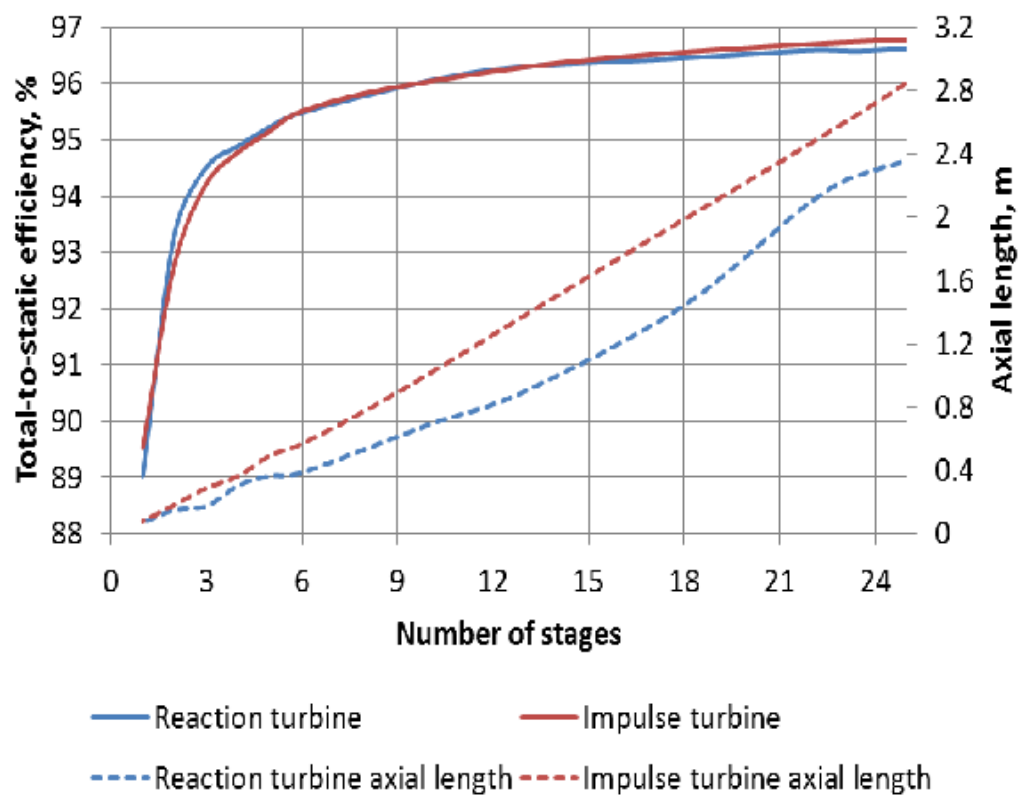
On-design states and power control of the plant

A multi-stage turbomachine cascade is stationary only when the axial velocity is constant in all stages. This will never happen in the real word, but turbomachine is operating in on-design state a high efficiency only when they are operated in an where the thermodynamic state of stage inlet matches with its design values.

with the At the center of the charge/discharge unit is a large motor-generator, which acts as a motor in the charging Source: https://ntrs.nasa.gov/api/citations/19710024786/downloads/19710024786.pdf
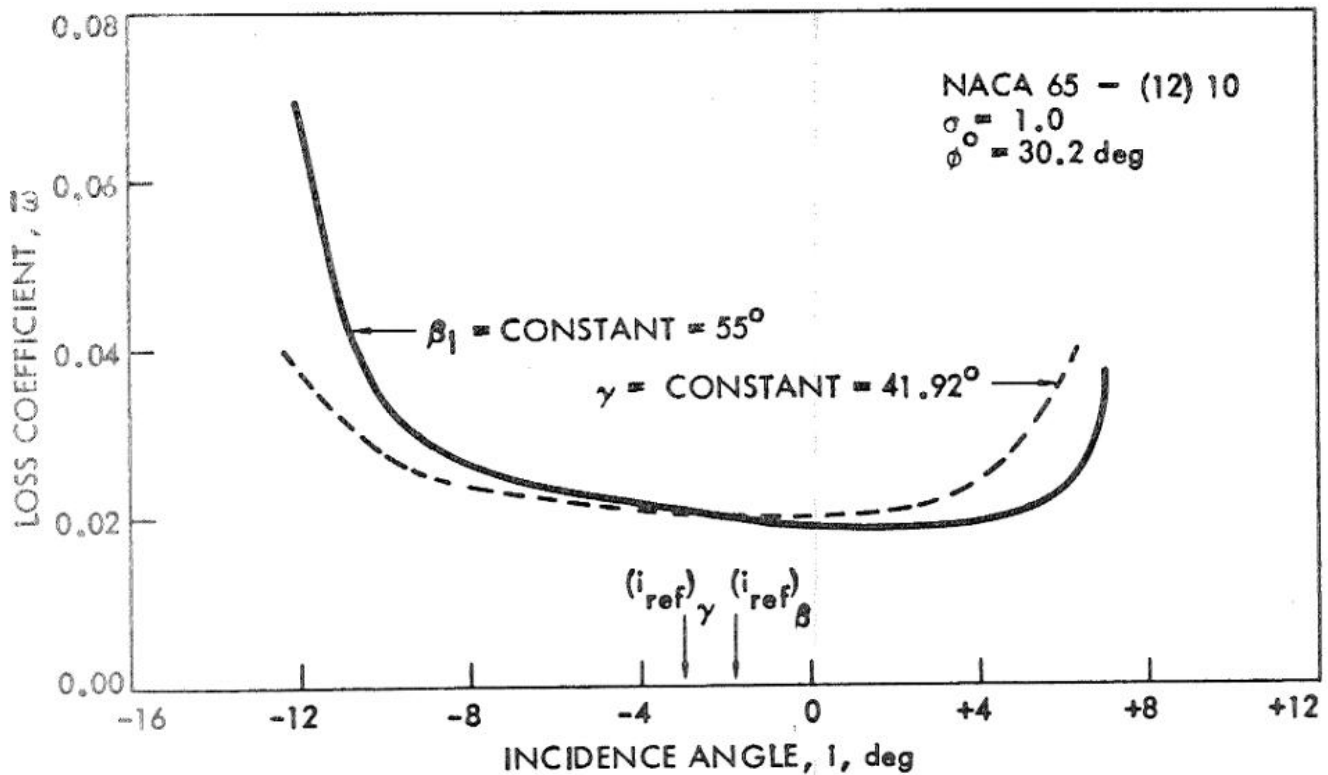
Fig. 3. Variation of loss coefficient with incidence angle at constant inlet flow angle and constant blade stagger angle (data from Ref. 5).

Charge/discharge unit of the plant

At the center of the charge/discharge unit is a large motor-generator, which acts as a motor in the charging phase and as a generator in the discharging phase. The motor-generators of the largest pumped storage power

plants have an output over 500 MW[80]. 99 % is a typical efficiency for large synchronous generators of several hundred megawatts.

The best round-trip efficiency is obtained with a solution where all turbomachines in the main circuit are directly connected to the main shaft of the motor-generator, i.e. they have the same rotational frequency with the generator. In the default design all turbines and compressors are subsonic, i.e. they operate entirely below the speed of sound at the design point. On other side of the generator are the main turbine and its 2 cryogenic compressors. On the opposite side of the generator are the main compressor, cryogenic turbine and the heat pump consisting of a medium size axial compressor, a cryogenic turbine and four counter flow plate and pipe heat exchangers. If the main shaft passes through the pipe shafts of turbines and compressors, then any individual turbomachine can be disconnected from the rotating main shaft.

The axial turbomachines operate in a pressure well, because the flow first accelerates to the designed axial velocity. The acceleration converts a part of the fluid's static enthalpy into kinetic energy by lowering the pressure and temperature. In the outlet diffuser, the flow correspondingly slows down to the velocity of the pipe, whereby the kinetic energy of fluid is converted back into enthalpy, increasing the gas pressure and temperature[81]. The efficiency of the fluid acceleration and diffusion is an input parameter. Its default value is 0.97, which is a typical loss in an optimized diffuser.

The main compressor and its motor-generator does not need any external startup motor, because they can be started by the normal startup procedure of the main turbine. When the generator's rotational frequency matches with the grid frequency, its magnets are enabled, the grid frequency starts to turn the main shaft, and the turbine can be disconnected from the shaft. The compressor may also be started directly by the motor-generator and frequency converters.

The gas incoming to turbomachines must be filtered to remove the dust particles in the same way as in the gas turbine power plants. A technical challenge is the hot gas from the upper high-pressure storage entering the main turbine, which exceeds the operating temperature of most conventional filter materials. High-temperature resistant ceramic or silicate fibers or combinations of them could be used as a filter material. If the filtering was done by a long sock inside the extended pipe, its pressure loss would be minimal, and the filter would be easy to clean or replace in a few hours' maintenance break.

The large hot gas pipe in the low-pressure storage can be made of ordinary steel, but all other pipes between the storage and the turbomachines must be made of austenitic steel. The tensile strength of austenitic steel may not be sufficient as such at the upper temperature of the high-pressure storage, in which case the pipe should be cooled and have inside insulation.

The heat pump, that pre-cools the fluid before the cryogenic turbine, has been designed to be directly connected to the motor-generator, but it may need also a frequency converter-controlled motor, because heat pump power varies depending on the cooling water temperature and the cooling requirement of the main charge circuit. The extra cooling power could be implemented also by a third heat pump unit, that would be switched on and off by need. The heat pump unit consists of 2 compressors with an additional gas-to-water cooler between them, a cryogenic turbine and four heat exchangers between the turbomachines. The heat pump's own power usage is about 6 % and its cooling power is usually about 4 % of the total load of the plant.

---

[80]https://voith.com/corp-en/11_06_Broschuere-Pumped-storage_einzeln.pdf
[81]https://en.wikipedia.org/wiki/Bernoulli%27s_principle#Compressible_flow_in_thermodynamics

The heat exchange power of the heat pump's counterflow plate heat exchangers is approximately 25% of the net power of the plant. For a 1000 MW plant, this would mean that with 1 mm plate gaps, a temperature difference of 2 Kelvins and a heat exchange coefficient of 100 W/m2/K, the volume of such heat exchanger could be perhaps 500-1000 cubic meters and its weight in tons would perhaps be of the same order of magnitude. The list price of such cooling system could be about 6-10 million euros[82] depending on the allowed pressure drop. Helium is the default working fluid of the heat pump because its exchangers are compact (compared to nitrogen) and helium heat exchangers have 0.2% better round-trip efficiency than nitrogen heat exchangers. The internal pressure of the heat pump is set to maximize the efficiency of its compressors and turbine.

If there is no need to produce district heat, the discharge and charge modes can operate at different pressure ratios so that the low and high temperatures of the main turbine and compressor are the same. The pressure difference requires that the excess gas in the charge mode is liquefied to a separate storage tank so that its boiling back to discharge cycle can be controlled. The liquidized part (about 2 ‰ for nitrogen) could be separated by directing the slightly wet gas coming out of from the cryogenic turbine at a sufficiently slow speed through a condensing fiber layer. The transition from the charge mode to the discharge mode is done by running cryogenic compressors for a maximum of a few hours, until the desired pressure ratio is reached. The switching time depends on the degree of filling of the energy storage. The switching a fully charged storage from charge pressure to the discharge pressure takes seven times longer than doing the same for an almost empty storage. The transition from the discharge mode back to the charge mode is done similarly by the cryogenic turbine. The pressure ratio can also be used to adjust the power of the main turbine and compressor to correspond to the amount of electricity sold or purchased.

The optimized turbomachinery designs

The program creates initial designs for all axial compressors and turbines of the plant and estimates their on-design efficiency with the mean line loss models. The result can be used as starting point for the actual design process and CFD modeling.

The default designs have been optimized for the best possible efficiency, but each optimization parameter also change the dimensions, the total number of blades and production cost of the turbomachinery. Because of high Reynold's numbers, the efficiency predictions are possible only if the blades have very tight manufacturing tolerances and smooth surfaces (0.4 μm Ra, smooth machine finished). All designs have stationary cascade rows, i.e. they have constant stage loading and flow coefficients and constant mean diameter.

The exceptional high efficiencies are the result of optimal number of stages, pressure ratio, aspect ratios, small tip gaps, high mass flow and optimal stage loading and flow coefficients. These parameters are hand tuned to the design tool produce highest possible efficiency prediction.

The design program creates Smith's charts for all turbomachinery designs, where its approximate machine loss is calculated with all possible combinations of stage loading coefficient $\Delta h/U^2$ and flow coefficient Vx/U. The

---

[82] https://www.ato.com/heat-exchanger-price-list

charts show the approximate area of the best efficiency, but the suggested optimal values must be tuned by testing to get the best possible efficiency.

Pressure ratio, low pressure, max temperature, rotational frequency, number of motor-generators and mass flow are common design parameters for all turbomachines. Reaction 0.5 would give the best efficiency prediction for all turbomachines if the structural constraints are ignored. The cryogenic turbines use reaction 0.55 because it allows a higher aspect ratio. The optimal compressor solidity (chord length / space between blades) is about 1.07 and 1.17 for turbines. In most cases the low centrifugal force allows the extending of the chord length with the increasing radius and to have about the same solidity for blade span. The constant mean diameter and equal stage power give the best efficiency for all presented turbomachine designs.
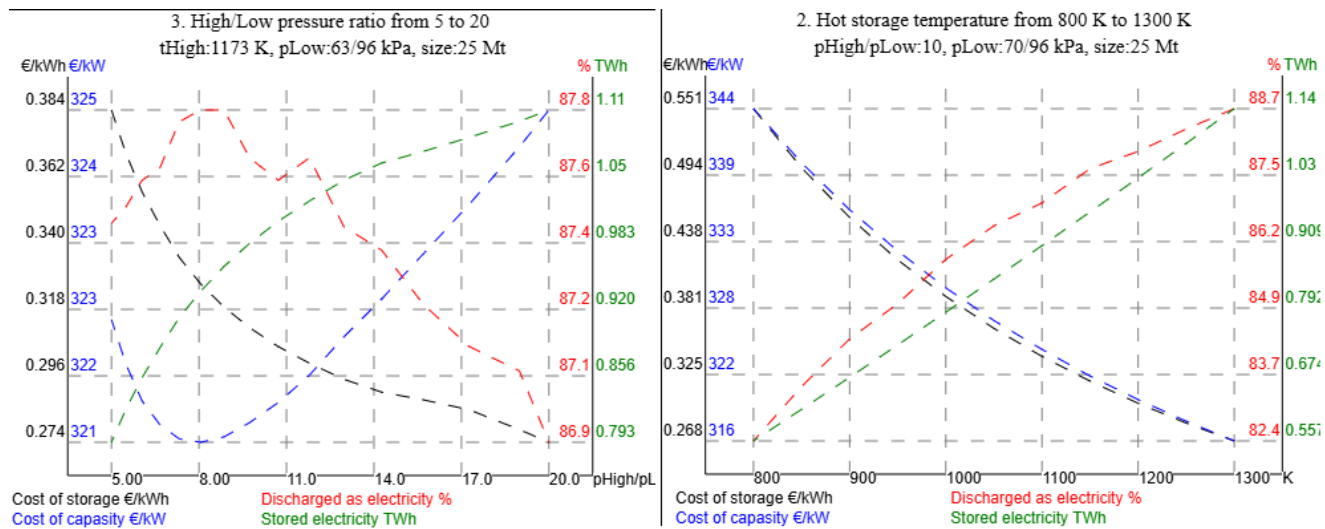
Figure 15. Round-trip efficiency, stored electricity and the unit cost of storage and capacity on variation of pressure ratio (left) and high temperature (right).

Pressure ratio 1:8 has about 1 % better round-trip efficiency than 1:20 and the implementation of the high-pressure storage is simpler with a lower pressure, but it has also about 20 % lower storage capacity. A lower pressure storage may have a bigger cross area and thus it enables higher mass flow and installed power capacity.

Available rock aggregate sets the upper limit for the high temperature. Every 100 K decrease of the high temperature drops the round-trip efficiency by 1 % and the discharge power by 100 MW for the same turbomachinery and mass flow.

The efficiencies of presented turbomachine designs are optimized with stage loading and flow coefficients, number of devices and stages, aspect ratio and the size of tip clearance.
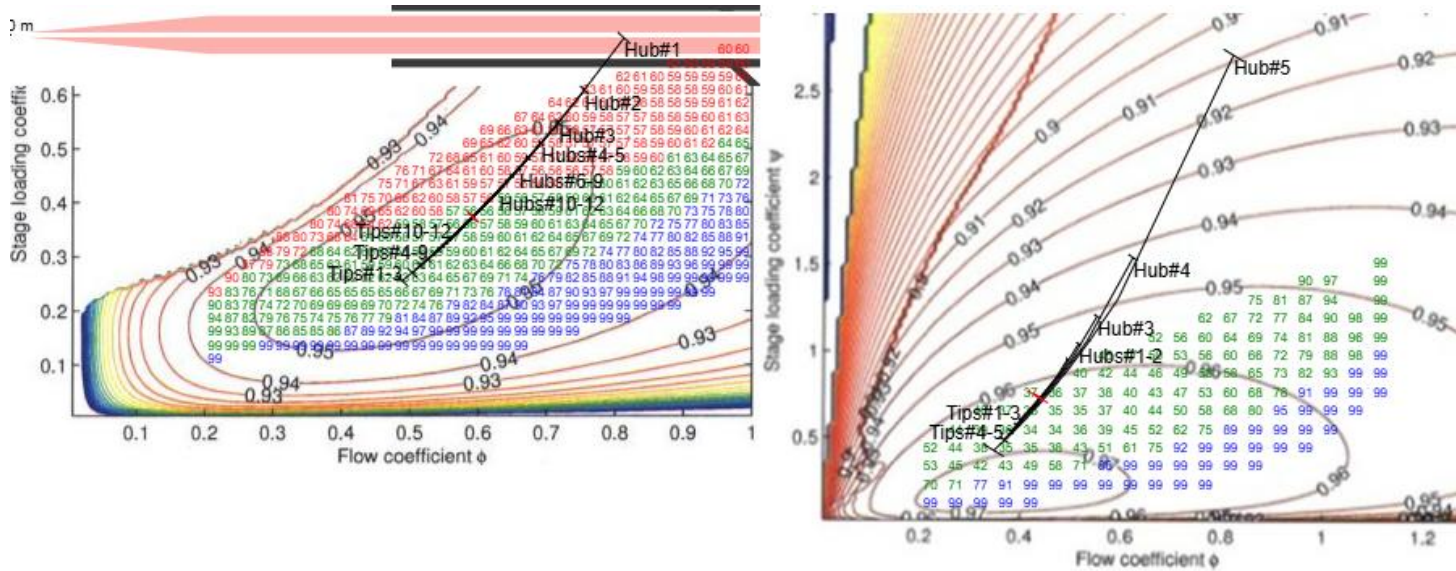
Figure 16 Smith's charts of plant's cryogenic compressor (left) and cryogenic turbine (right). Green machine loss values are subsonic, blue ones are intersonic and red ones would stall stall. Red cross line marks the position of the constant mean radius and black cross lines marks the position of blades' tips and hubs. Adiabatic efficiencies predicted by the loss models are 0.913 for the compressor and 0.975 for the turbine. The losses are calculated with the constant mass flow and rotational frequency and the resulted hub/tip ratio.

The optimal stage loading and flow coefficients seems to be about 0.36 and 0.59 for the compressor designs and about 0.70 and 0.45 for the turbine designs. If the pressure ratio, mass flow or high temperature is changed, then the number of stages must be readjusted to restore the best possible efficiency. The compressors' optimal stage loading and flow coefficients are almost in the middle the area of the expected best compressor efficiency, but turbines' values match better with the extrapolated optimum suggested by Kacker and Okapuu. Cryogenic compressor's stage efficiency decreases from 0.947 in the front to 0.935 in the rear. The efficiency of cryogenic turbine's middle stages is 0.971, but the stage efficiency drops below 0.97 in the first and last stage.

The number of turbomachine stages must be adjusted with the rotational frequency, mass flow, high temperature and pressure ratio of the plant. The heat pump has its internal pressure, which must be optional to get best possible efficiency. The number of stages should be incremented as far as it increases the efficiency and decreases the total number blades because of lower hub/tip ratio. The optimal low-pressure hub/tip ratio seems to be about 0.6 for the compressors and between 0.40 and 0.50 for the turbines.

The turbomachine endwall loss is divided by the aspect ratio in both loss models. Increased aspect ratio increases the number of blades and shrinks the chord length, but the height and maximum thickness of the blade and the total weight and surface area of all blades in cascade do not change. The higher number of smaller blades probably increases the total cost of turbomachine. A higher aspect ratio also increases the profile loss because of higher relative thickness tMax/chord. The optimal compressor aspect ratio giving the best efficiency is selected in an iterative loop for each compressor stage. Turbine profile loss is much less sensitive to increased relative thickness, and the predicted stage efficiency increases up to aspect ratio 12 which is given as input parameter for hot turbine. The stage aspect ratio may not cause the exceeding of the max allowed mean line tMax/chord parameter or the max enclosed cross area in rotor hub parameter (rotor hub solidity * tMax/chord). The first parameter is set as 0.18 from the previous figure of the typical turbine tMax/c values. The second parameter has an arbitrary default value 0.50. If the optimal chord length is

doubled, the predicted efficiency drops 0.75 % for the compressors and 0.5 % for the turbines. Aspect ratio 12 is possible only in the rear stages of the hot turbine. The cryogenic turbine stages have aspect ratios between 6 and 9 because otherwise the maximum enclosed cross area in rotor hub would exceed 0.5.

The tip clearance gap has a high impact on turbomachine endwall loss. Tip clearance depends on the operating temperature range, blade bending, the rotor elongation by the centrifugal stress and the type of the blade. Shrouded turbine blades usually have smaller tip clearances than the cantilevered compressor blades. Stable or controlled blade, disk and frame temperatures, low centrifugal stress and small thermal expansion of the ambient and cryogenic blades should make possible small tip clearance gaps. The tip clearance gaps of big hot turbomachines are above 0.5 mm, that matches well with the typical tip clearance gap of industrial compressors: 20–50 thousandths of an inch, or about 0.5–1.3 mm in 2000[83]. The thermal extension of the hot high-pressure blades may be up to 1.5 %, but the blades of other turbomachines operating in ambient and cryogenic temperatures shrink less than 0.2 % because of the smaller temperature range and lower coefficient of thermal expansion.   Their minimum tip clearance gap is set as 0.25 mm. The used tip clearance gap is the bigger one from two design parameters: absolute minimum tip gap of the turbomachine and percent of blade span. If hot compressor tip clearance gap is increased from 0.25 % to 0.5 % or 1 %, its efficiency drops 0.2 % and 0.9 % respectively. The size of the stage tip clearance gaps can be controlled by cooling or heating its disk. It shrinks or extends both rotor and stator clearance gaps at the same time.

The next figure is the default design of cryogenic compressor maintaining the system high-pressure for the main turbine. Koch and Smith loss model predicts its adiabatic efficiency 91.3 %. Its mass flow is only half of the main turbine mass flow, and the number of devices is doubled to adapt it better with the rotational frequency. The cross area is increased in the same proportion as blockage increases. The geometry of the inlets and outlets is for reference only. The geometry of the inner part matches with the used loss model parameters. The optimized aspect ratio and the stagger angles are calculated by the loss model. The compressor has an IVG (inlet vane guide), which loss is assumed to be included in the default 3 % loss in the inlet.

---

[83] https://www.netl.doe.gov/sites/default/files/gas-turbine-handbook/2-0.pdf

4 * 40 MW Axial Subsonic Cryogenic Compressor synchronized with Motor-Generator

Fluid: Nitrogen
Adiabatic efficiency: 0.913 (=>stage machine efficiency: 0.931650), average stage efficiency by DF and eqDR: 0.940
P-out/P-in: 11.13 (max: ~33.38), Mass flow: 488 kg/s
Constant axial velocity: 80.0 m/s (<=0.45 mach)
Rpm: 1500, 12 stages, reaction: 50 %, mean line solidity: 1.05
Adaptive aspect ratio (h/c); Hub/Tip ratios from 0.60 to 0.91
Max suction side relative velocity: 0.94 Mach
Max stall margin: 77 %
Total number of cantilevered stator and rotor blades: 2428

The compressor stages on Smith's chart. The stage(s) machine loss ‰ variation by stage loading and flow coefficients.
Green loss means that the 1st stage is subsonic, blue loss values are intersonic and in red ones the hub of the 1st stage would stall.
Best subsonic efficiency 0.944 of stage 1 when load coefficient: 0.3500 and flow coeffient: 0.5750 (hub/tip: 0.62 - 0.92, stall margin: 0.64)

Below are the states, parameters and characteristics of the compressor stages. The bending resistance of the blade is not added to the centrifugal force caused by the rotation movement, because in the bending the sum of the compression and stretching of the opposite sides is zero. Chord length, rotor tMax/c, stator tMax/c, stagger angle, stage loading coefficient and flow coefficient are the values of the mean flow.

Cold compressor	Inlet	Stage 1	Stage 2	Stage 3	Stage 4	Stage 5	Stage 6	Stage 7	Stage 8	Stage 9	Stage 10	Stage 11	Stage 12	Exit	Pipe out
Temperature K	76	73	79	85	92	99	106	113	120	127	134	140	147	154	158
Pressure kPa	69	58	78	102	132	167	208	255	310	372	442	521	609	706	771
Vx m/s	25	80	80	80	80	80	80	80	80	80	80	80	80	80	13
Diameter mm	2797	2099	2037	1987	1948	1917	1891	1871	1854	1839	1827	1817	1809	1801	1670
Gas flow m3/s	153	177	142	117	98	83	71	62	54	47	42	38	34	30	29
P2/P1	0.83	1.35	1.32	1.29	1.27	1.25	1.23	1.21	1.20	1.19	1.18	1.17	1.16	1.09	
Power MW		3.33	3.33	3.33	3.33	3.33	3.33	3.33	3.33	3.33	3.33	3.33	3.33		
Efficiency	0.970	0.947	0.945	0.944	0.943	0.942	0.941	0.940	0.939	0.938	0.937	0.936	0.937	0.970	
Entropy increase J/kg/K	1.61	4.62	4.41	4.17	3.96	3.77	3.60	3.45	3.31	3.20	3.09	3.00	2.81	0.76	
Static enthalpy kJ/kg	76	72	79	86	93	100	107	113	120	127	134	141	148	154	158
Stagn. enthalpy kJ/kg	77	77	83	90	97	104	111	118	124	131	138	145	152	159	159
Delta kinetic J/kg	3794	0	0	0	0	0	0	0	0	0	0	0	0	-4020	0
Delta kinetic ‰		0	0	0	0	0	0	0	0	0	0	0	0		
rTip mm		1047	1017	992	972	956	944	933	925	918	912	907	902		
Mean radius mm		863	863	863	863	863	863	863	863	863	863	863	863		
Hub/Tip		0.60	0.66	0.72	0.76	0.79	0.82	0.84	0.86	0.88	0.89	0.90	0.91		

Rotor mean height mm	398	325	268	224	190	164	142	124	110	97	87	78	
Rotor chord mm	109	100	89	79	71	64	59	54	49	43	39	35	
Tip gap mm	0.80	0.65	0.54	0.45	0.38	0.33	0.28	0.25	0.24	0.24	0.24	0.24	
Aspect ratio h/c	3.65	3.24	3.03	2.85	2.68	2.56	2.42	2.31	2.24	2.25	2.25	2.22	
Rotor blades	52	57	64	72	80	89	97	106	116	131	147	161	
Stator blades	58	63	70	78	87	96	104	113	123	139	155	170	
Rotor mean tMax/c %	4.1	4.1	4.3	4.4	4.6	4.7	4.8	4.9	5.1	5.4	5.7	6.0	
Rotor hub tMax/c %	9.6	9.3	9.4	9.5	9.7	9.9	10.0	10.2	10.5	11.1	11.7	12.2	
Rotor hub solidity*tMax/c	0.14	0.12	0.12	0.12	0.12	0.12	0.12	0.12	0.12	0.12	0.13	0.13	
Stator mean tMax/c %	3.3	3.3	3.3	3.4	3.5	3.6	3.6	3.7	3.8	4.0	4.2	4.4	
Tip stagger angle °	42	44	40	39	39	38	38	38	37	37	37	37	
Mid stagger angle °	39	36	36	36	36	36	36	36	36	36	36	36	
Hub stagger angle °	26	28	30	32	33	33	34	34	34	34	35	35	
Rotor mid $\beta 1/\beta 2$ °	49/28	49/28	49/28	49/28	49/28	49/28	49/28	49/28	49/28	49/28	49/28	49/28	
Suction side $\beta 1/\beta 2$ °	54/18	52/26	52/26	52/26	51/26	51/26	51/26	51/26	51/26	51/26	51/25	51/25	
Stator $\alpha 2/\alpha 3$°	-49/-28	-49/-28	-49/-28	-49/-28	-49/-28	-49/-28	-49/-28	-49/-28	-49/-28	-49/-28	-49/-28	-49/-28	-28
vRel tip inlet Mach	0.76	0.73	0.70	0.67	0.64	0.61	0.59	0.57	0.56	0.54	0.52	0.51	
max ss vRel Mach	0.88	0.94	0.83	0.79	0.75	0.72	0.69	0.67	0.65	0.63	0.61	0.59	
Re(c) E06	6.98	7.49	7.38	7.29	7.22	7.25	7.25	7.17	7.05	6.69	6.39	6.20	
Blade bending kN/m	8.6	8.6	8.6	8.6	8.6	8.6	8.6	8.6	8.6	8.6	8.6	8.6	
Bending stress MPa	175	175	175	175	175	175	175	175	175	175	175	175	
Centrifugal stress MPa	38	32	28	24	21	18	16	14	13	12	11	10	
Mean line load coefficient	0.37	0.37	0.37	0.37	0.37	0.37	0.37	0.37	0.37	0.37	0.37	0.37	
Mean line flow coefficient	0.59	0.59	0.59	0.59	0.59	0.59	0.59	0.59	0.59	0.59	0.59	0.59	
Diffusion factor DF	0.46	0.46	0.46	0.46	0.46	0.46	0.46	0.46	0.46	0.46	0.46	0.46	
Equivalent DR*	1.81	1.81	1.81	1.81	1.81	1.81	1.81	1.81	1.81	1.82	1.82	1.81	
deHaller Num	0.74	0.74	0.74	0.74	0.74	0.74	0.74	0.74	0.74	0.74	0.74	0.74	
AN2 E08	0.05	0.04	0.03	0.03	0.02	0.02	0.02	0.02	0.01	0.01	0.01	0.01	
Rotor/stator loss(h) %	2.7/2.6	2.8/2.7	2.8/2.8	2.9/2.8	3.0/2.9	3.0/2.9	3.1/3.0	3.1/3.0	3.2/3.1	3.2/3.1	3.3/3.2	3.3/3.0	
Profile/endwall loss(h) %	4.3/1.0	4.4/1.1	4.4/1.2	4.4/1.3	4.4/1.4	4.5/1.5	4.5/1.6	4.5/1.6	4.5/1.7	4.6/1.7	4.7/1.8	4.6/1.7	
Pressure loss error %	0.000	0.000	0.000	0.000	0.000	0.000	0.000	0.000	0.000	0.000	0.000	0.000	
h loss approximation/h loss %	103	104	104	104	104	104	104	104	104	104	104	104	
Rotor/stator loss error ‰	0/0	0/0	0/0	0/0	0/0	0/0	0/0	0/0	0/0	0/0	0/0	0/0	
$\Delta p/(\rho \cdot Vx^2)$	1.14	1.12	1.11	1.10	1.09	1.08	1.08	1.07	1.07	1.06	1.06	1.06	
$(\Delta h-(U1^2-U2^2))/maxVrel^2$	0.45	0.45	0.45	0.45	0.45	0.45	0.45	0.45	0.45	0.45	0.45	0.45	
Blockage factor	0.99	0.98	0.97	0.97	0.97	0.97	0.97	0.97	0.97	0.97	0.97	0.97	
Machine loss/P0 loss coefficient	1.86	1.89	1.91	1.93	1.94	1.96	1.97	1.98	1.99	2.00	2.01	2.02	
Tip % of stall	41	52	34	34	35	36	36	36	37	37	37	38	
Mid % of stall	59	42	42	42	42	41	41	41	41	41	41	42	
Hub % of stall	77	64	57	53	50	48	47	46	45	44	43	43	

2 * 589 MW Axial Subsonic Turbine synchronized with Motor-Generator

Fluid: Nitrogen
Adiabatic efficiency: 0.976 (=>stage machine efficiency: 0.967202), average stage efficiency by Kacker and Okapuu:0.969
P-in/P-out: 10.73, Mass flow: 976 kg/s
Constant axial velocity: 142 m/s (<=0.27 mach)
Rpm: 1500, 9 stages, reaction: 50 %, mean line solidity: 1.17
Adaptive aspect ratio (h/c); Hub/Tip ratios from 0.87 to 0.44
Max relative exit velocity of the last rotor: 0.63 Mach
Total number of shrouded stator and rotor blades: 5139

The turbine stages on Smith's chart. The stage machine loss ‰ variation by stage loading and flow coefficients.
Green loss means that the last stage is subsonic and blue loss values are intersonic.
Best subsonic efficiency 0.967 of stages 2, 6, 8 when load coefficient: 0.5000 and flow coefficent: 0.4000 (hub/tip: 0.91 - 0.64)

The previous figure is the default design of the main turbine. Kacker and Okapuu loss model predicts its adiabatic efficiency 97.6 %.

Hot turbine	Inlet	Stage 1	Stage 2	Stage 3	Stage 4	Stage 5	Stage 6	Stage 7	Stage 8	Stage 9	Exit	Pipe out
Temperature K	1172	1165	1108	1051	994	936	878	818	759	698	636	645

Pressure kPa	766	746	605	487	388	304	236	179	133	97	68	71
Vx m/s	53	142	142	142	142	142	142	142	142	142	142	67
Diameter mm	3259	4194	4236	4286	4346	4422	4516	4636	4790	4991	5260	7035
Gas flow m3/s	444	453	531	626	743	891	1080	1325	1649	2089	2705	2618
P1/P2	1.03	1.23	1.24	1.26	1.27	1.29	1.32	1.34	1.38	1.42	0.96	
Power MW		65.43	65.43	65.43	65.43	65.43	65.43	65.43	65.43	65.43		
Efficiency	0.970	0.960	0.967	0.969	0.970	0.971	0.971	0.972	0.971	0.968	0.970	
Entropy increase J/kg/K	0.23	2.56	2.20	2.16	2.22	2.32	2.43	2.57	2.86	3.47	0.42	
Static enthalpy kJ/kg	1280	1271	1203	1136	1069	1002	935	867	800	733	666	675
Stagn. enthalpy kJ/kg	1281	1281	1214	1147	1080	1013	946	879	812	745	677	677
Delta kinetic J/kg	8720	1078	0	0	0	0	0	0	0	0	-8944	0
Delta kinetic ‰		16.07	0	0	0	0	0	0	0	0		
rTip mm		2116	2141	2171	2209	2256	2316	2393	2494	2628		
Mean radius mm		1971	1971	1971	1971	1971	1971	1971	1971	1971		
Hub/Tip		0.87	0.85	0.82	0.79	0.75	0.70	0.64	0.55	0.44		
Rotor mean height mm		291	342	406	487	591	727	911	1171	1572		
Rotor chord mm		44	39	36	41	49	61	76	98	131		
Tip gap mm		0.73	0.86	1.02	1.22	1.48	1.82	2.28	2.93	3.93		
Aspect ratio h/c		6.65	8.85	11.14	12.00	12.00	12.00	12.00	12.00	12.00		
Rotor blades		332	375	397	357	294	239	191	148	111		
Stator blades		360	407	434	391	325	266	214	169	129		
Rotor mean tMax/c %		18.0	18.0	18.0	17.6	15.9	14.2	12.6	10.9	9.1		
Rotor hub tMax/c %		36.9	37.1	37.3	36.8	33.6	30.4	27.4	24.4	21.5		
Rotor hub solidity*tMax/c		0.47	0.48	0.49	0.49	0.46	0.44	0.42	0.42	0.45		
Stator mean tMax/c %		13.6	13.6	13.7	13.6	12.4	11.3	10.2	9.1	8.0		
Mid stagger angle °		22	22	22	22	22	22	22	22	22		
Rotor tip β2/β3 °		-24/62	-25/62	-26/62	-28/62	-29/62	-31/63	-33/63	-36/63	-39/64		
Rotor β2/β3 °		-18/62	-18/62	-18/62	-18/62	-18/62	-18/62	-18/62	-18/62	-18/62		
Rotor hub β2/β3 °		-11/62	-9/62	-7/62	-5/62	-1/62	3/62	10/62	20/62	36/62		
Stator α1/α2°		0/-62	18/-62	18/-62	18/-62	18/-62	18/-62	18/-62	18/-62	18/-62	18	
vRel tip outlet Mach		0.46	0.47	0.48	0.50	0.52	0.54	0.56	0.59	0.63		
Re(c) E06		0.54	0.42	0.35	0.33	0.35	0.37	0.39	0.42	0.46		
Blade bending kN/m		41.7	41.7	41.7	41.7	41.7	41.7	41.7	41.7	41.7		
Bending stress MPa		115	172	228	228	228	228	228	228	228		
Centrifugal stress MPa		63	75	83	97	114	136	162	196	236		
Mean line load coefficient		0.70	0.70	0.70	0.70	0.70	0.70	0.70	0.70	0.70		
Mean line flow coefficient		0.46	0.46	0.46	0.46	0.46	0.46	0.46	0.46	0.46		
AN2 E08		0.07	0.08	0.10	0.12	0.14	0.17	0.21	0.26	0.33		
Rotor/Stator loss(h) %		2.0/2.1	1.8/1.6	1.6/1.5	1.6/1.4	1.5/1.4	1.5/1.4	1.4/1.4	1.5/1.3	1.9/1.3		
Profile/trailing loss(h) %		1.5/1.1	1.2/1.1	1.2/1.1	1.2/1.1	1.2/1.1	1.1/1.1	1.1/1.1	1.2/1.1	1.5/1.0		
Clearance/secondary loss(h) %		0.2/1.3	0.2/0.8	0.1/0.7	0.1/0.6	0.1/0.6	0.1/0.6	0.1/0.6	0.0/0.6	0.0/0.6		
Rotor/stator loss error ‰		1/1	0/0	0/0	0/0	0/0	0/0	0/0	0/0	0/0		
Machine loss/P0 loss coefficient		1.18	1.18	1.18	1.17	1.17	1.16	1.15	1.14	1.12		

These and 5 other turbomachine designs are available on the web site.

Heat pump heat exchangers

The heat pump turbomachines are integrated with four quite massive counter flow plate micro heat exchangers. These counter flow plate heat exchangers have cross flow triangles in opposite corners where the other fluid flows in and out in 45° angle. The cross flow is defined to be 25% of the panel length. The algorithm designs the heat exchangers from these design parameters:

- Coolant fluid rotating between turbine and compressors through the four heat exchangers. The coolant fluid should have lower dew point than the main fluid of the storage. Helium gives 0.4% better round-trip efficiency for than nitrogen when nitrogen is the main fluid, but helium and nitrogen perform as well as coolants of argon.
- Internal high pressure of the storage is selected to have optimal hub/tip ratio for heat pump compressors.
- Relative pressure loss inside heat exchanger. The very low default value 0.001 gives 0.2% better system round-trip efficiency than 0.002 with 3.5 M€ additional cost. The pressure loss outside the micro channels is assumed to be zero because of very low velocity and Reynolds numbers of external cross flow channels (< 1).
- Heat exchanger panel length does not change the total cross area of heat exchanger, but it increases the cross area of a micro channel. If the panel length is increased from default 0.5 m to 1 m, the total cost estimation is increased by 3.2 M€ and the number of micro channels is decreased by 50%. The channel size and panel length would be set by the degree of the fouling and the manufacturing capabilities. All other fluids except the cryogenic high-pressure fluid of the main storage can be expected to be very clean because of a closed loop and any incoming dust of cryogenic nitrogen flow can be filtered without significant pressure drop because of very low velocity. The distilled cooling water may be mixed with alcohol in a temperate climate because it would make possible to use the wintertime temperatures for the cooling and to store the wintertime cold to a drilled rock storage.
- Heat exchanger temperature difference defines the size and efficiency of the heat exchanger. If the temperature difference is decreased from 2 K to 1 K, the system round-trip efficiency increases 0.2% and the cost of heat exchangers by 6.1 M€.
- Cooling water temperature defines the work done by heat pump compressors that is the main source of the loss. The system round-trip efficiencies with variation of cooling water temperature are: -10 C°: 89.4%, 0 C°: 89.1%, 5 C°: 88.9%, 10C°: 88.8% and 20C°: 88.4%. The utilization and storing the possible winter-time cold may be an economic way to improve the round-trip efficiency of the system.
- 2 configuration parameters define the structural strength of the micro channels by adjusting the aspect ratio and thickness of walls. The first parameter defines the panel height divided by sheet thickness at 100 kPa pressure difference (default 40). The second parameter is the width of high-pressure channel divided by thickness of sheet (default 20) at 100 kPa pressure difference. The algorithm decreases both values when the pressure difference between the micro channels exceeds 100 kPa. If the pressure difference exceeds 800 kPa, the strength must be increased by other means, for example by changing the straight wall between the channels to an arc or by changing the aluminum to stainless steel. The default pressure differences of the default design are 426, 266, 44 and 45 kPa. The default structural configuration parameters have not been analyzed, but the produced structure must be quite strong, because the internal pressure inside aluminum soda cans is about 250 kPa at 20 C°, its walls are thinner (~0.1 mm) and diameter about 66 mm.
- Heat exchanger panel width to length (default 4) defines the length triangular cross flow areas in the opposite corners. That length (25%) is not included in the heat exchange of the counter flow area.
- There are also 3 extra parameters to calculate a cost estimation for the heat exchangers. The cost estimation is the sum of the material costs, the processing cost of panel blocks and the other costs scaling with the heat exchanger cross area, typically 55-66% of all costs. The material costs is the cost of cryogenic 5000-series 0.3 mm aluminum sheets per ton. The default processing cost estimation 5€/m2 is based on the unit production cost of a soda can (0.06 – 0.12 $). The other costs include the

margin, design, installation work and the frame, external channels and steel pipe around the wall of heat exchanger blocks to contains the pressure. The estimated cost of all heat exchangers is 14 M€ that is about 34% of estimated cost of all turbomachines (41 M€) based on the number of rotor and stator blades.

The used Nusselt number is 8.6 (fully developed forced laminar flow in a panel heat exchanger). The same hydraulic diameter of channel rectangle is used for both pressure drop and heat transfer calculations. Aluminum has a very high heat conductivity, and the side walls probably transfer almost the same amount heat as the walls between different fluids. There is also some heat leak caused by aluminum sheet. Those errors can be compensated by decreasing the desired temperature difference by 2-3%.

The next table contains the heat exchanger properties produced by the default parameter values. The algorithm uses the thermodynamic values of fluids in the middle temperature ((Tin+Tout)/2). The result is verified by the sum of actual pressure loss in 10 subsections. The small error between actual and desired pressure loss (~0.3%) is more likely caused by 1% error margin of the heuristic loops. The heuristic algorithm is implemented in method calcFlatPlateHeatExchanger- on HTML page.

Counter flow plate heat exchanger	Nitrogen to Helium HE	Internal Helium to Helium HE	Helium to water HE 1	Helium to water HE 2
Coolant	Helium	Helium	Water	Water
Cooled fluid	Nitrogen	Helium	Helium	Helium
Coolant mass flow kg/s	187	187	232	232
Cooled mass flow kg/s	866	187	187	187
Plate height mm	2.072	2.441	2.793	2.582
Plate width m	0.126	0.126	0.124	0.124
Plate length m	0.503	0.505	0.496	0.498
Effective length m	0.377	0.379	0.372	0.373
Sheet thickness mm	0.221	0.122	0.140	0.129
Coolant passage height*width mm	0.981*18.8	1.13*3.95	0.373*6.27	0.390*5.80
Cooled passage height*width mm	0.650*1.04	1.06*1.51	2.14*6.27	1.93*5.80
Coolant hydraulic diameter mm	0.933	0.880	0.352	0.366
Cooled hydraulic diameter mm	0.399	0.624	1.596	1.450
Coolant inlet temp K	135.61	155.65	283.00	283.00
Coolant exit temp K	155.65	283.00	306.07	306.20
Fluids' temp difference K	2.00	2.00	2.00	2.00
Coolant pressure kPa	339	339	456	456
Coolant pressure drop Pa	340	337	1928	1871
Cooled pressure kPa	765	501	412	501
Cooled pressure drop Pa	767	507	414	501
Coolant mid flow m3/s	169.51	254.08	0.23	0.23
Cooled mid flow m3/s	47.18	172.27	280.36	230.65
Coolant mid velocity m/s	2.702	1.037	0.003	0.003
Cooled mid velocity m/s	0.747	0.742	3.359	3.340
Coolant mid ht coefficient W/m2	848	1184	14116	13596
Cooled mid ht coefficient W/m2	296	1671	799	880
Coolant mid Re	62	30	1278	1321
Cooled mid Re	538	31	181	198
Plates' total cross area m2	244	575	111	94
Plates' total volume m3	123	291	55	47
Micro channels/m2 (cross area)	409408	351613	111728	130728
Metal heat leak %	3.24	4.07	0.66	0.55
Plates' total weight in tons	91	115	18	15
Plates' total sheet area M2	118537	238064	39509	36360

Material costs of aluminum sheets €	226639	287422	44545	37899
Processing costs of plate blocks €	592687	1190320	197544	181801
Other costs €	976876	2301941	445278	377122
Total costs €	1796202	3779683	687368	596821

The profitability and capital costs of the energy storage

The cost calculation of a completely new plant, process, equipment or work phase is always very uncertain. The most important thing is to carry out the work as far as possible using methods known to be cost-effective or by applying them, and to use existing technology as far as possible. The construction of the energy storage mainly consists of large-scale open-pit mining with large machines, crushing aggregate, compacting and strengthening rock walls, and excavating gas pipelines embedded in the wall. The unit costs of these are generally known and the contract prices can therefore be estimated in advance and competitively priced. New work phases that are more difficult to estimate include the installation or masonry of distribution channel elements that can withstand the weight of the upper crushed stone, mixing loose stone wool (or biochar) into crushed stone having maximum porosity, building an elastic gas-tight layers above the hot high-storage and around the above-ground part of the low-pressure storage. The pipes of hot and cryogenic gas, their control valves are, at least for the most part, conventional process technology. The total length of the pipelines of various sizes is probably about two kilometers.

The costs of building a storage are significantly reduced if the storage is built in an abandoned open pit, and especially if the quarry's already stockpiled waste rock can be reused as crushed stone of the storage. In this case, the compacted walls of the open pit can act as pressure insulators, and thermal expansion is directed only upwards. In principle, any screened crushed stone is suitable for a low-pressure storage, but the crushed stone at the top of a high-pressure storage should be made of at least mafic rocks. However, the waste rock from ore mines is very often at least partly mafic or ultramafic rock.

Among the new work phases, the casting and masonry of vault structures and sloping wall structures are common construction techniques. Insulation layers can be made by alternately spreading evenly sized crushed stone and insulation in a thin mat with trucks and then harrowing them together. Stone wool can probably be mixed directly into the crushed stone before spreading.

In the United States, the average price of biochar in 2023 was $131/ton[84], so on an industrial scale, the price per ton of biochar is likely to be somewhere between 100–200 euros. The density of biochar is approximately 200 kg/m^3. In this case, the price of one cubic meter of insulation would be less than 20 euros. It would be most economical to produce biochar in connection with a thermal power plant operating on wood or peat, where the gasified half of the biomass would produce heat and electricity. Also, when using loose stone wool at double the density, the price of an insulation would probably be less than 20 euros/m^3.

The size of the plant buildings are probably about the same as a simple cycle gas turbine plant of equivalent capacity without heat recovery. The size of the hot compressors and turbines is significantly smaller because all

[84]https://cloverly.com/ultimate-business-guide-to-biochar/#:~:text=Biochar%20price%3A%20The%20average%20biochar,their%20portfolio%20of%20carbon%20credits.

combustion process technology is omitted. The cryogenic compressors and turbines are also small. Based on the compressor modelling, it appears that the turbines and compressors of the main circuits would fit into one trailer combination, at least in terms of size, so their estimated cost is probably overestimated. The heat exchangers integrated to the heat pumps and motor-generators would take most the space. The volume of the heat exchangers was estimated 2,500 cubic meters, and the motor-generators would probably need at least the same space. The expansion storage for liquefied gas would be 15,000 m^3 for nitrogen and 5,000 m^3 for argon. It would fit in an underground cylindrical austenitic steel storage insulated in the same was as any LNG storage.

If the electricity storage concept presented here proves to be technically and economically feasible, it would open a new market worth at least several billion for manufacturers of turbomachines. That would likely enable rapid product development of equipment tailored to the concept and perhaps also reasonable prices.

The cost of the turbomachines is estimated by the total number of blades. The price range of an aviation OEM compressor or turbine blade is 20 – 200 \$. The default cost estimation turbomachinery is the total number of blades multiplied by 1000 \$. The cost of the blades is probably more than all other parts combined.

The profitability of the investment depends on the plant's construction costs, operating costs, electricity price fluctuations and the total amount of electricity sold annually. The previous three years have been exceptionally turbulent in the Finnish and Nordic electricity markets, but based on futures, price fluctuations would be leveling out, at least for now. In the long term, however, the trend seems to be the opposite, because electricity consumption is predicted to grow rapidly, while the share of electricity production dependent on the sun and wind is constantly increasing and the continuous increase in the price of emission allowances will remove the last fossil energy plants from the market. It can therefore be assumed that in the longer term, turbulence will continue, and thus the need for regulated electricity production will also continue to grow. If the plant's highest purchase price of electricity excluding tax had been 2.5 cents and the lowest selling price 3 cents, then the average margin during the previous year would probably have been at least 5 cents and annual electricity sales perhaps 4 TWh. In that case, the plant's sales margin would have been over 200 million euros. If the degree of automation is high, the annual operating and maintenance costs of the plant will probably be around 10–20 million euros, in which case the annual return on investment would be at least 20 % based on the default parameters and expected capital costs of the design program.

Verification of the feasibility of energy storage

This plan is currently based solely on public sources, so the suggestions and preliminary estimates presented above must be verified either by simulation or measurement.

The most important things to verify are:

1. The performance of the carbon-free mild steel and aluminum used in the elastic gas insulation of the high-pressure storage must be tested by simulating the expected thermal movement of the crushed stone. The insulation can be double checked by an extra layer of elastic water ice and crushed stone.

2. What is the U-value, compressive strength and gas permeability in convection of a compacted 1:1 crushed stone and stone wool insulation in the expected temperature range? The stone particles should be uniform in size and have maximum porosity.
3. Measuring the hydraulic conductivity, thermal expansion coefficient, internal heat transfer and heat exchange efficiency of the screened crushed stone. The heat exchange efficiency is measured using forced convection at the designed gas flow rate.
4. Simulation and measurement of the gradual compression, and long-term durability of the mafic crushed stone mixture of the high-pressure storage when the crushed stone temperature is changing between the min and max temperature and the thermal expansion is compressing the crushed stone.

Most points can be measured empirically, for example, in a decommissioned steam power plant's pressure boiler, the central part of which is filled with the investigated crushed stone and the edge parts are insulated with crushed stone and stone wool or biochar mix. Argon or nitrogen gas, pressurized with a centrifugal or screw compressor and heated with possible additional resistors, is led to the upper part of the boiler. The lower part has an adjustable pressure equalizer and a return pipe to the compressor. The outer surface of the pressure boiler has a dense water-cooling pipeline inside the insulation. The U-value of the crushed stone insulation can be calculated from the cooling power. The hydraulic conductivity and the heat exchange efficiency of the crushed stone mix can be measured from the pressure and temperature change of the gas in inlet and outlet.

The high-pressure storage bottom can be manually pressed either with an expanding vessel made of carbon-free steel, which is pressurized with a second compressor to the desired pressure of 20–40 atmospheres. Economical simulation of dozens of heating and cooling cycles may require parallel thermal storages where the hot and cryogenic cold released from the measuring storage can be stored. If there is a heat exchanger in between, the second storage does not even need to be pressurized, but can be, for example, a vessel inside a welded austenitic steel plate covered with stone wool, which is heated and cooled with air.

In Finland, Olivine aggregate can be ordered, for example, from Luvia stove stone quarries, but the purity of the aggregate and the screening of measurable crushed stone fractions may require special arrangements. Biochar can be ordered in cubic meters and in 1.6m3 big bags. When purchasing and testing biochar, it is important to determine its pore size, which is essential for insulating thermal radiation. Biochar produced at high temperatures has the smallest pore size. In addition to biochar, it is also worth measuring the properties of the stone wool crushed stone. With a density of 0.036 for ordinary blown wool, convection may be a significant problem. The density of the stone wool used in the insulating plastering of high vertical walls is 0.075, which would probably be a sufficient density for the stone wool mixed with the crushed stone.

Summary

This study is a concrete proposal for the implementation of a low-cost and high-efficiency PTES plant. These are the main findings in this study:

- A very efficient closed two-way Brayton cycle can charge and discharge the heat and cryogenic cold in a massive low-cost thermal energy storage made of crushed stone and crushed ice.
- The thermal energy storage can be made using very affordable open-pit mining technology, or alternatively it can be built into an abandoned open-pit quarry and recycle its waste rock
- The hot top side of the high-pressure storage can be made of heat-resistant ultramafic and mafic rocks.
- The energy storage can be insulated with a 50/50 mixture of very porous crushed stone and stone wool (or biochar) that can withstand the high pressure and temperature of the energy storage
- The hot high-pressure storage section can be pressure insulated with elastic carbon-free mild steel that adapts to the thermal movement of the crushed stone. Aluminum, technical rubber and bitumen can be used in the cooler edge section.
- The predicted excellent 87.8 % electricity round-trip efficiency can be achieved with the conventional axial turbomachinery technology.
- The amount of crushed stone can be halved by using crushed ice to store the cryogenic cold. Crushed ice has about 50% better volumetric heat capacity at 77K than crushed stone.
- The long-term simulation of the storage shows that the system can utilize almost 60% of the theoretical maximum heat capacity of the crushed stone in the hot high-pressure storage.

These points have been found to be technically feasible to implement through software modeling and are estimated to be very cost-effective compared to other electricity storage methods. The modeling has considered, as accurately as possible, the properties of the materials found in other studies, the physical formulas related to the modeling, known technical limitations, and the costs of corresponding equipment and work stages used.

Motor-generators of hundreds of megawatts are existing commercial technology that, with minor modifications, can be adapted to a PTES plant. The plant's control system would in principle be a combination of gas turbine power plant and pumped storage systems, supplemented by predictive pressure ratio control and possible active rotor tip gap control.

If the electricity storage system presented here proves to be technically feasible, and its initial price estimate is even approximately correct, its global impact would be revolutionary in the energy sector. Solar cells and wind power already produce electricity that is at least several cents/kWh cheaper than electricity production using fossil fuels. If the almost free electricity produced during their production peaks can be stored for a long time with a margin of about 2–4 cents, then electricity production based on fossil energy will become unprofitable almost everywhere. In addition, cheap electricity all year round would accelerate the replacement of gas and oil heating with heat pumps. Together, these would make the global goal of carbon neutrality in 2050 entirely possible. At a global level, economic considerations and political realities have determined the use of fossil fuels and the continuous growth of their carbon emissions in electricity production. The only guaranteed way to abandon the use of fossil fuels on a rapid schedule is to make their use economically unprofitable.

Checklist:

https://en.wikipedia.org/wiki/Three-dimensional_losses_and_correlation_in_turbomachinery

https://www.jafmonline.net/article_1785_552db38eff898db561ebfc12e98241b0.pdf

// Modified surge margin calculation:

https://iris.polito.it/retrieve/580ec40f-1a42-42d8-8f74-841adc5600cd/postprint.pdf

Blockage

Blade Row and Blockage Modelling in an Axial Compressor Throughflow Code:

https://core.ac.uk/download/pdf/37320547.pdf

Turbin basics:

https://www.lth.se/fileadmin/tpe/Kurser/Chapter_4.pdf

Denton:

https://www.unife.it/ing/lm.meccanica/insegnamenti/fluidodinamica-delle-macchine/materiale-didattico/JT_V115_621-656.pdf

Kracker & Okapuu model implementation:

Preliminary Design and Optimization of Axial Turbines Accounting for Diffuser Performance

Roberto Agromayor * and Lars O. Nord

https://www.made-in-china.com/products-search/hot-china-products/Compressor_Blade.html

Compressor disc for Boeing 737-300 – 737-500

https://www.ebay.com/itm/266267945316

https://en.wikipedia.org/wiki/CFM_International_CFM56

Fan diameter ~1.5

Turha juttu: file:///C:/Users/asaarenheimo/Downloads/4207__1662749128.pdf

About endwall blockage:

https://scispace.com/pdf/endwall-blockage-in-axial-compressors-3lkb10wk3t.pdf

Reynolds correction of profile and endwall losses

file:///C:/Users/asaarenheimo/Downloads/1-s2.0-S1000936125003413-main.pdf

Hyvä ja monipuolinen:

DESKTOP COMPUTER PROGRAMS FOR PRELIMINARY DESIGN OF TRANSONIC COMPRESSOR ROTORS:

https://apps.dtic.mil/sti/pdfs/ADA390533.pdf

file:///C:/Users/asaarenheimo/Downloads/8_476.pdf => solidity lisätty, tsekkaa vielä Niclaksen koodi